Supplementary Information for:

Airborne microplastics: An unexpected source of atmospheric brown carbon

Yangyang Liu[1,2], Weinan Leng[3], Qiuyue Ge[4], Sonali Srivastava[1], Delicia Gonsalves[1], Hosein Foroutan[1], Liwu Zhang[4], Chak K. Chan[5], Gabriel Isaacman-VanWertz[1], Peter J. Vikesland[1,2,]*

[1]*Department of Civil and Environmental Engineering, Virginia Tech, Blacksburg, Virginia 24061, United States;*
[2]*Virginia Tech Institute of Critical Technology and Applied Science (ICTAS), Sustainable Nanotechnology Center (VTSuN), Blacksburg, Virginia 24061, United States.*
[3]*Virginia Tech Institute for Critical Technology and Applied Science, Nanoscale Characterization and Fabrication Laboratory, Blacksburg, Virginia 24061, United States.*
[4]*Shanghai Key Laboratory of Atmospheric Particle Pollution and Prevention, National Observations and Research Station for Wetland Ecosystems of the Yangtze Estuary, IRDR international Center of Excellence on Risk Interconnectivity and Governance on Weather, Department of Environmental Science & Engineering, Fudan University, Shanghai, 200433, Peoples' Republic of China*
[5]*Division of Physical Science and Engineering, King Abdullah University of Science and Technology (KAUST), Thuwal, Jeddah 23955-6900, Kingdom of Saudi Arabia*
*To whom correspondence should be addressed**: vikesland@vt.edu (Peter J. Vikesland)

This file contains:

Supplementary Notes 1-3

Supplementary Discussions 1-5

Supplementary Tables 1-5

Supplementary Figures 1-28

Supplementary Reference 1-120

Table of Contents

Supplementary Notes:

Supplementary Note 1: Contact Angle Sample Preparation and Measurement

Polyethylene (PE) particles were exposed to simulated solar irradiation for either 0 (fresh PE) or 180 min (aged PE) in both aerosolized and bulk nitrate samples. After exposure, the suspensions were filtered using a cup-type vacuum filtration funnel to collect the particles onto a 0.45 μm PTFE membrane filter. The resulting samples were washed thoroughly with deionized water to remove residual salts and then dried. Water contact angles were measured by placing a 2 μL water droplet onto the surface of dried PE particles immobilized onto a glass substrate using double-sided adhesive tape. The layered structure from top to bottom consists of: (1) the test PE layer; (2) supporting adhesive tape; and (3) rigid glass slide. This configuration ensured a flat, uniform surface for reliable contact angle measurements (see Supplementary Fig. 6).

Supplementary Note 2: Dynamic light scattering measurement

Dynamic light scattering (DLS) measurements were performed using a Zetasizer Nano ZS (Malvern Panalytical) equipped with a 633 nm laser to determine the hydrodynamic particle size distribution of aged PE. The instrument was operated at 25 °C and each sample was equilibrated for 30 seconds prior to measurement. Dual-angle detection mode was employed thus enabling simultaneous acquisition of forward (13°) and backscatter (173°) signals to improve accuracy across a broad size range. Both the detector position and the laser attenuator were automatically optimized by the instrument software to ensure optimal count rates. The refractive index of the PE particles was set to 1.552, while the dispersant—aqueous 1 M $NaNO_3$—was defined with viscosity of 0.8937 mPa·s and a refractive index of 1.336. The intensity-weighted size distributions were analyzed using the instrument's general-purpose algorithm.

Supplementary Note 3: ATR-FTIR measurement

Attenuated total reflectance Fourier-transform infrared (ATR-FTIR) spectroscopy was performed using a Bruker Invenio X spectrometer equipped with a diamond crystal ATR accessory (A225/Q Platinum ATR, Diamond #CD000002) to analyze photoaged PE particles. All measurements were conducted under ambient temperature. Spectral resolution was set to 4 cm^{-1} with 12 scans for both sample and background spectra. Data were collected in absorbance mode over the range of 4000 to 400 cm^{-1}. The interferogram size was set to 16k points with a scanner velocity of 10 kHz. The RT-DLaTGS detector was used, and acquisition was carried out in double-sided, forward-backward mode.

Supplementary Discussion:

Supplementary Discussion 1: Synchronous and asynchronous Attenuated Total Reflectance Fourier-Transform Infrared (ATR) spectra analyses of products in the bulk and aerosol systems.

By combining synchronous and asynchronous ATR analyses, we can deduce the temporal evolution of functional groups and their inter-relationships. In 2D correlation theory, a synchronous cross-peak indicates that two vibrations change intensity in unison (either both increasing or both decreasing), whereas asynchronous cross-peaks appear only if there is a phase delay between their changes[1]. Analysis of PE particles after photo treatment shows the correlated formation of oxygenated fragments, with detailed 2D correlation spectroscopy (2DCOS) providing insight into the dynamic changes resulting from the different aging environments[2].

In the synchronous 2D map collected following bulk aging (Supplementary Figure 13A), positive auto-peaks are prominent at ~1400–1300 cm^{-1} (I: C-O stretch and symmetric NO$_2$), ~1710 cm^{-1} (II: C=O stretch, ketones/acids),   and ~3300–2400 cm^{-1} (III: broad O-H, C-H, N-H regions), indicating these bands vary significantly with time[3-5]. Positive cross-peaks between ~1710 cm^{-1} and ~1400–1300 cm^{-1} suggest coordinated formation of carbonyl and ether/alcohol groups, consistent with oxidative chain scission releasing polar fragments[6,7]. The structured pattern in the dashed boxes (e.g., 3200–2400 cm^{-1} vs. 1800–800 cm^{-1}) implies a unified oxidation pathway, where O-H broadening correlates with the emergence of C=O, reflecting hydrogen bonding in carboxylic acids[8].

The synchronous 2D map collected following aerosol aging (Supplementary Figure 13B) displays more intricate patterns, including strong positive auto-peaks at ~1710 cm^{-1}, ~1550 cm^{-1}, and ~1300 cm^{-1}, but negative cross-peaks (e.g., ~1700 cm^{-1} vs. ~1400 cm^{-1}), indicating opposing changes where carbonyl growth accompanies the loss or shift in certain C-O/NO$_2$ bands, possibly due to competitive nitration vs. oxidation[9]. The dashed boxes highlight clustered negative regions (e.g., 2400–1600 cm^{-1} vs. 1200–800 cm^{-1}), suggesting anti-correlated evolution of O-H/C-H with fingerprint modes (i.e., characteristic IR absorption bands in the 1800–800 cm^{-1} region that are unique to specific molecular structures), indicative of dehydration or elimination and the formation of C=C bonds following oxidation[10]. This complexity may reflect interfacial confinement, where radical recombination competes with propagation[11].

The asynchronous map collected following bulk aging (Supplementary Figure 13C) reveals sequential details via Noda's rules: for cross-peak $\Phi(v_1, v_2)$, where v_1 and v_2 are the wavenumbers (in cm^{-1}) of the two vibrational bands being compared, and Φ is the asynchronous intensity (the pitchfork 'Φ' notation is standard in 2DCOS to denote the

asynchronous correlation function between the two bands). If $\Phi > 0$ and synchronous $\Psi(v1, v2) > 0$, v_1 changes before v_2[12]. Here, positive Φ at ~1710 cm^{-1} (v_1) vs. ~1160 cm^{-1} (v_2) indicates carbonyl formation precedes development of the signal for the C-O stretch, aligning with initial ketone production from peroxy disproportionation, followed by alcohol/ether from hydroperoxide decomposition[13,14]. Negative Φ in the ~1550 cm^{-1} (NO_2) vs. the ~1710 cm^{-1} region suggests delayed nitration, occurring after oxidation creates reactive sites (e.g., alkyl radicals)[15,16]. The anti-correlated patterns in the lower wavenumber regions (~900–800 cm^{-1}, possibly C-H out-of-plane bends) suggest that minor structural rearrangements lag behind functional group changes[17]. Overall, this points to a linear, •OH-driven mechanism with minimal branching, where primary oxidation products dissolve first, followed by more functionalized fragments.

In the asynchronous map collected following aerosol aging (Supplementary Figure 13D), diverse patterns suggest the following sequences: positive Φ at ~1710 cm^{-1} (v_1) vs. ~1550 cm^{-1} (v_2) implies carbonyls form before nitro groups, but negative Φ at ~1640 cm^{-1} (C=C) vs. ~1710 cm^{-1} suggests unsaturation lags the carbonyls, consistent with elimination from β-hydroxy carbonyls post-oxidation[18,19]. Strong negative Φ in ~890 cm^{-1} (vinylidene wag) vs. ~1350 cm^{-1} (NO_2) indicates nitro addition precedes terminal alkene formation, pointing to •NO_2 attacking radicals early, followed by chain scission/dehydration[20,21]. The broader, more fragmented patterns compared to bulk (e.g., multiple hotspots in 4000–2400 cm^{-1}) reflect branched pathways: simultaneous •OH oxidation and •NO_2 nitration, with interfacial acidity enhancing hydrolysis/nitrite formation[22,23]. This leads to dynamic shifts, where some bands (e.g., peroxynitrate intermediates ~1380 cm^{-1}) transiently appear and decay[24].

In summary, the ATR results suggest that aging in the bulk phase is •OH-driven and linear, with 2DCOS showing coordinated, sequential changes. In contrast, aerosol aging is multifaceted and accelerated since 2DCOS reveals competitive, branched dynamics (Extended Data Fig. 4; Supplementary Figure 13). These findings underscore the distinct role of the aerosol phase in PE aging.

Supplementary Discussion 2: Calculation of equivalent exposure times— converting lab-based aging times into atmospheric-relevant ones.

Absorption from microplastic-derived organic carbon is calculated as:

$$\text{Abs}_{\text{MPS, City}_i} = \text{OC}_{\text{MPS, City}_i} \times \text{MAC}_{\text{MPS, City}_i} \qquad (S1)$$

where $\text{OC}_{\text{MPS, City}_i}$ is the organic carbon formed in city, i, from the oxidation of

microplastics in that city and $\text{MAC}_{\text{MPS, City}_i}$ the average MAC of MP-derived organics in

city *i*. The total amount of microplastic-derived organic carbon is the sum of organic carbon, $OC_{j, City_i}$, from each type of microplastic, *j*, which is calculated from laboratory-determined and modeled oxidation kinetics:

$$OC_{MPS, City_i} = \sum_{j=1}^{n} OC_{j, City_i} = \sum_{j=1}^{n} MPS_i \times P \times \omega_{i,j} \times CC_j \times f(t_{lab,i}) \tag{S2}$$

where MPS_i is the total mass concentration of microplastics in city *i* (Supplementary Discussion 4), P is the probability that a microplastic combines with nitrate to enable this chemistry, $\omega_{i,j}$ the mass fraction of microplastic type *j* in city *i*, CC_j is the conversion efficiency (%) of specific microplastic type *j* to organic carbon under standardized empirical laboratory conditions, and $f(t_{lab,i})$ adjusts conversion efficiency to real-world conditions in city *i* such that the combined term $CC_j \times f(t_{lab,i})$ captures the real-world fraction of a microplastic converted to OC under local conditions in the city. Different microplastics have different CC_j values, which were determined experimentally under laboratory aging conditions. Conversion efficiencies are calculated for a standard laboratory exposure at a given light intensity and nitrate concentration and are provided for each type of microplastic in Supplementary Table 3. Conversion efficiency is corrected for the amount of light and nitrate exposure in the real world compared to the standard laboratory exposure using an effective conversion fraction $f(t_{lab,i})$ that adjusts a real-world exposure time (3, 5, and 7 days studied in this work) to an equivalent time of laboratory oxidation based on ratios of nitrate concentration and photolysis rates as described in Supplementary Discussion 3.

The effective conversion fraction as a function of time is empirical (Supplementary Equation S3, Supplementary Figure 26A), determined from observed laboratory oxidation kinetics of polyethylene microplastic, and is equal to 1.0 at standard laboratory exposure, increasing to an asymptote at longer reaction times representing complete conversion of MPs to organic carbon, as:

$$f(t) = -3.654 \times (e^{-t/1.872}) + 1.723 \tag{S3}$$

MAC is observed emperically to increase with exposure time (Supplementary Fig. 26B), so the average MAC in a city, *i,* is calculated as the standardized laboratory MAC of each plastic, *j*, weighted by its relative contribution to microplastic-derived OC (i.e., its mass fraction, $\frac{OC_{j, City_i}}{OC_{MPS, City_i}}$), and adjusted by a exposure-dependent MAC enhancement, γ, that is 1.0 at standardized laboratory exposure and increases sigmoidally at longer exposure times (Supplementary Figure 26B, Equation S4).

$$MAC_{MPS, City_i} = \sum_{j=1}^{n} MAC_j \times \frac{OC_{j, City_i}}{OC_{MPS, City_i}} \times \gamma(t_{lab,i}) \qquad \text{(S4)}$$

This average MAC describes the OC-mass-weighted average of MAC values for each microplastic present and is multiplied by the total microplastic-derived OC to yield microplastic-derived absorption as in Equations 4 and 5. The enhancement value, γ, is empirically fit to laboratory observations for the MAC of microplastic-derived organics increasing approximately sigmoidally with exposure time (Supplementary Fig. 26):

$$\gamma(t) = 0.989 + 1.79*(1-e^{-\left(\frac{t}{7.2}\right)^{6.93}}) + 9.873*(1-e^{-\left(\frac{t}{221.3}\right)^{1.19}}) \qquad \text{(S5)}$$

Real-world exposure times of 3, 5, and 7 days were used to calculate absorption from microplastic-derived organics in each city of interest, as in Equation 6 and Supplementary Equation S1. The probability factor P is estimated using a theoretical model that considers the forces of Brownian diffusion, gravitational settling, and turbulent shear (Supplementary Discussion 5 and Supplementary Fig. 27). A constant value of P = 10% is used in this work, which is an approximate central tendency for this value for microplastics a few tens of diameters in radius at aerosol loadings of a few micrograms per cubic meter, which are the general conditions of cities studied here.

Taken above, supplementary Equation S1 is mathematically equivalent to:

$$Abs_{MPS, City_i} = \sum_{j=1}^{n} Abs_{j, City_i} = \sum_{j=1}^{n} MAC_j \times \gamma(t_{lab,i}) \times MPS_i \times P \times \omega_{i,j} \times CC_j \times f(t_{lab,i}) \qquad \text{(S6)}$$

In this formulation, total absorption is equal to the sum of absorption from each microplastic type, *j*. The first two terms describe the MAC of a given microplastic type at a given exposure time, and the last five terms describe the conversion of microplastics into aerosol organic carbon in a given city.

Supplementary Discussion 3: Determination of the effective laboratory oxidation time

Laboratory photochemical aging was conducted using a xenon-arc solar simulator (Model 11002 SunLite™, Abet Technologies) equipped with an AM 1.5G filter. This lamp provides an average output equivalent to ~0.61 sun (611 W m^{-2}), with a Class A spectral match to the standard solar reference spectrum—ASTM G-173 global solar spectrum (AM 1.5G). All spectral data were converted to photon flux (photons cm^{-2} s^{-1} nm^{-1}) across the UV range of interest. Using nitrate actinometry, we quantified the effective UV dose for both the lab and for the authentic sun conditions. A series of nitrate solutions with varying concentrations (0.02–6 M NaNO₃) was used to account for inner-filter effects on photolysis. The wavelength range 300–350 nm was chosen for integration since nitrate absorbs and photolyzes predominantly in this region. The wavelength-dependent molar absorptivity ($\varepsilon(\lambda)$) of nitrate at each concentration was taken from our measured spectra, and a quantum yield $\varphi = 0.01$ was assumed for nitrate photolysis over 290 nm[25,26]. For

each nitrate concentration c, the photolysis rate J (s^{-1}) was calculated under both spectra by integrating the wavelength-dependent profiles of the spectral photon flux $I(\lambda)$ and the nitrate absorption coefficient (derived from $\varepsilon(\lambda)$) over 300–350 nm:

$$J = 0.1 * \int_{300}^{350} \phi \varepsilon_c(\lambda) I(\lambda) d\lambda \qquad (S7)$$

with appropriate constants for unit conversion (Avogadro's number and factor log(10) to convert ε (M^{-1} cm^{-1}) to absorption cross-section). This integration was performed for (i) the authentic solar spectrum (yielding J_{real}) and (ii) the solar simulator spectrum (yielding J_{lab}), with their ratio written as:

$$\frac{J_{NO_3^- real(C)}}{J_{NO_3^- lab(C_{lab})}} = \frac{\int_{300}^{350} \phi \varepsilon_{real(C)}(\lambda) I_{real}(\lambda) d\lambda}{\int_{300}^{350} \phi \varepsilon_{lab(C_{lab})}(\lambda) I_{lab}(\lambda) d\lambda} = \int_{300}^{350} \frac{\varepsilon(C_{real})(\lambda)}{\varepsilon(C_{lab})(\lambda)} \frac{I_{real}(\lambda)}{I_{lab}(\lambda)} d\lambda = \int_{300}^{350} R(C_{real}) \, F d\lambda \quad (S8)$$

In the laboratory case, we used the absorptivity for 1 M nitrate to represent the conditions of our experiments (since 1 M NO_3^- was present during lab irradiation), and the factors $R(C_{real})$ and F account for differences between laboratory and real-world conditions in concentration-dependent molar absorptivity and total light intensity, respectively. Because the light spectrum is the same between the laboratory and sun, these terms are wavelength independent, and the integral can be treated as a constant for a given concentration.

In this case, $R(C_{real})$ expresses how the concentration-dependent absorption cross-section (300–350 nm) in the real sunlight at a real-world concentration, C_{real}, compares to that in the lab simulator at 1M. We found that $\int_{300}^{350} \varepsilon_{(C)} d\lambda$ is highly concentration-dependent due to increased light attenuation at higher nitrate levels. Across the range 0.02–6 M, $\varepsilon_{(C)}$ decreased as a function of concentration (C) and could be empirically fit to a DoseResp regression ($y = A+B/(1+10^{(C-x)D})$) on a plot (yielding A = 14.77, B = 51.23, C = 2.17, D = -0.27, R^2 = 0.99, Supplementary Figure 25A). This relationship allowed us to interpolate or extrapolate R(C) for any possible intermediate concentration-dependent absorption cross-section in the real world (Supplementary Figure 25B). Nitrate aerosol concentrations for typical regions were derived using the therodynamic ISORROPIA (II) model[27] (https://www.epfl.ch/labs/lapi/models-and-software/isorropia/). This was done by inputting the water-soluble ion concentration and meteorological factors of specific cities, collected from the literature (Supplementary Tables 4,5).

The intensity correction factor F is defined to account for the overall difference in average light intensity between the simulator (SunLite™ 11002) and real sunlight (Supplementary Fig. 25B). We assumed that the relevant wavelength-dependent spectral profiles are comparable in the 300–350 nm range (the dominant nitrate absorption band). The

intensity of the SunLite™ lamp in this range was measured as 611 W m^{-2} (averaged measurement results), corresponding to a flux of 5.17×10^{18} photons cm^{-1} h^{-1}, while the daily average solar intensity is 215 W m^{-2}, corresponding to a flux of 1.81×10^{18} photons cm^{-1} h^{-1}, (ASTM G173, see Supplementary Fig. 25). Therefore, the intensity correction factor is simply:

$$F = \frac{I_{real}}{I_{lab}} = \frac{1.81 \times 10^{18} \text{ photons cm}^{-1} \text{ day}^{-1}}{5.17 \times 10^{18} \text{ photons cm}^{-1} \text{ day}^{-1}} \approx 1/2.85 \qquad (S9)$$

The ratio R(c) together with F convert exposure durations between laboratory and ambient conditions at a given city, *i*. A laboratory experiment lasting t_{lab} hours corresponds to a real sunlight exposure, t_{real} as:

$$t_{real,i} = \frac{1}{R(C_{real,i}) \cdot F} \cdot \frac{[NO_3]_{lab}}{[NO_3]_{real,i}} t_{lab,i} \qquad (S10)$$

Supplementary Discussion 4: Estimation and description of airborne microplastic concentrations (µg/m^3) in different regions.

South Korea:
We utilized data indicating a particle number concentration ranging from 0.51 to 9.88 particles/m^3, with an average of ~2.2 ± 1.3 particles/m^3 [28]. The microplastic composition was predominantly fibers (90%, 100–1000 µm), followed by fragments (8%, 10–1000 µm) and films (2%, 50–1000 µm)[28]. Converting particle number to mass concentration (µg/m^3) required assumptions about shape, size, and density due to the absence of direct mass data. Fibers were modeled as cylindrical with a median length of 550 µm and a diameter of 20 µm, fragments as spherical with a median diameter of 505 µm, and films as thin sheets with median dimensions of 525 µm × 525 µm × 20 µm. A uniform density of 1 g/cm^3, typical of common plastics like polyethylene and polypropylene, was applied[29]. Volume calculations yielded approximately 172,788 µm^3 for fibers, 67,433,333 µm^3 for fragments, and 5,512,500 µm^3 for films, translating to individual masses of 0.17 µg, 0.067 µg, and 0.0055 µg, respectively. Multiplying these by their respective average particle concentrations (2.01, 0.18, and 0.045 particles/m^3) resulted in mass contributions of 0.35 µg/m^3 from fibers, 1.2×10^{-2} µg/m^3 from fragments, and 2.5×10^{-4} µg/m^3 from films, summing to an estimated total mass concentration of approximately 0.37 µg/m^3.

Pakistan:
Fibers were modeled as cylindrical with a fixed diameter of 20 µm[30] and lengths based on the mean of each size category (e.g., 25 µm for <50 µm, 75 µm for 50–100 µm, etc.), fragments as spherical with diameters equal to the category mean (e.g., 25 µm, 75 µm, etc.), and sheets as thin films with square dimensions. A uniform density of 1 g/cm^3, representative of common plastics such as polyethylene and polypropylene, was applied[29]. Particle concentrations were apportioned by type and size (e.g., fibers in <50

μm: 0.194 items/m^3, fragments in 250–500 μm: 0.080 items/m^3), yielding volumes such as 7,854 μm^3 for fibers (<50 μm), 27,754,646 μm^3 for fragments (250–500 μm), and 1,406,250 μm^3 for sheets (250–500 μm)[31]. These translated to masses per particle (e.g., 7.9 × 10^{-3} μg for fibers <50 μm, 27.8 μg for fragments 250–500 μm), resulting in total contributions of approximately 3.76 × 10^{-2} μg/m^3 from fibers, 5.5 μg/m^3 from fragments, and 1.8 × 10^{-2} μg/m^3 from sheets, summing to an estimated mass concentration of ~5.6 μg/m^3.

Brazil:
Given the deposition flux, conversion to airborne particle concentration (C) required an assumed deposition velocity (V_d), set at 0.001 m/s (1 mm/s) to reflect turbulent atmospheric conditions for 100–200 μm particles[32], yielding F = 123.20 / 86400 ≈ 1.4 × 10^{-3} particles/m^2/s and C = F / V_d ≈ 1.43 particles/m^3. Mass per particle was calculated by assigning shapes and a uniform density of 1 g/cm^3 (typical for plastics such as polyethylene): fragments as spheres with a median diameter of 150 μm (volume ≈ 1.77 × 10^6 μm^3, mass ≈ 1.77 μg), films as 1 μm thick square sheets with 150 μm sides (volume ≈ 22,500 μm^3, mass ≈ 2.25 × 10^{-2} μg), granules as identical to fragments (1.77 μg), and foams as fragments with half density (~0.88 μg)[29]. Weighting by prevalence, the average mass was 1.50 μg/particle, resulting in a mass concentration of 1.43 × 1.50 ≈ 2.13 μg/m^3, reported as 1 μg/m^3 for simplicity. However, uncertainty in V_d (0.001–0.1 m/s) significantly impacts this estimate, yielding a C range of 0.014–1.43 particles/m^3 and a mass concentration of 0.021–2.13 μg/m^3, while shape assumptions (e.g., thicker 10 μm films increasing mass to 0.23 μg) and density variations (e.g., 0.5–1.4 g/cm^3) could further adjust the result.

California, United States:
We utilized corrected Nile red-stained microscopy data indicating a mean concentration of 0.6 ± 0.6 fibers/m^3 and 5.6 ± 3.2 fragments/m^3, with fibers exhibiting a mean length of 616 μm (range 25–2061 μm, SD 536 μm) and fragments a mean maximum width of 104 μm (range 51–408 μm, SD 64 μm), excluding particles smaller than 20 μm[33]. Conversion to mass concentration involved assuming cylindrical shapes for fibers (diameter 20 μm, length 616 μm) and spherical shapes for fragments (diameter 104 μm), with a uniform density of 1 g/cm^3, typical of common plastics like polyethylene and polypropylene, though a range of 0.9–1.1 g/cm^3 was considered[29]. Volume calculations yielded 193,514 μm^3 for fibers (mass ≈ 0.19 μg, contribution ≈ 0.12 μg/m^3) and 588,787 μm^3 for fragments (mass ≈ 0.58 μg, contribution ≈ 3.3 μg/m^3), summing to an estimated total mass concentration of approximately 3.4 μg/m^3. This estimate is sensitive to shape assumptions: modeling fragments as flat disks (104 μm diameter, 10 μm thick) reduces their contribution to ≈0.48 μg/m^3 (total ≈0.59 μg/m^3), while a cubic shape increases it to ≈6.30 μg/m^3 (total ≈6.42 μg/m^3); a smaller fiber diameter (10 μm) lowers their contribution to ≈0.029 μg/m^3 (total ≈3.332 μg/m^3). Density variations (0.9–1.1 g/cm^3) adjust the range

to 3.07–3.75 µg/m³, and concentration uncertainties (±0.12 µg/m³ for fibers, ±1.88 µg/m³ for fragments) suggest a total range of 1.5–5.3 µg/m³.

Australia:
We utilized data indicating a mean particle concentration of 0.17 ± 0.06 particles/m³, predominantly fibers, with size distribution derived from a cumulative distribution plot showing approximately 80% of fibers less than 500 µm in length, a median length estimated at 312.5 µm, and a significant fraction (20–30%) below 50 µm, though an average length of 750 µm was adopted to account for the skewed distribution toward larger sizes[34]. Assuming a cylindrical shape with a diameter of 20 µm, typical for microplastic fibers as noted in Microplastic Fibers San Francisco Estuary Institute, and a density of 1 g/cm³ (ranging 0.9–1.1 g/cm³, ref.[29]), the volume was calculated as $\pi*(10)^2*750 \approx 235{,}620$ µm³, yielding a mass of approximately 0.24 µg per particle and a total mass concentration of 0.17 * 0.2356 ≈ 0.04 µg/m³.

Taiwan, China:
We analyzed data reporting a mean concentration of 28 ± 24 MPs/m³, with fragments dominating (99%) over fibers (1%), and a size distribution of 79% <50 µm and 21% 50–100 µm, alongside material compositions of acrylic (40%) and rubber (13%)[35]. Fragments were modeled as spherical with a density of 1.1 g/cm³ (averaging acrylic at 1.18 g/cm³ and rubber at 1.0 g/cm³), yielding masses of 9×10^{-3} µg for <50 µm (diameter 25 µm, volume ≈ 8,181 µm³, contribution ≈ 0.20 µg/m³ from 21.90 MPs/m³) and 0.24 µg for 50–100 µm (diameter 75 µm, volume ≈ 221,302 µm³, contribution ≈ 1.41 µg/m³ from 5.82 MPs/m³), totaling 1.611 µg/m³; fibers, assumed cylindrical with a 20 µm diameter, had lengths of 25 µm and 75 µm for the respective size bins, resulting in masses of 0.0864 µg and 0.26 µg (contributions ≈ 0.02 µg/m³ and 0.016 µg/m³ from 0.22 and 0.06 MPs/m³), summing to 0.035 µg/m³ [29]. The total estimated mass concentration is approximately 1.7 µg/m³, rounded to 2 µg/m³, with fragments contributing the majority due to their high abundance (27.7 MPs/m³). However, this estimate is sensitive to shape assumptions—if fragments are cubic, the mass concentration increases to ~2.0 µg/m³, or if thin sheets (1 µm thick), it drops to ~0.6 µg/m³—and density variations (0.9–1.1 g/cm³) adjust the range to 1.35–1.7 µg/m³, while the concentration uncertainty (4–52 MPs/m³) suggests a broader range of 0.25–3.25 µg/m³, refined to 1–3 µg/m³ considering realistic constraints.

Wenzhou, China:
We analyzed data reporting a mean concentration of 189 ± 85 MPs/m³, with fragments dominating (94.2%) over fibers (5.8%), and a size distribution of 65.1% at 5–30 µm, 29.4% at 30–100 µm, and 5.5% >100 µm, where fibers were prevalent in the >100 µm range (74.3–100% of that fraction)[36]. Fragments were modeled as spherical with a density of 1 g/cm³ (range 0.9–1.1 g/cm³), yielding masses of 2.8×10^{-3} µg for 5–30 µm (diameter 17.5 µm, contribution ≈ 0.33 µg/m³ from 116 MPs/m³), 0.144 µg for 30–100 µm (diameter 65

µm, contribution ≈ 7.534 µg/m^3 from 52.4 MPs/m^3), and 1.77 µg for >100 µm (diameter 150 µm, contribution ≈ 7.07 µg/m^3 from 4 MPs/m^3), totaling ~14.9 µg/m^3; fibers, assumed cylindrical with a 20 µm diameter, had masses of 5.5 × 10^{-3} µg, 0.02 µg, and 0.47 µg for the respective size bins (average length 1500 µm for >100 µm), contributing ≈ 0.0385, 0.065, and 2.83 µg/m^3, summing to ~2.93 µg/m^3. The total estimated mass concentration is approximately 15.9 µg/m^3, rounded to 15 µg/m^3, with fragments contributing the majority due to their high abundance (178 MPs/m^3). Notably, larger fibers (>100 µm), despite their low abundance (6 MPs/m^3), contribute significantly (≈2.8 µg/m^3, ~60% of fiber mass) due to their higher mass. However, this estimate is sensitive to shape assumptions—if fragments are modeled as thin sheets (1 µm thick), the total drops to 6.4 µg/m^3, while cubic shapes increase it to 16.4 µg/m^3—and density variations adjust the range to 14.3–17.5 µg/m^3, with concentration uncertainty (104–274 MPs/m^3) suggesting a broader range of 8.0–23.5 µg/m^3.

Sri Lanka:
We analyzed data reporting a mean concentration of 0.12 MPs/m^3 (range 0.01–0.23 MPs/m^3), with fibers dominating (98%) over fragments (2%), the latter observed only in the high-density industrial zone (IZ1)[37]. Fibers ranged from 67 to 4919 µm (mean 768.63 ± 25.42 µm, median 551 µm), predominantly in the 100–300 µm and 300–500 µm size classes, while fragments were primarily 500–700 µm[37]. Fibers, modeled as cylindrical with a 20 µm diameter, 551 µm length, and density of 1 g/cm^3 (range 0.9–1.1 g/cm^3), had a mass of ~0.17 µg (volume ≈ 173,415 µm^3), contributing ≈ 0.020 µg/m^3 from 0.1176 MPs/m^3; fragments, assumed spherical with a 600 µm diameter, had a mass of 113.1 µg (volume ≈ 113,097,336 µm^3), contributing ~0.27 µg/m^3 from 2.4 × 10^{-3} MPs/m^3. The total mass concentration is estimated at 0.3 µg/m^3, with fragments contributing disproportionately (~0.27 µg/m^3) due to their larger size despite low abundance. Sensitivity analysis reveals significant uncertainty: if fragments are modeled as thin sheets (1 µm thick), their contribution drops to 0.001 µg/m^3, reducing the total to 0.021 µg/m^3; if cubic, their contribution rises to 0.518 µg/m^3, increasing the total to 0.539 µg/m^3. Density variations adjust the range to 0.26–0.32 µg/m^3, and concentration variability (0.01–0.23 MPs/m^3) suggests a broader range of 0.02–0.56 µg/m^3. Compared to urban settings like Paris (0.9 MPs/m^3) or Shanghai (0.93 MPs/m^3), this estimate is lower, likely due to Sri Lanka's lower population density (355 inhabitants/km^2), reduced industrialization, and sampling during the post-COVID-19 lockdown period, which may have diluted MP levels, highlighting the influence of regional and temporal factors on MP concentrations.

Xiamen, China:
In Xiamen, China, the atmospheric MP mass concentration in outdoor air samples was estimated using a mean numerical concentration of 0.011 ± 0.012 MPs/m^3 (range 0–0.062 MPs/m^3), with fibers dominating at approximately 84% (94.9% at DTA, 73.5% at URFA)

and non-fiber MPs (fragments, granules, films, microbeads) comprising 16%, as identified across 69 and 54 valid data points from two districts[38]. The size distribution indicated over 50% of MPs were <1.0 mm, categorized into six classes (<0.1 mm, 0.1–0.3 mm, 0.3–0.5 mm, 0.5–1.0 mm, 1.0–2.5 mm, 2.5–5.0 mm), with an assumed average size of 0.8 mm (800 μm) based on the prevalence of 0.1–0.3 mm and 0.5–1.0 mm ranges. Fibers, modeled as cylindrical with a 20 μm diameter, 800 μm length, and density of 1 g/cm^3 (range 0.9–1.3 g/cm^3)[29], had a mass of 0.251 μg (volume ≈ 251,328 μm^3), contributing ≈ 0.0023 μg/m^3 from 0.0092 MPs/m^3; non-fiber MPs, assumed spherical with an 800 μm diameter, had a mass of 268.5 μg (volume ≈ 268,499,200 μm^3), contributing ≈ 0.47 μg/m^3 from 0.0018 MPs/m^3, yielding a total mass concentration of 0.47 μg/m^3. However, if non-fiber MPs were thin sheets (10 μm thick), their mass dropped to 5.03 μg, reducing their contribution to 8.7 × 10^{-3} μg/m^3 and the total to 0.011 μg/m^3. Drawing from a comparable study in Sri Lanka (0.12 MPs/m^3, 0.3 μg/m^3, implying 2.5 μg/particle), the mass concentration in Xiamen was estimated at 0.028 μg/m^3 (0.011 × 2.5), with a range of 0.003–0.47 μg/m^3 considering concentration variability and shape assumptions. Sensitivity analysis highlighted significant uncertainty: if non-fiber MPs were cubic (800 μm edge), their mass increased to 512 μg, raising the total to 2.9 μg/m^3; density variations (0.9–1.1 g/cm^3) adjusted the range to 0.42–0.51 μg/m^3 for the spherical assumption. Notably, despite their low abundance (16%), non-fiber MPs contributed disproportionately (~0.47 μg/m^3 vs. 2.3 × 10^{-3} μg/m^3 for fibers) when assumed spherical due to their larger volume.

Norway:
In Norway, the atmospheric MP mass concentration in outdoor air samples was estimated based on a deposition rate of 233 μg/m^2/day in Trondheim, derived from wet deposition data across multiple locations, with an average precipitation rate of 0.89 L/m^2/day (0.00089 m/day)[34,39]. Assuming a dominant composition of fibers (98%) and fragments (2%), consistent with similar studies, and drawing on size distributions from analogous research (e.g., Sri Lanka, where fibers averaged 551 μm in length and fragments 600 μm in diameter), the mass concentration was calculated using a wet deposition model[37]. Fibers, modeled as cylindrical with a 20 μm diameter, 551 μm length, and density of 1 g/cm^3 (range 0.9–1.1 g/cm^3), contributed approximately 0.020 μg/m^3 from a derived numerical concentration of 0.1176 MPs/m^3 (volume ≈ 173,415 μm^3, mass ≈ 0.17 μg/particle); fragments, assumed spherical with a 600 μm diameter, contributed ≈ 0.27 μg/m^3 from 2.4 × 10^{-3} MPs/m^3 (volume ≈ 113,097,336 μm^3, mass ≈ 113.1 μg/particle), yielding a total mass concentration of ~0.291 μg/m^3, rounded to 0.3 μg/m^3[29]. This estimate was corroborated by an alternative approach using a washout ratio of 10^6 and a precipitation rate of 0.00089 m/day, resulting in an air concentration of ~0.26 μg/m^3, or via dry deposition with a settling velocity of 0.01 m/s, yielding ≈ 0.27 μg/m^3, with a range of 0.03–0.3 μg/m^3 depending on velocity (0.01–0.1 m/s) and washout ratio (10^5–10^7) assumptions. Sensitivity analysis revealed significant uncertainty: if fragments were

modeled as cubic (600 μm edge), their mass increased to 216 μg, raising the total to ~0.54 μg/m^3, or as thin sheets (1 μm thick), reducing their contribution to 0.001 μg/m^3 and the total to 0.021 μg/m^3; density variations adjusted the range to 0.26–0.32 μg/m^3.

Four Provinces (Beijing, Shanghai, Hangzhou, Nanjing), China：

The original data provided number concentrations of 393 items/m^3 (Beijing), 267 items/m^3 (Shanghai), 246 items/m^3 (Hangzhou), and 177 items/m^3 (Nanjing), with a size distribution of 61.6% <30 μm, 33.1% 30–100 μm, 4.7% 100–300 μm, 0.5% 300–1000 μm, and 0.03% >1000 μm, and shape proportions of 88.2% fragments and 11.8% fibers[40]. The initial overestimation was attributed to a high-density assumption (1 g/cm^3) and potentially overestimated fiber dimensions. The revised approach adjusted the average MP density to 0.1 g/cm^3[29], reflecting the presence of lighter microplastics (e.g., expanded polystyrene with densities of 0.02–0.05 g/cm^3), and optimized fiber dimensions by assuming a fixed diameter of 10 μm rather than a length-dependent ratio, reducing their mass contribution. For Beijing, the total mass was calculated by first determining the mass of fragments (modeled as spheres) and fibers (modeled as cylinders) across size categories: fragments contributed ~69.2 μg/m^3 (e.g., 238 fragments <30 μm at 1.8×10^{-3} μg each yielded ~0.42 μg/m^3) and fibers 0.48 μg/m^3 (e.g., 14.8 fibers 100–300 μm at ~0.016 μg each yielded ~0.23 μg/m^3) under a 1 g/cm^3 density, totaling ~69.7 μg/m^3. Adjusting the density to 0.1 g/cm^3 reduced this to 6.97 μg/m^3, rounded to 7.0 μg/m^3. Using Beijing's concentration as a reference, the mass concentrations for the other cities were scaled proportionally based on their number concentrations: Shanghai (267/393 × 7.0 ≈ 4.7 μg/m^3), Hangzhou (246/393 × 7.0 ≈ 4.4 μg/m^3), and Nanjing (177/393 × 7.0 ≈ 3.1 μg/m^3).

France:
The estimation of MP mass concentration in outdoor air samples from Paris, France, provides critical supporting information for understanding atmospheric microplastic pollution in urban environments. Based on the provided data, the numerical concentration of microplastics in Paris outdoor air ranges from 0.3 to 1.5 MP/m^3, with a mean or median value of 0.9 MP/m^3, and particle sizes predominantly fall within 20–250 μm, though the broader size range spans 50 μm to 5 mm[41]. To estimate the mass concentration (μg/m^3), we assumed an average particle diameter of 100 μm, reflecting the geometric mean of the predominant size range (sqrt(20 × 250) ≈ 70.7 μm) and aligning with literature values such as 66.15 μm reported for indoor environments. Assuming a spherical particle shape and a conservative density of 900 kg/m^3 [29]—typical for common plastics like polyethylene—the volume of a 100 μm particle is approximately 5.24×10^{-13} m^3, yielding a mass of ~0.47 μg per particle. Multiplying this by the mean numerical concentration of 0.9 MP/m^3 results in an estimated mass concentration of 0.42 μg/m^3, with a potential range of 0.15 to 1.04 μg/m^3 when accounting for size variability (70.7–135 μm) and density uncertainties (900–1400 kg/m^3).

India:

The calculation began by converting the deposition rate to an air concentration, assuming a typical MP settling velocity of 0.001 m/s (equivalent to 86.4 m/day), a value consistent with literature on atmospheric MPs[29]. Dividing the deposition rate by this settling velocity yielded an air concentration of 1959.6 / 86.4 ≈ 22.68 MPs/m³ [41]. Next, the average mass per MP particle was calculated by considering the three dominant morphotypes—fibres (40.5%), films (26.5%), and fragments (33%)[42]—with their respective sizes and assumed densities. Fibres, with an average length of 1100 μm and an assumed diameter of 20 μm (density 1.2 g/cm³), had a volume of $\pi \times (10)^2 \times 1100 = 345{,}576$ μm³, resulting in a mass of $1.2 \times 3.46 \times 10^{-7} = {\sim}0.41$ μg. Films, with an average size of 206.5 μm and thickness of 5 μm, had a volume of $206.5 \times 206.5 \times 5 = 213{,}211.25$ μm³, yielding a mass of $1.2 \times 2.13 \times 10^{-7} = {\sim}0.26$ μg. Fragments, assumed spherical with a diameter of 98 μm, had a volume of $(4/3)\pi \times (49)^3 = 492{,}400$ μm³, resulting in a mass of $1.2 \times 4.9 \times 10^{-7} = 0.59$ μg. The weighted average mass per particle was then computed as $(0.41 \times 0.41) + (0.27 \times 0.26) + (0.33 \times 0.60) = 0.167 + 0.0678 + 0.195 = 0.43$ μg. Adjusting this mass to align with urban deposition, a slightly lower average mass of 0.4 μg was adopted, reflecting potentially smaller or less dense particles in urban settings. Multiplying the air concentration by this mass gave $22.68 \times 0.4 = 9.07$ μg/m³.

Supplementary Discussion 5: Estimation of collision probability between airborne microplastics and deliquescent nitrate aerosols.

To quantify the potential interaction frequency between airborne MPs and deliquescent nitrate aerosols under atmospheric conditions, we developed a mechanistic model that incorporates multiple collision pathways. This assessment is required to understand interfacial aging processes, heterogeneous reactivity, and pollutant encapsulation mechanisms in ambient aerosols.

Theoretical framework

The total collision kernel β_{total} [m³/s] between MPs and nitrate aerosols is defined as the sum of three contributions:

$$\beta_{total} = \beta_{Brownian} + \beta_{turbulence} + \beta_{gravity} \tag{S11}$$

The Brownian diffusion kernel can be written as follows:

$$\beta_{Brownian} = 4\pi(D_a + D_p)(r_a + r_p) \tag{S12}$$

where $D_i = \frac{k_B T}{6\pi\eta r_i}$ is the diffusion coefficient of particle i, with r_a denoting the radius of a deliquescent nitrate aerosol particle and r_p denoting the radius of the airborne microplastic particles. η is the dynamic viscosity of air, T = 298 K, and k_B is the Boltzmann constant. For Turbulent shear kernel (Saffman–Turner regime):

$$\beta_{turbulence} = C \cdot \varepsilon^{1/3} \cdot \left(r_a + r_p\right)^{7/3} \tag{S13}$$

where C ≈ 1.3 and $\varepsilon(m^2/s^3)$ is the turbulent dissipation rate (1.0) in the atmosphere. We considered gravitational settling kernel using the equation below:

$$\beta_{gravity} = \pi\left(r_a + r_p\right)^2 \cdot \left|v_a - v_p\right| \tag{S14}$$

where $v_i = \frac{2}{9}\frac{r_i^2 \rho_i g}{\eta}$ is the Stokes settling velocity, and p_i is the particle density.

Parameter space and concentration normalization

To convert aerosol and MP mass concentrations to number concentrations, we assumed spherical geometries and representative densities for each particle type. In this case, the number concentration N (particles/m³) is calculated from the mass concentration C (µg/m³) via:

$$N = \frac{C}{\frac{4}{3}\pi r^3 \rho} \cdot 10^9 \tag{S15}$$

We explored the following parameter ranges based on literature observations and experimental feasibility, where $r_{aerosol}$ = 1.0 µm, r_{MP} = 1 - 50 µm, and ε = 1.0 m²/s³. While this spherical assumption is appropriate for deliquescent nitrate aerosols and approximately spherical microplastics, we note that many airborne MPs occur as irregular fragments, sheets, or fibers. Such morphologies would alter the effective collision cross-section, diffusion coefficients, and gravitational settling velocities, potentially increasing or decreasing the collision kernels relative to the spherical case.

Collision probability

To obtain a collision probability, we used:

$$P(t) = 1 - \exp\left(-\beta_{total} \cdot N_a \cdot t\right) \tag{S16}$$

This yields the probability that a given MP will collide with any nitrate aerosol. Supplementary Fig. 28 illustrates how cumulative probability scales with turbulence intensity and concentration ratios as a function of the radius of microplastics. The observation supports the hypothesis that airborne MPs collide with and can potentially integrate into aqueous aerosol particles under atmospheric-relevant conditions, even for low-particle concentration regimes (C_a and C_p = 0.5 µg/m³). This facilitates the

subsequent physical encapsulation or photochemical aging process. This collision model provides a basis for interpreting plausible MP-in-aerosol systems in the atmosphere.

Supplementary Tables:

Supplementary Table 1 | Summarization of the nanosecond transient absorption spectrometry (NTAS) signals

Signal Assignments	Notes	Ref.
Ground state bleaching (GSB) signal	Under the influence of pump light radiation, certain molecules move from the ground state to the excited state. This transition decreases the number of particles that remain in the ground state, resulting in weaker ground-state absorption in the excited sample compared to the incident light. Consequently, the excited sample molecules generate a negative signal peak.	[43]
Stimulated radiation (SE) signal of excited states	When a sample molecule is excited by pump light and transitions to an excited state, it is then exposed to probe light. The stimulated radiation causes the molecule to return to the ground state, triggered by light of a specific wavelength. This process typically results in a signal intensity that is greater than that of spontaneous radiation, leading to the appearance of a negative signal peak.	[43]
Absorption of excited states (AES) signal	A small number of molecules that have already been excited to an excited state by the pump light can be further excited to an even higher energy level by the probe light. As a result, the transmitted light passing through the sample is attenuated, leading to the observation of a positive signal peak.	[43]
Photoproduct absorption (PA) signal	A process occurs in which a sample molecule, initially excited by pump light and transitioning to a higher-energy excited state, returns to the ground state through a series of normal relaxation processes. Subsequently, it absorbs probe light to excite a transition to an even higher-energy excited state, resulting in a positive signal peak.	[43]
$(NO_3^-)^*$	$NO_3^- \xrightarrow{h\nu} (NO_3^-)^* \rightarrow ONOO$, with maximum adsorption at 300 mm	[44]
$NO_2^-/O^{\cdot-}$	$(NO_3^-)^* \rightarrow NO_2^- + O^{\cdot}$, NO_2^- with its maximum adsorption at 410 mm, $O^{\cdot-}$ with its maximum adsorption at ~235 mm	[44]
NO^-	NO^- with its absorbance covering from 250 to 310 nm	[44]

Supplementary Table 2 | Summary for browning processes and corresponding conditions for determining MAC values.

Browning Process	Precursor	Condition Note	Ref.
Microplastics, nitrate, *hv*	Microplastics	Microplastics + Nitrate + *solar-relevant irradiation* + 3h	This* Work
Catechol, nitrite	Phenol	Catechol + Nitrite 6h	[45]
Toluene, ·OH + NO$_x$	Benzenes	Toluene + NO$_x$ + ·OH	[46]
1-Methylnaphthalene (MN) and Longifolene (LG)-Derived, NH$_3$+NO+H$_2$O$_2$	Others	1-Methylnaphthalene or Longifolene+NH$_3$+NO+H$_2$O$_2$	[47]
	Others	1-Methylnaphthalene or Longifolene + NH$_3$ + NO + HONO	
Pyrrole, NO$_2$ + O$_3$	Heterocyclic Aromatic Compounds	Condition: NO$_2$ + O$_3$ + RH < 20%	[48]
2-methylpyrrole, NO$_2$ + O$_3$		Reaction time: 1 h	
Ethylbenzene, H$_2$O$_2$ + UV + NO$_x$	Benzenes	Ethylbenzene or β-pinene + H$_2$O$_2$ + UV + NO$_x$	[49]
β-pinene, H$_2$O$_2$ + UV + NO$_x$	VOCs		
MG-MA MG-DA MG-TA	Others	Methylglyoxal (MG) + methylamine (MA)/dimethylamine (DA) /trimethylamine (TA) + Sonicated for ~5 h	[50]
GL-MA GL-DA GL-TA	Others	Glyoxal (GL) + methylamine (MA)/dimethylamine (DA) /trimethylamine (TA) + Sonicated for ~5 h	
Furan, NH$_4^+$	Heterocyclic Aromatic Compounds	Ammonium Sulfate + Furan/Pyrrole Condition: RH <20% or RH ~50%	[51]
Pyrrole, NH$_4^+$	Heterocyclic Aromatic Compounds		
Ambient BrC from biomass, *hv*	Others	Ambient BrC + UVB photolysis Condition: 20 h	[52]
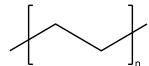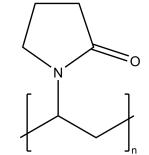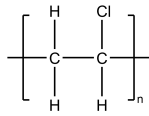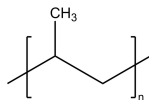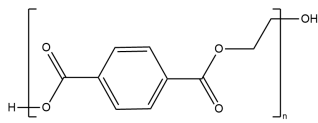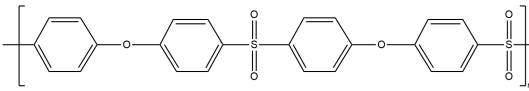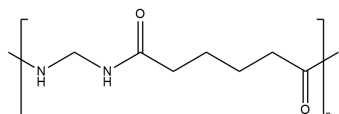
	Others	Ambient BrC + UVB + H_2O_2 Condition: 20 h	
Naphthalene, ·OH	Polycyclic Aromatic Hydrocarbons	Naphthalene + ·OH Condition: 30–40% RH	[53]
Guaiacol, ·OH	Phenol Compounds	Guaiacol + ·OH Condition: 30–40% RH	
Tricyclo[5.2.1.02,6] decane, ·OH	Heterocyclic Aromatic	Tricyclo[5.2.1.02,6]decane + ·OH Condition: 30–40% RH	
a-Pinene, ·OH	Biogenic Volatile Organic Compounds (BVOCs)	a-Pinene + ·OH Condition: 30–40% RH	
Primary Coal Combustion Particles	Others	Bituminous Coals or Anthracite Coals Condition: Stove Burning	[54]
Coal Combustion Particles after Aging		Bituminous Coals or Anthracite Coals Condition: Stove Burning+ OH radicals	
Phenol, ·NO$_3$	Phenol	Seed Aerosol NaCl + Precursor+ NO_2+O_3 Condition: RH = 45–55%	[55]
Catechol, ·NO$_3$			
3-methylcatechol, ·NO$_3$			
4-methylcatechol, ·NO$_3$			
Guaiacol, ·NO$_3$			
Naphthalene, ·OH	Polycyclic Aromatic Hydrocarbons	Condition: RH = 25–62 % ·OH Source: O_2 + UV lamps (185 and 254 nm) ·NO$_3$ Source: NO_2 + O_3	[56]
Naphthalene, ·NO$_3$			
Acenaphthylene, ·OH			
Acenaphthylene, ·NO$_3$			
Fluorene, ·OH			
Phenanthrene, ·OH			
Phenanthrene, ·NO$_3$			
2-methylfuran, ·OH	Heterocyclic Aromatic		
2,5-			
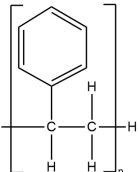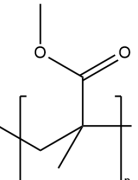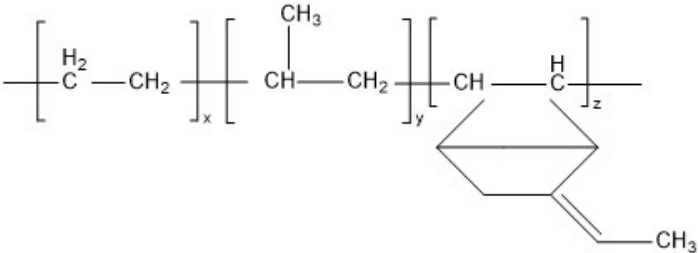
dimethylfuran, ·OH	Compounds		
2,5-dimethylfuran, ·NO$_3$			
Furan, ·OH			
Furan, ·NO$_3$		Precursor + NO + O$_3$ Condition: RH=2–16%	[57]
Pyrrole, ·NO$_3$	Heterocyclic Aromatic Compounds		
Thiophene, ·NO$_3$			
α-Pinene, NO$_x$ α-Pinene, ·OH	BVOCs	Seed Aerosol Ammonium Sulfate + Precursor + ·OH or + NO$_x$; ·OH Source: H$_2$O$_2$ Photolysis; NO$_x$ Source: NO	[58]
β-Caryophyllene, NO$_x$ β-Caryophyllene, ·OH	VOCs		
1,3,5-Trimethylbenzene, ·OH	Benzenes		
1,2,4-Trimethylbenzene, NO$_x$ 1,2,4-Trimethylbenzene, ·OH			
m-Xylene, NO$_x$ m-Xylene, ·OH			
Toluene, NO$_x$ Toluene, ·OH			
Ethylbenzene, NO$_x$ Ethylbenzene, ·OH			
Benzene, NO$_x$ Benzene, ·OH			
Naphthalene, NO$_x$ Naphthalene, ·OH	Polycyclic Aromatic Hydrocarbons		
m-Cresol, NO$_x$ m-Cresol, ·OH	Phenol Compounds		
Phenol, ·OH+NO$_x$	Phenol Compounds	Precursors + H$_2$O$_2$ + NO + UV Condition: RH < 10%	[59]
1-	Polycyclic		

methylnaphthalene, ·OH+NO$_x$	Aromatic Hydrocarbons
Longifolene, ·OH+NO$_x$	BVOCs
Phenol+1-methylnaphthalene, ·OH+NO$_x$	Phenol Compounds/Polycyclic Aromatic Hydrocarbons
Longifolene+1-methylnaphthalene, ·OH+NO$_x$	BVOCs/Polycyclic Aromatic Hydrocarbons

*The MAC value at 365 mm (~0.62 m^2 g^{-1}) of the phenolic compound undergoing nitration in our experimental system falls in the range with those reported in the literature (0.4-0.8 m^2 g^{-1})[60], which suggests that our method yields results consistent with previous studies and does not artificially inflate the light absorption estimates.

Supplementary Table 3 | Summarization of the chemical structure, size distribution, and OC conversion efficiency of MPs in this study.

Microplastic Types	Molecular Formula	Chemical Structure	*Size Distribution (µm)	CCj
Polyethylene (PE)	$(C_2H_4)_n$		40±10	0.44
Polyvinylpyrrolidone (PVP)	$(C_6H_9NO)_n$		92±45	0.43
Polyvinyl Chloride (PVC)	$(C_2H_3Cl)_n$		152±35	0.15
Polypropylene (PP)	$(C_3H_6)_n$		182±60	0.16
Polyethylene Terephthalate (PET)	$(C_{10}H_8O_4)_n$		62±46	0.13
Polyethersulfone (PES)	$(C_6H_4SO_2)_n$		103±77	0.09
Polyamide (PA)	$(C_{12}H_{22}N_2O_2)_n$		19±11	0.09

			Size (nm)*	
Polystyrene (PS)	$(C_8H_8)_n$		26±9	0.12
Polymethyl Methacrylate (PMMA)	$(C_5H_8O_2)_n$		34±20	0.09
Ethylene–Propylene–Diene Monomer Rubber (ER)			81±60	0.15

*The size distribution of each MPS was determined by measuring the diameters of at least 50 individual particles.

Supplementary Table 4 | Summarization of the relevant information for calculating the contribution of nitrate photolysis aging of airborne microplastics in 16 cities worldwide.

Region/ Country	Location/ Geographic Information	Concentrations of Water-soluble ions of concern and meteorological factors	Microplastic Concentration	Relative Abundance of each MP (%)	WSOC/ WIOC Content ($\mu g/m^3$)	Light Absorption Coefficient /Efficiency ($m^2\ g^{-1}$)	Ref
Seoul, South Korea	37.57° N,126.98° E	$[NO_3^-]$ = 9.0 ± 5.6 $\mu g/m^3$ $[SO_4^{2-}]$ = 4.1 ± 2.3 $\mu g/m^3$ $[NH_4^+]$ = 4.4 ± 2.5 $\mu g/m^3$ Temperature Range = 290–293 K (291.5 K) RH = 73.2 ± 8.8% Aerosol Liquid Water Content (ALWC) = 18.8 ± 17.4 $\mu g/m^3$	Total Range = 0.51–9.88 particles/m^3 (n=90) Average = 2.235 ± 1.28 particles/m^3 (n=90) Fibers (90%) = 100 μm–1000 μm Fragments (8%) = 10 μm–1000 μm Film (2%) = 50 μm–1000 μm NC_{MPS}= ~0.37 $\mu g/m^3$ $\mu g/m^3$	PE=37 PP=26.7 PES=13.6 PA=9.10 PS=4.4 AR=2.4 PVC=1.7 PTFE=1.9 ALK=2.3 PU=0.9	OC = ~7.98 WSOC =4.7 ± 0.8 WIOC = ~3.28	Average$_{WSOC}$=0.73 Average$_{WSIC}$=0.95 *Average$_{overall}$ = 0.82	28,61 ,62
Islamabad, Pakistan	33.738045° N, 73.084488° E	$[NO_3^-]$ = 15.25 ± 12.90 $\mu g/m^3$ $[SO_4^{2-}]$ = 37.5 ± 21.94 $\mu g/m^3$ $[NH_4^+]$ = 13.0 ± 1.87 $\mu g/m^3$ Temperature = 310 K RH = 40–60% (50%)	Outdoor air samples= (0.93 ± 0.32 items/m^3) <50 μm: 31.5% 50–100 μm: 14.2% 100–250 μm: 19.5% 250–500 μm: 27.8% 500–1000 μm: 4.8% Sheet = 3% Fragment = 30.7%	PET=42.2 PE=30.0 PS=14.4 Others=13.4	OC = 30.3 WSOC = 21.4 WIOC = 8.9	†Average$_{WSOC}$: 0.80±0.40 ‡Average$_{WIOC}$= 1.56 *Average$_{overall}$ = 1.02	63-68

			Fiber = 66.3% NC_{MPS}= ~5.55 µg/m³				
São Paulo, Brazil	23.55° S, 46.63° W	$[NO_3^-]$ = 1.29 ± 1.12 µg/m³ $[SO_4^{2-}]$ = 2.57 ± 1.11 µg/m³ $[NH_4^+]$ = 1.08 ± 0.61 µg/m³ PO_4^{3-}= 0.037 ± 0.01 µg/m³ Cl^-= 0.16 ± 0.15 µg/m³ Na^+=0.11 ± 0.055 K^+=0.44 ± 0.12 Mg^{2+}=0.035 ± 0.005 Ca^{2+}=0.233 ‖Temperature = 296 K RH = 70.85%	Outdoor air samples= 123.20 ± 47.09 MPs/m2/day MP lengths range from 100 and 200 µm; The fragment was the dominant morphology (74%). Film was the second most common shape (13%), followed by granule (8%) and foam (5%); NC_{MPS}: 0.2–2.1 µg/m³ (1 µg/m³)	PE=67 PET=25 PS=85	WSOC = 26.3 WIOC = 6.92	Average$_{WSOC}$=2.1 ‡Average$_{WSIC}$=4.1 *Average$_{overall}$ = 2.52	[66,69-72]
California, United States	36.78° N, 119.42° W	$[NO_3^-]$ = 8.32 ± 5.06 µg/m³ $[SO_4^{2-}]$ = 3.92 ± 0.50 µg/m³ $[NH_4^+]$ = 3.23 ± 1.41 µg/m³ Temperature = 291 K RH = 66.5% §Aerosol Water = ~3.5 µg/m³	Outdoor air samples=0.6 ± 0.6 fibers and 5.6 ± 3.2 fragments m⁻³ Fiber length (µm) = 616 ± 536 (55%) Fragment size (µm) = 104 ± 64 (45%) NC_{MPS}: 0.6–6.4 µg/m³ (3.4 µg/m³)	PVC-HS=57 PS=10 Polymeric=10	¶OC=5.41±1.21 WSOC= 3.06±0.96 WIOC= 2.35± 0.69	Average$_{WSOC}$=0.64±0.55 Average$_{WSIC}$=1.51±0.25 *Average$_{overall}$ = 1.02	[33,73-76]
Queensland, Australia	23.0° S, 145.0° E.	Na^+= 0.27 ± 0.063 µg/m³ NH_4^+= 0.19 ± 0.041	Outdoor air samples = 0.17 ± 0.06	PET=59 PE=25	OC=4.19±0.20	Averaged from values predicted with	[77-83]

		$\mu g/m^3$ $K^+ = 0.052 \pm 0.044$ $\mu g/m^3$ $Mg^{2+}=0.028 \pm 0.020$ $\mu g/m^3$ $Ca^{2+}=0.11 \pm 0.077$ $\mu g/m^3$ $Cl^-=0.13 \pm 0.011$ $\mu g/m^3$ $NO_2^-=0.009 \pm 0.003$ $\mu g/m^3$ $NO_3^-=0.30 \pm 0.21$ $\mu g/m^3$ $SO_4^{2-}=0.60 \pm 0.088$ $\mu g/m^3$ $C_2O_4^{2-}=0.066 \pm 0.018$ $\mu g/m^3$ $PO_4^{3-}=0.015 \pm 0.015$ $\mu g/m^3$ $F^-=0.010 \pm 0.012$ Acetate=0.19 ± 0.198 Formate=0.091 ± 0.027 Temperature = 313 K RH = 67%	particles/m^3 NC_{MPS}: 0.03–0.15 $\mu g/m^3$ (0.04 $\mu g/m^3$)	PA=10 PP=3 PAN=2 PVC=1	WSOC=1.09 ±0.68 [#]WIOC=3.10	effective radius (re) at different RH values:7.50 ± 3.42 $Abs_{WSOC}=0.213$ Mm^{-1}; $Average_{WSOC}=0.20$; [‡]$Average_{WSIC}=0.39$	
Taiwan, China	23.7° N, 120.9° E	[**]$F^-=0.04 \pm 0.01$ $\mu g/m^3$ [**]$Cl^-=1.07 \pm 0.01$ $\mu g/m^3$ [**]$NO_3^-=2.26 \pm 1.23$ $\mu g/m^3$ [**]$SO_4^{2-}=9.12 \pm 5.79$ $\mu g/m^3$ [**]$Na^+=0.67 \pm 0.13$ $\mu g/m^3$ [**]$NH_4^+=3.17 \pm 1.48$	Outdoor air samples = 28 ± 24 MPs/m^3; NC_{MPS}: 1–3 $\mu g/m^3$ (2 $\mu g/m^3$)	AR=40 Other=28 Rubber= 13 PVC=12 PVA=3 PEI=2 PUR=2	OC = 2.21 ± 1.40 C; WSOC= 1.21 ± 0.79; WIOC= ~1;	$Average_{WSOC}$ = 6.05 ± 0.56; $Average_{WIOC}$ = 5.29 ± 0.61; *$Average_{overall}$ = 5.71	84-88

		$\mu g/m^3$ [**]K^+=0.60 ± 0.04 $\mu g/m^3$ [**]Mg^{2+}=0.31 ± 0.25 $\mu g/m^3$ [**]Ca^{2+}=0.60 ± 0.08 $\mu g/m^3$ Temperature = 294.6 K RH = 78-85% (81.5%)					
Wenzhou, China	7.87° N, 120.70° E	[§§][NO_3^-] = 5.85 ± 5.85 $\mu g/m^3$ [§§][SO_4^{2-}] = 4.9 ± 2.18 $\mu g/m^3$ [§§][NH_4^+] = 3.43 ± 2.37 $\mu g/m^3$ [§§]Temperature = 293 K [§§]RH = 82±4.24%	outdoor air samples = 189 ± 85 n/m^3; urban areas = 224 ± 70 n/m^3 rural areas = 101 ± 47 n/m^3; NC_{MPS}: 8-23 $\mu g/m^3$ (15 $\mu g/m^3$)	PE=26.8 PS=17.8 Polyester= 17.2 PA≈4 PP≈16 PVC≈10 Others≈8	$PM_{2.5}$=41.64 ±15.18; [††]OC = 12.5; [¶¶]WSOC= 4.96; WIOC=7.54	Abs_{BrC}=0.55 Mm^{-1}; [‖‖]$Abs_{WSOC+WIOC}$=0.73 Mm^{-1}; $Average_{WSOC}$=0.04; $Average_{WSIC}$=0.072; [*]$Average_{overall}$ = 0.06	36,89 -91
Sri Lanka	7.87° N, 80.77° E	[***]Nitrate Concentration = ~2 $\mu g/m^3$; [†††]SO_4^{2-} = ~2.1$\mu g/m^3$; [†††]NH_4^+ = ~1.4 $\mu g/m^3$; Temperature = ~300 K; RH = ~76%	Outdoor air samples=0.23 particles/m^3; NC_{MPS}: 0.3 $\mu g/m^3$ (0.02–0.56 $\mu g/m^3$)	PET= 48; PES=34; Nylon=14; Andacrylic= 4	OC =22.00; [‡‡‡]WSOC=10 .4; WIOC=11.6	Abs_{BrC}=0.4-0.6 Mm^{-1} (Mean 0.5 Mm^{-1});[‖‖]$Abs_{WSOC+WIOC}$= 0.67 Mm^{-1};$Average_{WSOC}$=0 .021 $Average_{WSIC}$=0.039;[*] $Average_{overall}$ = 0.03	37,92
Xiamen, China	24.48° N, 118.09° E	[‖‖‖]Na^+= 0.43 ± 0.05 $\mu g/m^3$ [‖‖‖]NH_4^+=0.56 ± 0.00 $\mu g/m^3$ [‖‖‖]Cl^-=0.45 ± 0.04 $\mu g/m^3$ [‖‖‖]NO_3^-=0.55 ± 0.01	Range: 0 to 0.062 items m^{-3} Average: 0.011 ± 0.012 items m^{-3};NC_{MPS}: 0.25 $\mu g/m^3$ (0.03–0.47 $\mu g/m^3$)	Tourist area: polymer=44 .9 PET=37.8 PE=5.1	[§§§]WSOC= 1.68 ± 1.05;WIOC= 1.15 ± 0.77	[¶¶¶]$Average_{WSOC}$ = 0.34;$Average_{WIOC}$ =0.66;[*]$Average_{overall}$ = 0.47	38,93 -95

Location	Coordinates	Chemical composition	MP deposition / concentration	Polymer types	OC / WSOC	Abs / optical	Ref.
		μg/m³ ⅢⅢⅢⅢSO_4^{2-}=0.53 ± 0.01 μg/m³ Temperature = ~300 K RH = ~76%		PP =5.1 PS=5.1 PE-PP=2.0 urban-rural fringe area: PET=34.7 PE=17.3 PP=15.3 PES=10.2 PS=9.2 PE-PP=8.2 PVC=4.1 PMMA=1.0			
Norway	60.47° N, 8.47° E	****SO_4^{2-}=0.110 ± 0.055 ****NO_3^-=0.079 ± 0.062 ****NH_4 =0.342 ± 0.121 ****Mg^{2+}=0.041 ± 0.028 ****Ca^{2+}=0.037 ± 0.018 ****K^+=0.043 ± 0.021 ****Cl^-=0.425 ± 0.314 ****Na^+=0.323 ± 0.230 Temperature = ~276.6 K RH = 75%	MP deposition rates (μg/m²/d)=159 ± 295 NC_{MPS}: 0.3 μg/m³ (0.03–0.56 μg/m³)	Nylon-N6=42 SBR=22 PMMA=13 PET=8 PU=6 PVC=5 PS=1.6 Others=2.5	OC=0.57–0.58 (0.575) ††††WSOC= 0.36 WIOC= 0.22	Abs_{BrC}=0.1-0.4 Mm⁻¹ (Mean 0.25 Mm⁻¹); ⅢⅢⅢ$Abs_{WSOC+WIOC}$= 0.33 Mm⁻¹; $Average_{WSOC}$=0.49; $Average_{WSIC}$=0.93; *$Average_{overall}$ = 0.66	34,96-99
Four Cities, China	Beijing: 39.90° N, 116.40° E Shanghai: 31.23° N,	[Cl^-]$_{BJ}$=0.33 ± 0.09 [NO_3^-]$_{BJ}$=6.18 ± 2.30 [SO_4^{2-}]$_{BJ}$ =5.51 ± 2.63 [Na^+]$_{BJ}$=0.19 ± 0.03 [K^+]$_{BJ}$=0.28 ± 0.08 [Ca^{2+}]$_{BJ}$=2.10 ± 0.65	Beijing (BJ)=393 ± 112 items/m³ Shanghai (SH)=267 ± 117 items/m³ Hangzhou (HZ) =246 ± 78 items/m³	PE≈21 PET≈12 PS≈32 PP≈10 PA≈5 PVC≈8	‡‡‡‡OC_{BJ}=9.27±5.39 $WSOC_{BJ}$=3.54±1.99 $WIOC_{BJ}$=7.28	SH=0.35–0.81 (0.56 ± 0.11) BJ=0.71-1.79(1.25±0.54) §§§§NJ_{WSOC} = 0.65	40,62,89,93,100-112

121.47° E	$[Mg^{2+}]_{BJ}$=0.38 ± 0.19 $[NH_4^+]_{BJ}$=4.68 ± 1.91	Nanjing (NJ) = 177 ± 59 items/m^3	Other≈11		NJ_{WIOC} = 0.61
Hangzhou: 30.27° N, 120.15° E	Temperature Range$_{BJ}$ = 290. K RH_{BJ} = 56%	NC$_{MPS\_BJ}$: ~74 µg/m^3 NC$_{MPS\_SH}$: ~65 µg/m^3 NC$_{MPS\_HZ}$: ~60 µg/m^3		OC_{HZ}=12.1 $WSOC_{HZ}$=4.80 ± 4.20 $WIOC_{HZ}$=7.3	*Average$_{overall\_NJ}$ = 0.64 Abs$_{BrC\_HZ}$=0.5-0.7 Mm^{-1} (Mean 0.6 Mm^{-1})
Nanjing: 32.06° N, 118.79° E	$[NO_3^-]_{SH}$ = 8.10 ± 7.78 µg/m^3 $[SO_4^{2-}]_{SH}$ = 12.00 ± 7.35 µg/m^3 $[NH_4^+]_{SH}$ = 6.15 ± 5.44 µg/m^3 $[Mg^+]_{SH}$ = 0.15 ± 0.07 µg/m^3 $[Ca^+]_{SH}$ = 1.15 ± 0.78 µg/m^3 Temperature Range$_{SH}$ = 289K RH_{SH} = 75%	NC$_{MPS\_NJ}$: ~55 µg/m^3		OC_{NJ}=6.1 ± 2.5 ¶¶¶¶$WSOC_{NJ}$= 3.97 $WIOC_{NJ}$=2.13 OC_{SH}=4.9 $WSOC_{SH}$=2.1 $WIOC_{SH}$=2.8	‖‖Abs$_{WSOC+WIOC\_HZ}$= 0.8 Mm^{-1} HZ_{WSOC} = 0.042 HZ_{WIOC} = 0.079 *Average$_{overall\_HZ}$ = 0.064
	$[F^-]_{HZ}$ = 0.1 ± 0.1 µg/m^3 $[Cl^-]_{HZ}$ = 4.3 ± 1.9 µg/m^3 $[NO_3^-]_{HZ}$ = 12.6 ± 5.4 µg/m^3 $[SO_4^{2-}]_{HZ}$ = 18.1 ± 7.1 µg/m^3 $[Na^+]_{HZ}$ = 1.9 ± 0.7 µg/m^3 $[NH_4^+]_{HZ}$ = 7.6 ± 3.7 µg/m^3				

$[K^+]_{HZ} = 0.8 \pm 0.6 \ \mu g/m^3$

$[Mg^{2+}]_{HZ} = 0.2 \pm 0.1 \ \mu g/m^3$

$[Ca^{2+}]_{HZ} = 1.5 \pm 0.7 \ \mu g/m^3$

$\text{Temperature Range}_{HZ} = 290K$

$RH_{HZ} = 75\%$

$[NO_2^-]_{NJ} = 0.50 \pm 0.10 \ \mu g/m^3$

$[F^-]_{NJ} = 0.45 \pm 0.05 \ \mu g/m^3$

$[NO_3^-]_{NJ} = 8.25 \pm 3.75 \ \mu g/m^3$

$[Cl^-]_{NJ} = 1.75 \pm 0.75 \ \mu g/m^3$

$[SO_4^{2-}]_{NJ} = 19.00 \pm 2.00 \ \mu g/m^3$

$[NH_4^+]_{NJ} = 8.00 \pm 1.00 \ \mu g/m^3$

$[Ca^{2+}]_{NJ} = 3.50 \pm 0.50 \ \mu g/m^3$

$[Na^+]_{NJ} = 1.90 \pm 0.10 \ \mu g/m^3$

$[K^+]_{NJ} = 1.15 \pm 0.35 \ \mu g/m^3$

$\text{Temperature Range}_{NJ} = 289K$

$RH_{NJ} = 74\%$

		Nitrate Concentration$_{HZ}$ = 6.98 ± 6.09 µg/m³					
France	46.60° N, 1.88° E	[†††††]NH_4^+=1.42 ± 0.32 µg/m³ NO_3^-=2.60 ± 0.77 µg/m³ SO_4^{2-}=1.78 ± 0.39 µg/m³ Temperature = ~282 K RH = ~78%	Range = 0.09–0.66 microplastics particles/m3 NC$_{MPS}$: 0.42 µg/m³ (0.15–1.04 µg/m³)	Polyethylene (LD/HDPE) =44 PS=18 PVC=15 PET=14 PP=10	[####]WSOC= 5.64 ± 5.42 [‡‡‡‡‡]WIOC= 3.07	[*****]Abs$_{WSOC+WSIC}$=0.1-0.2 Mm^{-1} (Mean 0.15 Mm^{-1});[‖‖‖]Abs$_{WSOC+WIOS}$= 0.27 Mm^{-1};Average$_{WSOC}$ = 0.02;Average$_{WIOC}$ = 0.04; *Average$_{overall}$ = 0.027	[109,113-115]
India	20.59° N, 78.96° E	[§§§§§]F^-=0.27 ± 0.04 Cl^-=3.25 ± 0.21 NO_3^-=1.85 ± 1.38 SO_4^{2-}=12.02 ± 2.31 Na^+=0.98 ± 0.22 NH_4^+=2.58 ± 1.32 K^+=2.79 ± 1.08 Ca^{2+}=1.67 ± 0.41 Temperature = 298 K RH = ~69%	Average$_{2016}$= 1.30 ± 0.14 n/m³ Average$_{2020}$= 1.46 ± 0.12 n/m³ NC$_{MPS}$: 0.34 µg/m³	PVC=31 PMMA=24 PES=15 Styrene Butyl Methacrylate (SBMA)=11 Polyacetal (POM)=9 Polyarylate (PAR)=3 PUR=2 Acrylonitrile (AN)=2, Epoxy resin	OC=1.6-14.7 (Mean=8.25) WSOC=0.85-8.2(Mean=4.53) WIOC=3.72	Average$_{WSOC}$ = 1.5 ± 0.6;AverageW$_{IOC}$ = 2.07 ± 0.8;*Average$_{overall}$ = 1.76	[42,80,116-118]

	(ER)=2
	Polyvinyl
	Alcohol
	(PVAL)=1

[*]Average$_{overall}$ = (water-soluble organic carbon (WSOC) × Average$_{WSOC}$) + (water-insoluble organic carbon (WIOC) × Average$_{WIOC}$)/(WSOC + WIOC)

[†]WSOC$_{average}$ is derived from the mean value of WSOC$_{winter}$ = 35.2 ± 14.9 and WSOC$_{summer}$ = 7.5 ± 1.7 (Shahid et al., 2015)

[‡]The MAC values of WIOC at 365 nm were approximately 2.3 and 1.6 times higher than the values of WSOC for the biomass and ambient aerosols, and a mean of 1.95 was thus applied (Yan et al., 2020).

[‖]Average from PRB and SPA sampling sites (Vieira-Filho et, 2016).

[¶]The value averaged from six sampling sites (Kim et al., 2007).

[#]WIOC = OC - WSOC

[**]We averaged the concentration of each constituent in two sampling sites, NEM-Inland and SLBs-Inland (Tsai et al., 2011).

[††]OC accounts for 30% of the total mass of PM$_{2.5}$ (Ram et al., 2011).

[§§]We adopted the averaged constituent concentrations and meteorological conditions determined in NB sites in two season periods (Wang et al., 2023).

[‖‖]Abs$_{BrC}$ accounts for 75% of Abs$_{WSOC+WIOC}$ on average at 365 nm (Zhang et al., 2018).

[¶¶]We adopted a WSOC/OC ratio of 0.4 reported for Hangzhou.

[##]Abs(WSOC + WSIC) = MAE$_{WSOC\_365}$ × WSOC + MAE$_{WIOC\_365}$ × WIOC = 0.55 M m^{-1}. Given that MAE$_{WIOC\_365}$ is 1.9 times of MAE$_{WIOC\_365}$.

[***]The nitrate concentration values for the Sri Lanka region were estimated based on the RegCCMS simulation. The area corresponds to a concentration of ~2 μg/m^3 (Wang et al., 2010).

[†††]SO$_4^{2-}$ and NH$_4^+$ concentrations in Sri Lankan PM$_{2.5}$ were estimated using the provided NO$_3^-$ concentration of 2 μg/m^3 and regional PM$_{2.5}$ composition data from South Asia. Assuming a total PM$_{2.5}$ concentration of 24 μg/m^3 (based on 2019 Sri Lankan PWM), SO$_4^{2-}$ was approximated at 2.1 μg/m^3 by scaling South Asian SO$_4^{2-}$ contributions (3.9 μg/m^3) and adjusting for chemical balance. NH$_4^+$ was calculated as 1.4 μg/m^3, assuming full neutralization of SO$_4^{2-}$ and NO$_3^-$ as (NH$_4$)$_2$SO$_4$ and NH$_4$NO$_3$, with mass ratios of 0.375 (NH$_4^+$/SO$_4^{2-}$) and 0.2903 (NH$_4^+$/NO$_3^-$), respectively. Estimates align with a total ionic contribution of 5.5 μg/m^3 (22.92% of PM$_{2.5}$).

[‡‡‡]The WSOC/OC and WIOC/OC were derived from the sampling in Thumba (8.55°N, 77°E) (Aswini et al., 2019), and the resulting ratios are 0.425 ± 0.1 and 0.575 ± 0.1, respectively.

[§§§]Mean ± standard deviation of the concentration of water-soluble constituents in the sampling campaign in the year 2022.

[‖‖‖]PM$_{2.5}$ concentrations were estimated by applying the average PM$_{2.5}$/PM$_{10}$ ratio (59.47%) to PM$_{10}$ values (Li et al., 2013).

¶¶¶The MAE$_{365}$ value for Xiamen was estimated based on the ratio of organic matter (OM) concentrations between Xiamen and Beijing, using the mean MAE$_{365}$ values measured during winter and summer in Beijing (Tao et al., 2017).

****Average value derived from 5 sampling sites including B irkenes ll, Hurdal, Karvatn, Tustervatn, Zeppelin.

††††We adopted the WSOC/OC ratio of 0.62 determined in Hyytialä 2007 Campaign (Xuguang Chi, 2009).

‡‡‡‡Averaged from the non-polluted days and polluted days (Li et al., 2019)

§§§§Averaged from warm and cold seasons (Huang et al., 2020)

‖‖‖‖SOC = 3.5 μg/m^3 (Wang et al., 2021), and we tentatively assumed a WSOC of 3 μg/m^3 for simplicity.

¶¶¶¶For simplicity, we tentatively assumed the WSOC/WIOC corresponding to the WSOM/WIOM reported by Liu et al., 2021.

####Static analysis for all plots shown in Figures 11 and 12 in this work (Jaffrezo et al., 2005)

*****This value was speculated from the simulated zonal averaged annual mean absorption at 365 nm (Mm^{-1}) for all sources (Zhang et al., 2019).

†††††Averaged concentration level from 2016-2020.

‡‡‡‡‡The WSOC fraction is stable at 54.8±7.7% and 75.9±6.3% for temperatures in the ranges −10 to +3∘C and 12 to 24∘C, and we applied a mean fraction of 65.4%, and the resulting WIOC fraction is 34.6%.

§§§§§Averaged from Commercial area, Industrial area, and Rural area (Saxena et al., 2024)

Supplementary Table 5 | Summarization of the relevant information for calculating the concentration of nitrate aerosol and corresponding correction factors applied for calculating light-absorbing strength derived from aged microplastics in 16 cities worldwide.

Region/Countries	Model Input	Key Parameter Output	NO_3^-(M) and MPs Concentration (µg/µg aerosol water) 15 mg MPs/200 g water = 7.5×10^{-5} µg MPs/µg water
South Korea	$[NO_3^-]$ = 9.0 ± 5.6 µg/m^3 $[SO_4^{2-}]$ = 4.1 ± 2.3 µg/m^3 $[NH_4^+]$ = 4.4 ± 2.5 µg/m^3 Temperature =291.5 K RH = 0.73	[WATER] = 7.5 µg/m^3 $[NO_3^-]$ = 1.97 µg/m^3	NO_3^-(M) = 4.23 Airborne [MPs]/[WATER] = 0.37 µg/75.01 µg $=$ 4.93×10^{-3} µg/µg
Pakistan	$[NO_3^-]$ = 15.25 ± 12.90 µg/m^3 $[SO_4^{2-}]$ = 37.5 ± 21.94 µg/m^3 $[NH_4^+]$ = 13.0 ± 1.87 µg/m^3 Temperature = 310 K RH = 0.5	[WATER] = 24.6 µg/m^3 $[NO_3^-]$ = 15.03 µg/m^3	NO_3^-(M) = 9.88 Airborne [MPs]/[WATER] = 5.55 µg/24.6 µg $=$ 0.23 µg/µg
São Paulo, Brazil	$[NO_3^-]$ = 1.29 ± 1.12 µg/m^3 $[SO_4^{2-}]$ = 2.57 ± 1.11 µg/m^3 $[NH_4^+]$ = 1.08 ± 0.61 µg/m^3 Cl$^-$= 0.16 ± 0.15 µg/m^3 Na$^+$=0.11 ± 0.055 µg/m^3 K$^+$=0.44 ± 0.12 µg/m^3 Mg^{2+}=0.035 ± 0.005 µg/m^3 Ca^{2+}=0.233 µg/m^3 Temperature = 296 K	[WATER] = 4.152 µg/m^3 $[NO_3^-]$ = 1.577×10^{-2} µg/m^3	NO_3^-(M) = 4.93 Airborne [MPs]/[WATER] = 1 µg/4.152 µg $=$ 0.24 µg/µg

	RH = 0.71		
California, United States	$[NO_3^-]$ = 8.32 ± 5.06 µg/m³ $[SO_4^{2-}]$ = 3.92 ± 0.50 µg/m³ $[NH_4^+]$ = 3.23 ± 1.41 µg/m³ Temperature = 291 K RH = 0.67	[WATER] = 6.314 µg/m³ $[NO_3^-]$ = 6.80 µg/m³	NO_3^-(M) = 6.80 Airborne [MPs]/[WATER] = 3.4 µg/6.314 µg = 0.59 µg/µg
Queensland, Australia	Na^+= 0.27 ± 0.063 µg/m³ NH_4^+= 0.19 ± 0.041 µg/m³ K^+ = 0.052 ± 0.044 µg/m³ Mg^{2+}=0.028 ± 0.020 µg/m³ Ca^{2+}=0.11 ± 0.077 µg/m³ Cl^-=0.13 ± 0.011 µg/m³ NO_3^-=0.30 ± 0.21 µg/m³ SO_4^{2-}=0.60 ± 0.088 µg/m³ Temperature = 313 K RH = 0.67	[WATER] = 1.253 µg/m³ $[NO_3^-]$ = 0.3 µg/m³	NO_3^-(M) = 3.80 Airborne [MPs]/[WATER] = 0.04 µg/1.253 µg = 4.93×10⁻³ µg/µg
Taiwan, China	Cl^-=1.07 ± 0.01µg/m³ NO_3^-=2.26 ± 1.23 µg/m³ SO_4^{2-}=9.12 ± 5.79 µg/m³ Na^+=0.67 ± 0.13 µg/m³ NH_4^+=3.17 ± 1.48 µg/m³ K^+=0.60 ± 0.04 µg/m³ Mg^{2+}=0.31 ± 0.25 µg/m³ Ca^{2+}=0.60 ± 0.08 µg/m³ Temperature = 294.6 K RH = 0.82	[WATER] = 24.8 µg/m³ $[NO_3^-]$ = 2.22 µg/m³	NO_3^-(M) = 1.45 Airborne [MPs]/[WATER] = 2 µg/24.8 µg = 4.93×10⁻³ µg/µg
Wenzhou, China	$[NO_3^-]$ = 5.85 ± 5.85 µg/m³ $[SO_4^{2-}]$ = 4.9 ± 2.18 µg/m³ $[NH_4^+]$ = 3.43 ± 2.37 µg/m³	[WATER] = 20.01 µg/m³ $[NO_3^-]$ = 5.76 µg/m³	NO_3^-(M) = 4.62 Airborne [MPs]/[WATER] = 15 µg/20.01 µg = 4.93×10⁻³ µg/µg

	Temperature = 293 K RH = 82±4.24%		
Sri Lanka	Aerosol Water = ~2.5 µg/m^3 Nitrate Concentration = ~2 µg/m^3 SO_4^{2-} = ~2.1µg/m^3 NH_4^+ = ~1.4 µg/m^3 Temperature = ~300 K RH = ~76%	[WATER] = 5.56 µg/m^3 [NO_3^-] = 1.97 µg/m^3	NO_3^-(M) = 5.70 Airborne [MPs]/[WATER] = 0.3µg/5.56 µg = 4.93×10^{-3} µg/µg
Xiamen, China	Na^+= 0.43 ± 0.05 µg/m^3 NH_4^+=0.56 ± 0.00 µg/m^3 Cl^-=0.45 ± 0.04 µg/m^3 NO_3^-=0.55 ± 0.01 µg/m^3 SO_4^{2-}=0.53 ± 0.01 µg/m^3 Temperature = ~300 K RH = ~76%	[WATER] = 3.42 µg/m^3 [NO_3^-] = 0.54 µg/m^3	NO_3^-(M) = 2.55 Airborne [MPs]/[WATER] = 0.25 µg/3.42 µg = 4.93×10^{-3} µg/µg
Norway	SO_4^{2-}=0.110 ± 0.055 NO_3^-=0.079 ± 0.062 NH_4 =0.342 ± 0.121 Mg^{2+}=0.041 ± 0.028 Ca^{2+}=0.037 ± 0.018 K^+=0.043 ± 0.021 Cl^-=0.425 ± 0.314 Na^+=0.323 ± 0.230 Temperature = ~276.6 K RH = 75%	[WATER] = 2.70 µg/m^3 [NO_3^-] = 7.775×10^{-2} µg/m^3	NO_3^-(M) = 2.03 Airborne [MPs]/[WATER] = 0.3 µg/2.7 µg = 4.93×10^{-3} µg/µg
Five Provinces, China	[Cl^-]$_{BJ}$=0.33 ± 0.09 [NO_3^-]$_{BJ}$=6.18 ± 2.30 [SO_4^{2-}]$_{BJ}$ =5.51 ± 2.63 [Na^+]$_{BJ}$=0.19 ± 0.03	[WATER]$_{BJ}$ = 3.55 µg/m^3 [NO_3^-]$_{BJ}$ = 6.08 µg/m^3 [WATER]$_{TJ}$ = 24.63 µg/m^3	$NO_3^-$$_{BJ}$(M) = 6.08 $NO_3^-$$_{SH}$(M) = 5.63 $NO_3^-$$_{HZ}$(M) = 4.38 $NO_3^-$$_{NJ}$(M) = 4.35

$[K^+]_{BJ} = 0.28 \pm 0.08$

$[Ca^{2+}]_{BJ}]_{BJ} = 2.10 \pm 0.65$

$[Mg^{2+}]_{BJ} = 0.38 \pm 0.19$

$[NH_4^+]_{BJ} = 4.68 \pm 1.91$

Temperature Range$_{BJ}$ = 290 K

RH_{BJ} = 56%

$[Na^+]_{TJ} = 1.0 \pm 0.1$

$[NH_4^+]_{TJ} = 11.2 \pm 0.3$

$[K^+]_{TJ} = 4.0 \pm 0.6$

$[Mg^{2+}]_{TJ} = 0.2 \pm 0.1$

$[Ca^{2+}]_{TJ} = 1.3 \pm 0.4$

$[Cl^-]_{TJ} = 9.4 \pm 1.5$

$[NO_3^-]_{TJ} = 15.8 \pm 1.9$

$[SO_4^{2-}]_{TJ} = 39.7 \pm 6.6$

[Temperature Range$_{TJ}$ = 271.1 K

RH_{TJ} = 50%

$[NO_3^-]_{SH} = 8.10 \pm 7.78$ µg/m³

$[SO_4^{2-}]_{SH} = 12.00 \pm 7.35$ µg/m³

$[NH_4^+]_{SH} = 6.15 \pm 5.44$ µg/m³

$[Mg^+]_{SH} = 0.15 \pm 0.07$ µg/m³

$[Ca^+]_{SH} = 1.15 \pm 0.78$ µg/m³

Temperature Range$_{SH}$ = 289K

RH_{SH} = 75%

$[F^-]_{HZ} = 0.1 \pm 0.1$ µg/m³

$[Cl^-]_{HZ} = 4.3 \pm 1.9$ µg/m³

$[NO_3^-]_{HZ} = 12.6 \pm 5.4$ µg/m³

$[NO_3^-]_{TJ} = 0$ µg/m³

$[WATER]_{SH} = 22.83$ µg/m³

$[NO_3^-]_{SH} = 7.97$ µg/m³

$[WATER]_{HZ} = 45.65$ µg/m³

$[NO_3^-]_{HZ} = 12.40$ µg/m³

$[WATER]_{NJ} = 30.09$ µg/m³

$[NO_3^-]_{NJ} = 8.12$ µg/m³

Airborne [MPs]/[WATER]_BJ = 0.37µg/2.7 µg = 4.93×10⁻³ µg/µg

Airborne [MPs]/[WATER]_SH = 0.37µg/2.7 µg = 4.93×10⁻³ µg/µg

Airborne [MPs]/[WATER]_NJ = 0.37µg/2.7 µg = 4.93×10⁻³ µg/µg

$[SO_4{}^{2-}]_{HZ}$ = 18.1 ± 7.1 µg/m^3

$[Na^+]_{HZ}$ = 1.9 ± 0.7 µg/m^3

$[NH_4{}^+]_{HZ}$ = 7.6 ± 3.7 µg/m^3

$[K^+]_{HZ}$ = 0.8 ± 0.6 µg/m^3

$[Mg^{2+}]_{HZ}$ = 0.2 ± 0.1 µg/m^3

$[Ca^{2+}]_{HZ}$ = 1.5 ± 0.7 µg/m^3

Temperature Range$_{HZ}$ = 290K

RH$_{HZ}$ = 75%

$[NO_2{}^-]_{NJ}$ =0.50 ± 0.10 µg/m^3

$[F^-]_{NJ}$ =0.45 ± 0.05 µg/m^3

$[NO_3{}^-]_{NJ}$ =8.25 ± 3.75 µg/m^3

$[Cl^-]_{NJ}$ =1.75 ± 0.75 µg/m^3

$[SO_4{}^{2-}]_{NJ}$ =19.00 ± 2.00 µg/m^3

$[NH_4{}^+]_{NJ}$ =8.00 ± 1.00 µg/m^3

$[Ca^{2+}]_{NJ}$ =3.50 ± 0.50 µg/m^3

$[Na^+]_{NJ}$ =1.90 ± 0.10 µg/m^3

$[K^+]_{NJ}$ =1.15 ± 0.35 µg/m^3

Temperature Range$_{NJ}$ = 289K

RH$_{NJ}$ = 74%

France	$NH_4{}^+$=1.42 ± 0.32 µg/m^3 $NO_3{}^-$=2.60 ± 0.77 µg/m^3 $SO_4{}^{2-}$=1.78 ± 0.39 µg/m^3 Temperature = ~282 K RH = ~78%	[WATER] = 6.46 µg/m^3 $[NO_3{}^-]$ = 2.56 µg/m^3	$NO_3{}^-$(M) = 6.39 Airborne [MPs]/[WATER] = 0.42µg/30.01 µg $^=$ 4.93×10^{-3} µg/µg
India	F^-=0.27 ± 0.04 Cl^-=3.25 ± 0.21 $NO_3{}^-$=1.85 ± 1.38 $SO_4{}^{2-}$=12.02 ± 2.31	[WATER] = 12.69 µg/m^3 $[NO_3{}^-]$ = 1.82 µg/m^3	$NO_3{}^-$(M) = 2.31 Airborne [MPs]/[WATER] = 0.3µg/6.46 µg $^=$ 4.93×10^{-3} µg/µg

Na^+=0.98 ± 0.22

NH_4^+=2.58 ± 1.32

K^+=2.79 ± 1.08

Ca^{2+}=1.67 ± 0.41

Temperature = 298 K

RH = ~69%

Supplementary Figures:
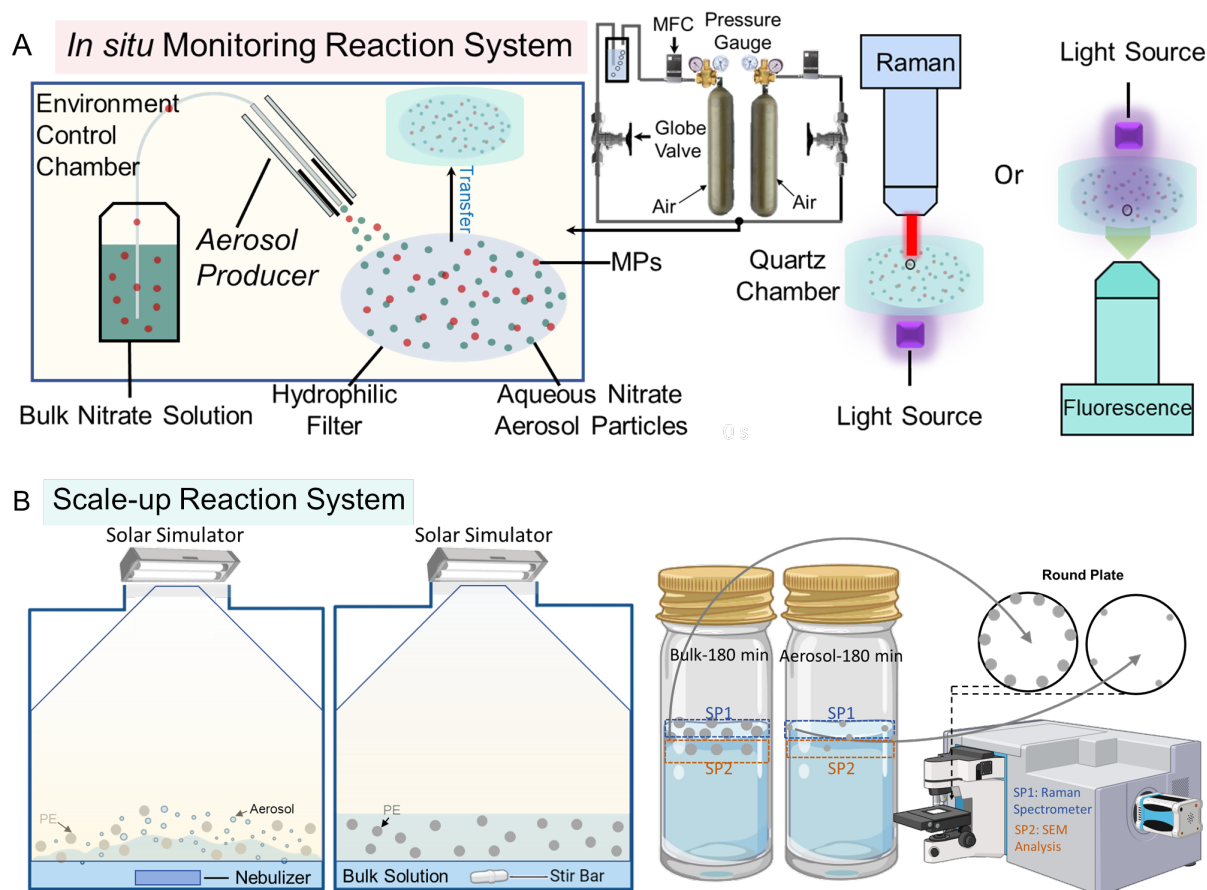
Supplementary Figure 1 | Schematic illustration of experimental setup.

(**A**) Schematic for a suite of gas flow control systems, *in situ* confocal Raman and confocal fluorescence imaging devices coupled with a cell chamber and LED UV light source (295 nm) that provides the capacity to probe the fate of MPs in real-time. (**B**) Schematic representation of the two scaled-up photochemical reaction systems: (i) bulk nitrate solution environment in a beaker with magnetic stirring expoosed to simulated sunlight irradiation, and (ii) aerosols generated by a nebulizer with simulated sunlight irradiation. Both reactor systems are fully sealed to minimize potential water loss.
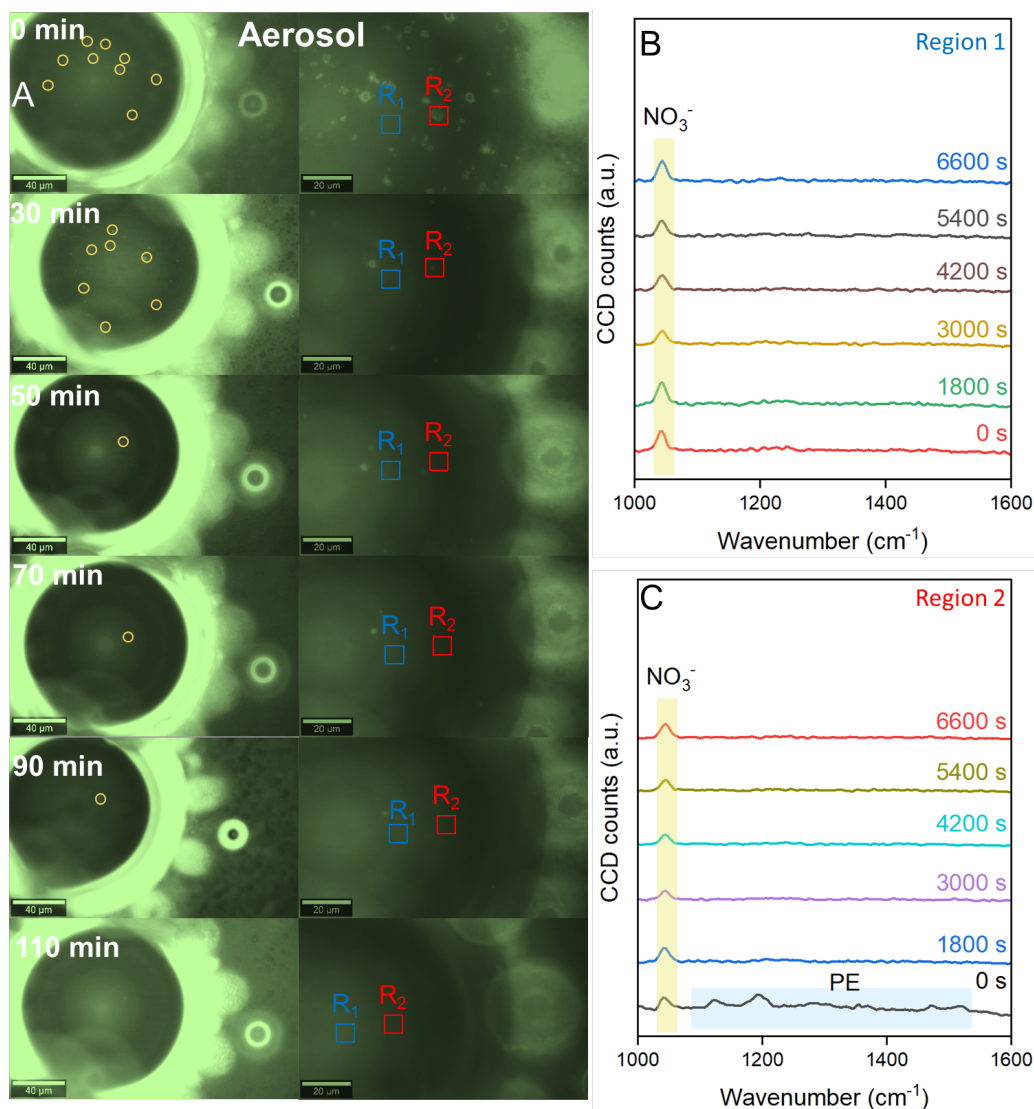
Supplementary Figure 2 | Raman spectroscopic analysis of the photochemical aging of polyethylene (PE) microplastics in NaNO$_3$ aerosols.

(**A**) Optical micrographs of PE microplastics suspended at the air-liquid interface of the NaNO$_3$ aerosols for different aging times (0, 30, 50, 70, 90, and 110 minutes). The red and blue squares indicate regions of interest (ROI) for Raman spectroscopic measurements that reflect the NaNO$_3$ aerosol (**B**) and PE microplastics (**C**) Raman spectra collected from the two ROIs (Region 1: NaNO$_3$ aerosol; Region 2: PE microplastics) at various aging times (0, 1800, 3000, 4200, 5400, and 6600 seconds).
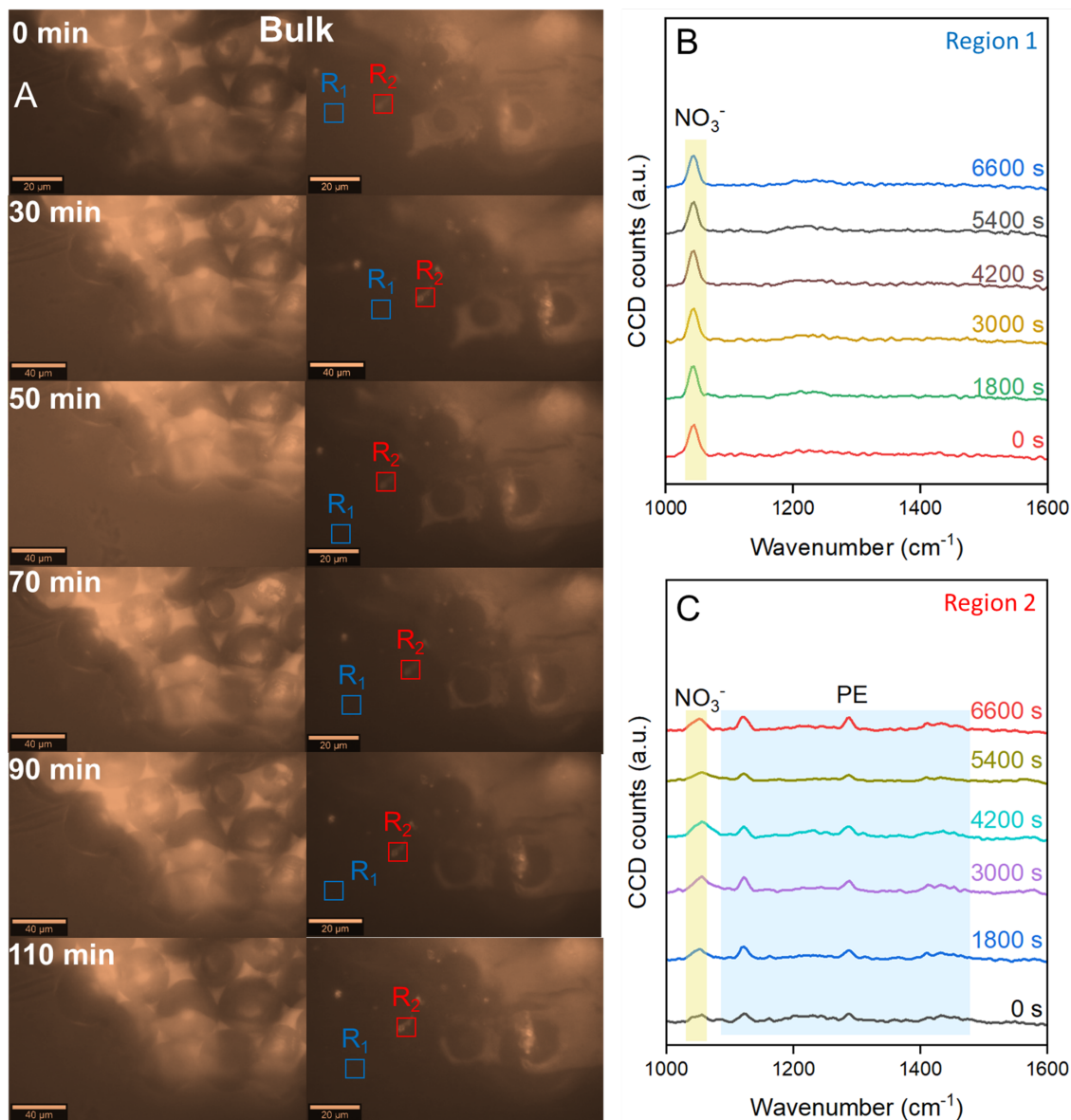
Supplementary Figure 3 | Raman spectroscopic analysis of the photochemical aging of polyethylene (PE) microplastics in bulk $NaNO_3$ solution.

(**A**) Optical micrographs of PE microplastics in bulk $NaNO_3$ solution at different aging times (0, 30, 50, 70, 90, and 110 minutes). The red and blue squares indicate regions of interest (ROIs) for Raman spectroscopic measurements, representing bulk $NaNO_3$ solution (**B**) and PE microplastics, respectively (**C**). Raman spectra collected from the two ROIs (Region 1: bulk $NaNO_3$ solution; Region 2: PE microplastics) at various aging times (0, 1800, 3000, 4200, 5400, and 6600 seconds).
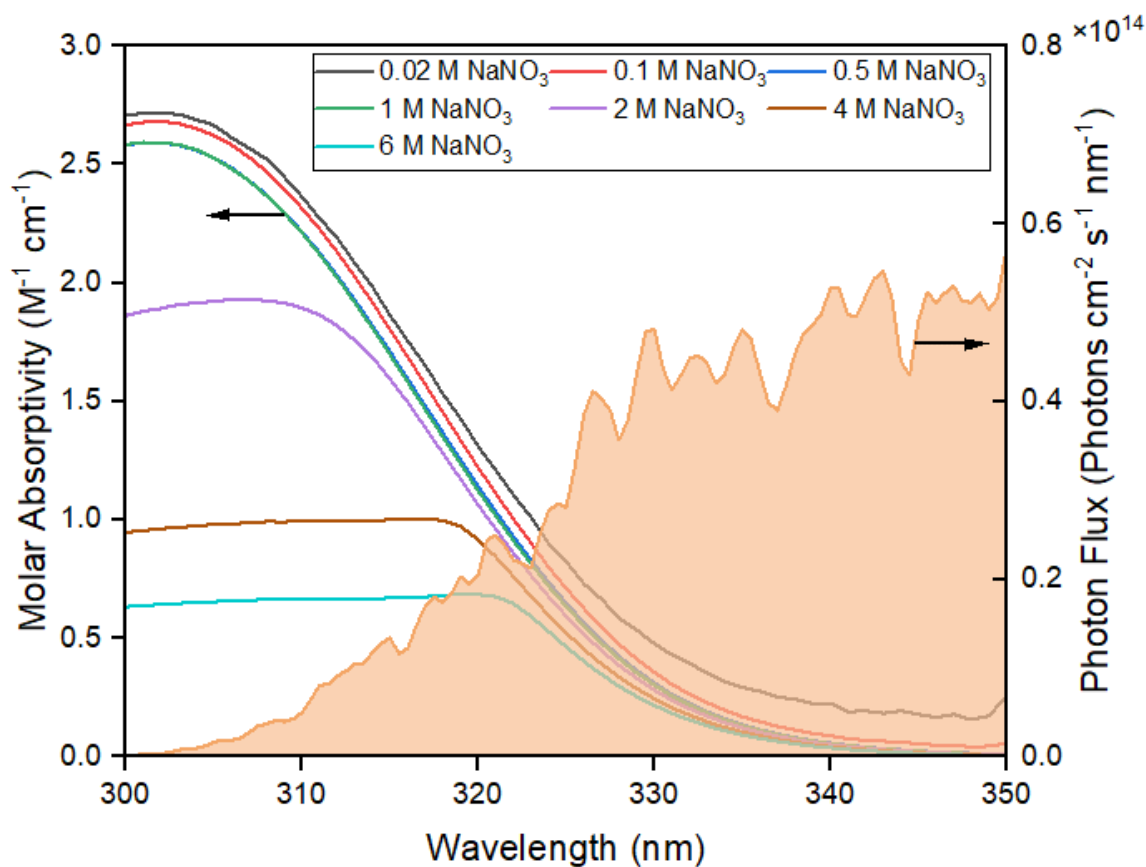
Supplementary Figure 4 | Molar absorptivity of NaNO$_3$ solutions (0.02–6 M) and photon-flux spectra of solar simulator.

Considering that the solar simulator's wavelength-dependent irradiance profile closely matches the ASTM G173-03 AM1.5G standard spectrum at 1 sun (1000 W m^{-2}), with their average measured irradiance output of 611 W m^{-2} (VBR-Solar Irradiance Meter, VABIRA), we scaled the ASTM G173-03 spectrum to 0.61 sun to generate the wavelength-dependent irradiance profile used for our solar simulator.
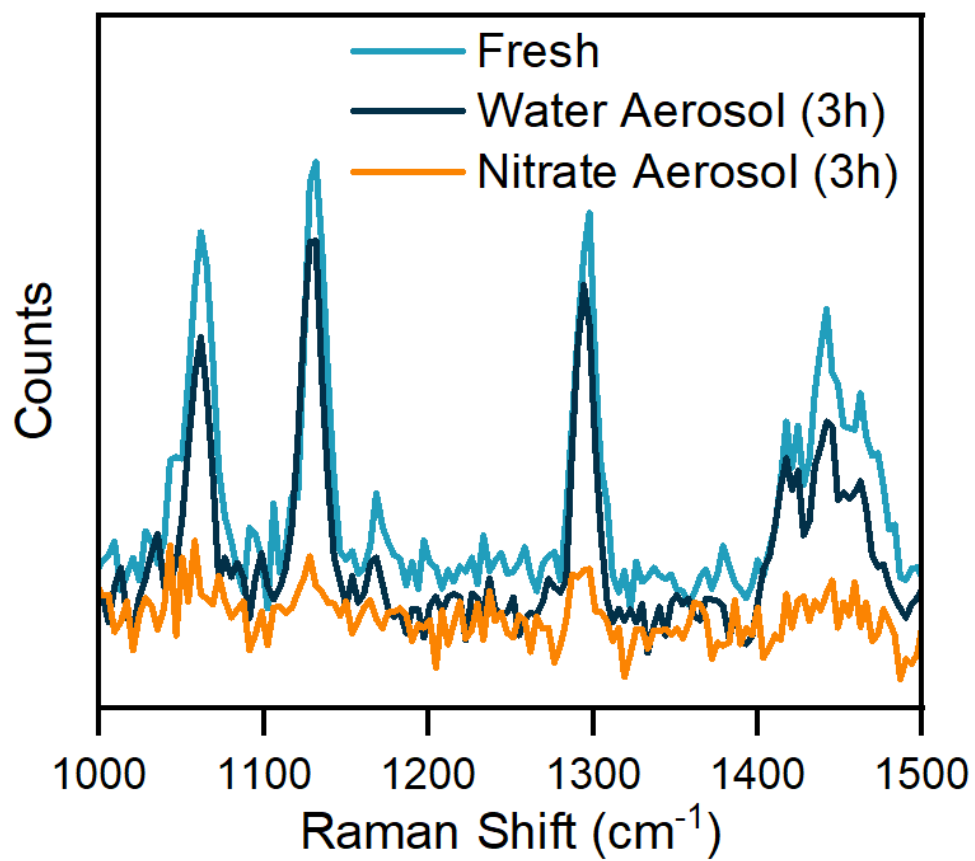
Supplementary Figure 5 | Raman spectra analysis of fresh MP and samples from the two photochemically aged suspensions (water aerosol and nitrate aerosol) after 180 minutes of exposure.
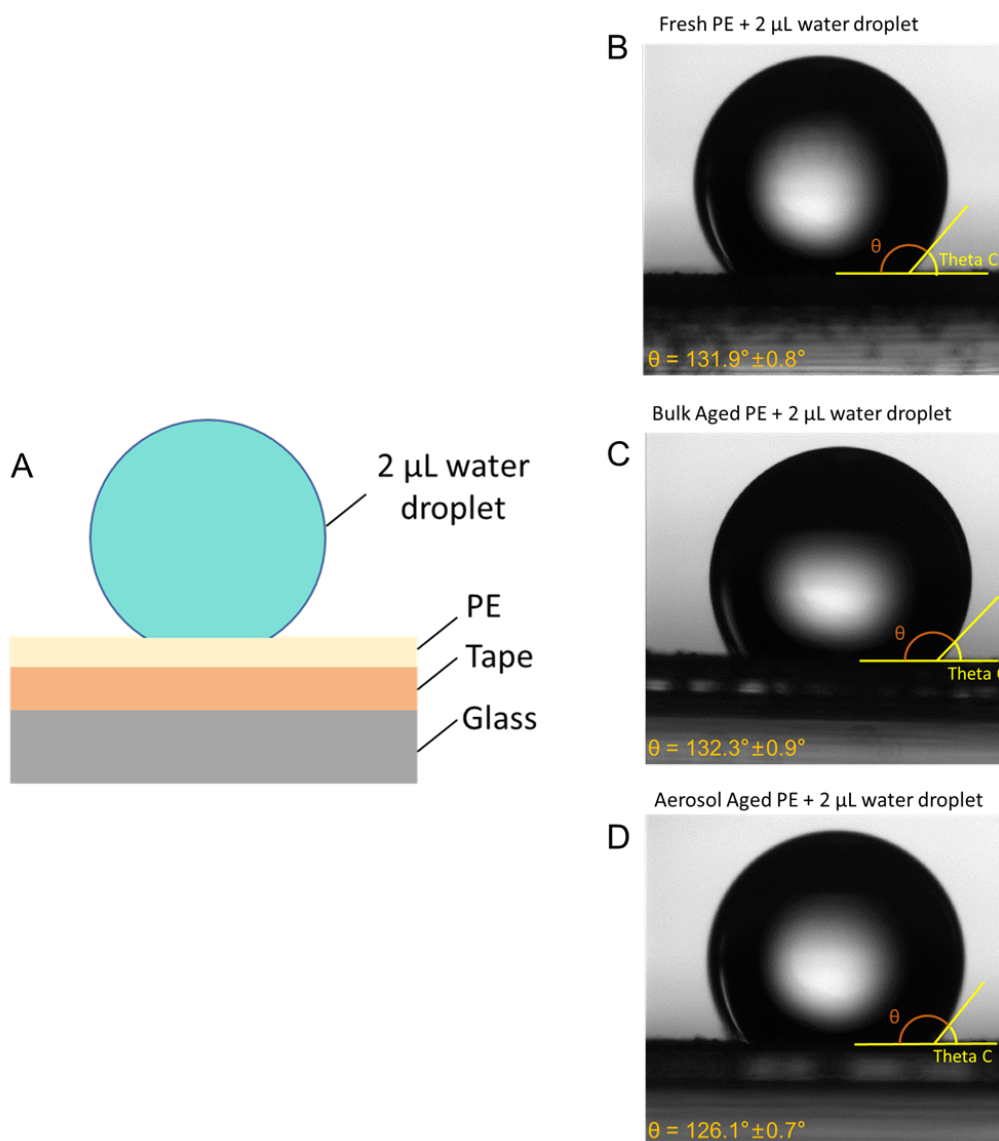
Supplementary Figure 6 | Contact angle measurements of water droplets on layered surfaces.

(**A**) schematic diagram illustrating a multilayer structure consisting of a top polyethylene (PE) layer (light yellow), tape layer (orange), and glass substrate (gray). Representative contact angle images showing θ = 131.9° ± 0.8°, 132.3° ± 0.9°, and 126.1° ± 0.7° on corresponding to fresh (**B**), bulk-aged (**C**), and aerosol-aged (**D**) PE layers. The yellow lines indicate the solid–liquid interface and the tangent at the contact point used to determine the contact angle (θ). Smaller θ values indicate greater surface hydrophilicity. Bulk-aged and fresh PE show comparable wettability, whereas aerosol-aged PE exhibits enhanced hydrophilicity.
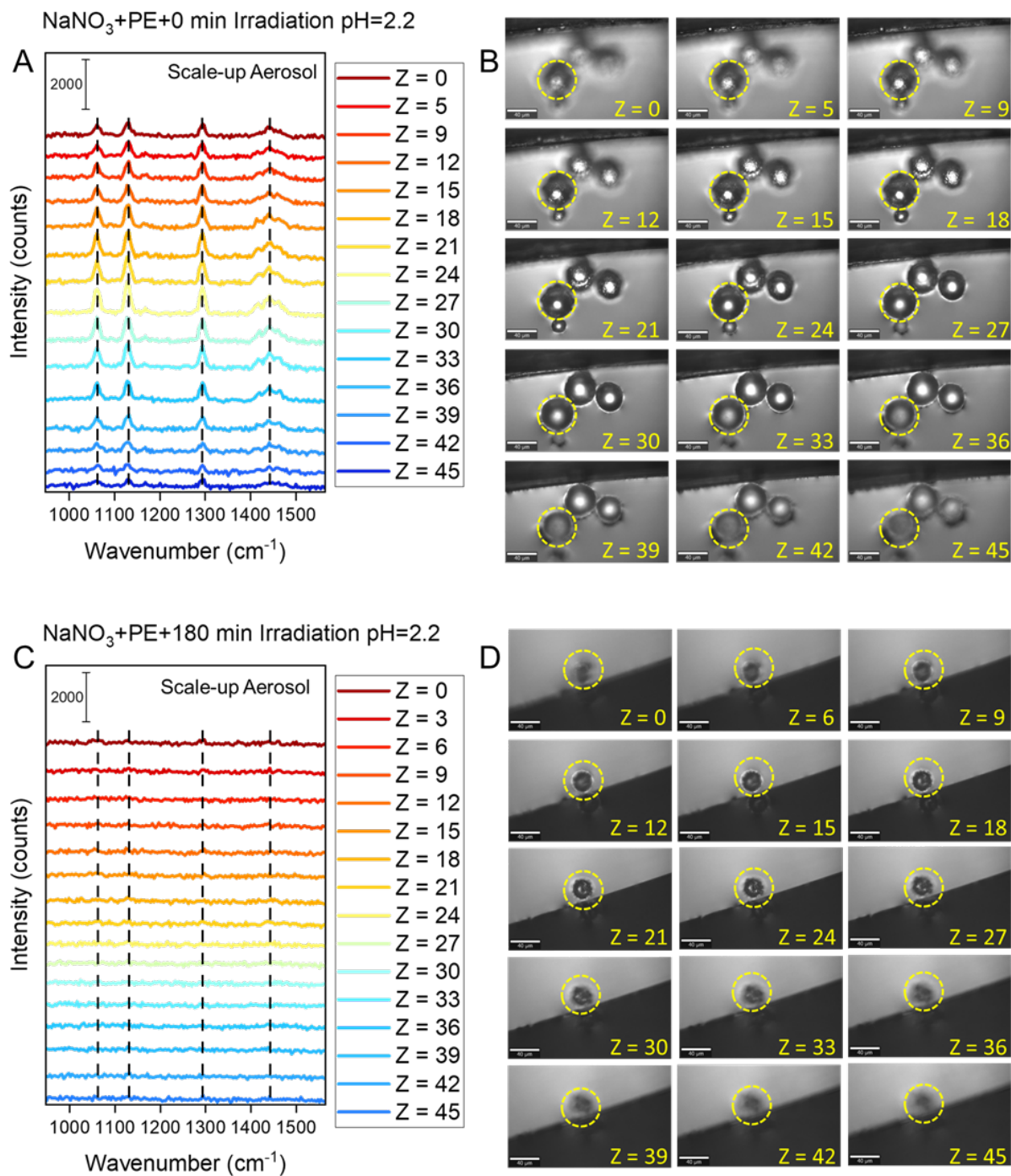
Supplementary Figure 7 | Depth-dependent Raman spectra.

Characterization of fresh (**A**) and aged (**C**) polyethylene (PE) microplastic microspheres in the presence of nitrate aerosol (pH = 2) upon irradiation for 3h, and corresponding optical images captured for fresh (**B**) and aged (**D**) PE microplastics, respectively.
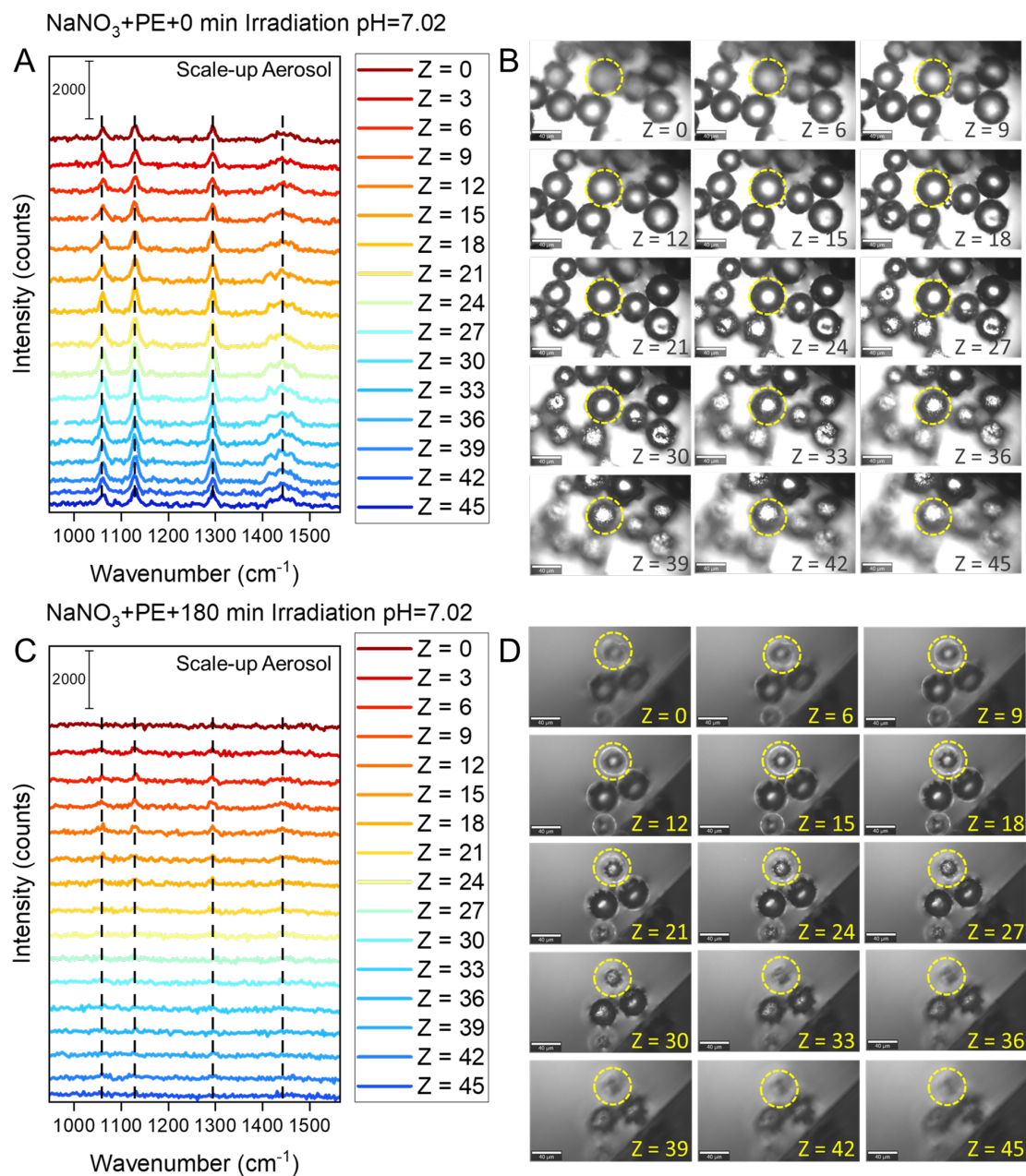
Supplementary Figure 8 | Depth-dependent Raman spectra.

Characterization of fresh (**A**) and aged (**C**) polyethylene (PE) microplastic microspheres in the presence of nitrate aerosol (pH = 7.02) upon irradiation for 3h, and corresponding optical images captured for fresh (**B**) and aged (**D**) PE microplastics, respectively.
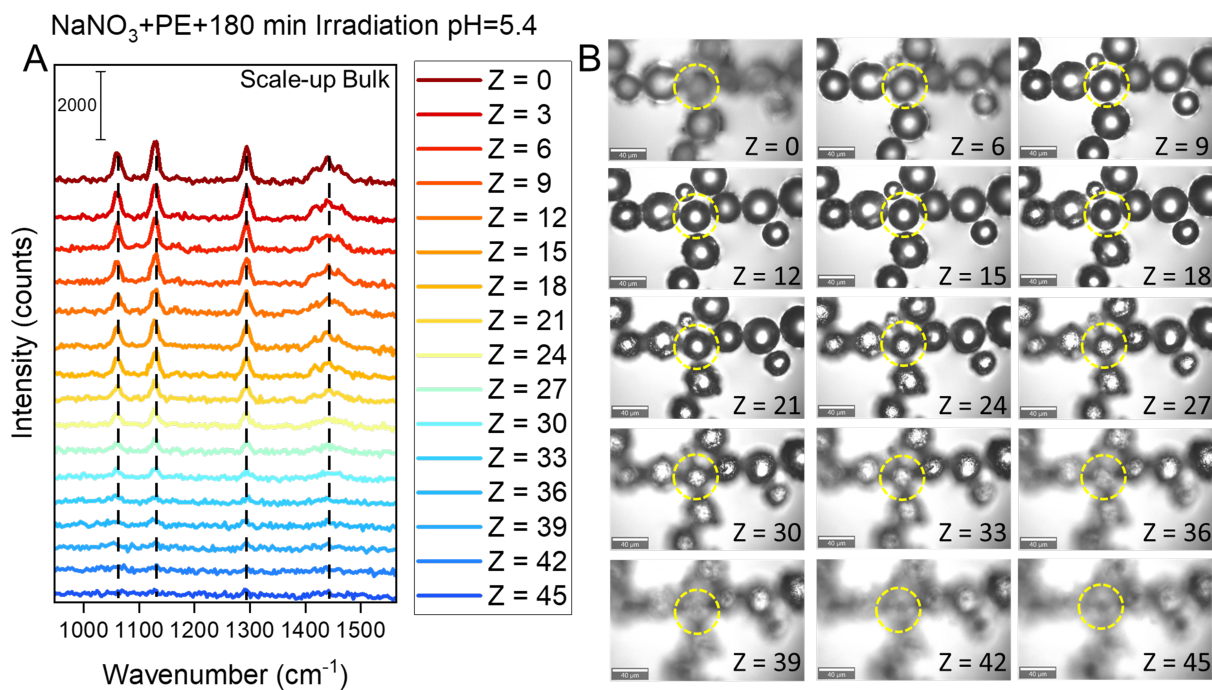
Supplementary Figure 9 | Depth-dependent Raman spectra.

Characterization of aged (PE) microplastic microspheres in the presence of bulk nitrate solution (pH = 5.4) upon irradiation for 3h, and corresponding optical images captured for (**B**) PE microplastics, respectively.
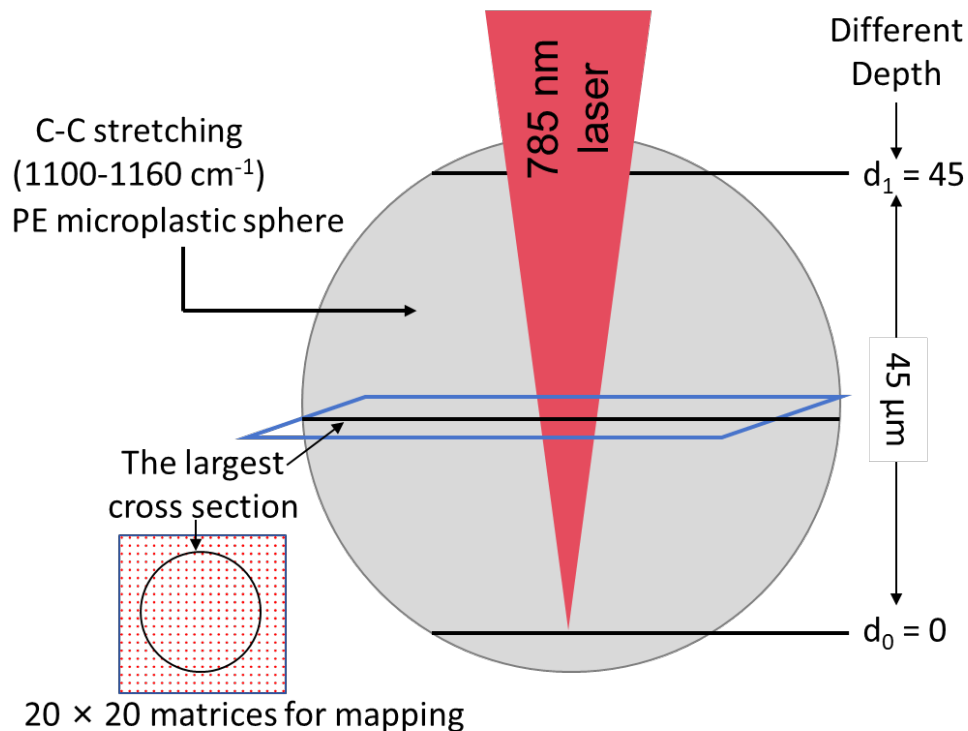
Supplementary Figure 10 | Schematic illustration of the characterization of aged microplastics in different depths:

From $d_0 = 0$ μm to $d_1 = 45$ μm, covering most of the selected PE microplastic spheres with their size of ~ 50 μm using a two-dimensional mapping approach, where Raman 2D mapping reconstructed images based on the integrated peak areas in the regions of 1100-1160 cm^{-1}.

Supplementary Figure 11 | Optical images (Z = 25) and mapping characterization of aged polyethylene (PE) microplastic microspheres:

Impacts of 3h photochemical aging of nitrate aerosol (**A**) and bulk nitrate (**B**) on signal intensity as a fucntion of depth.
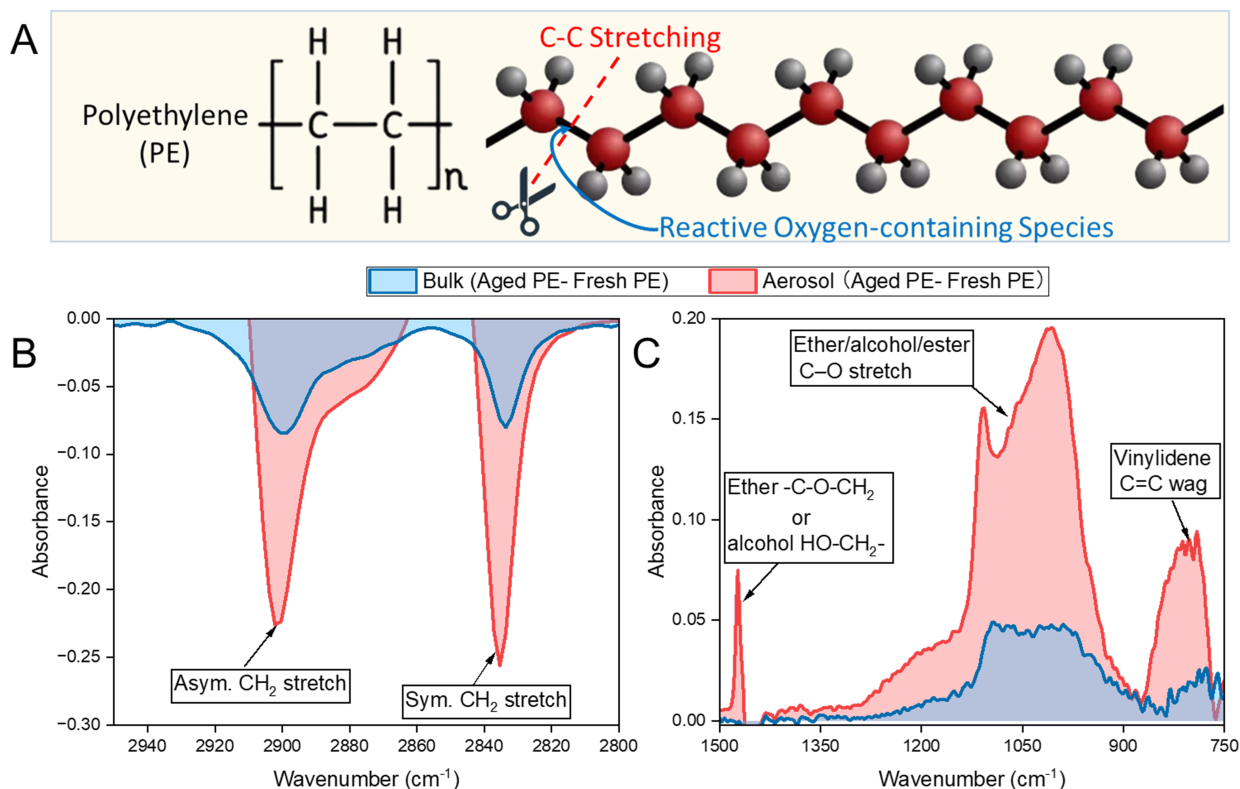
Supplementary Figure 12 | ATR-FTIR difference spectra of polyethylene (PE) particles after 180 min photochemical aging in the presence of nitrate.

(**A**) PE repeating unit and proposed ROS-driven oxidative degradation pathway, showing C–C bond scission (red) and incorporation of oxygenated functionalities (blue). (**B**) C–H stretch region (3100–2800 cm^{-1}). Difference spectra (aged – fresh) for PE particles irradiated in bulk-phase nitrate solution (blue) and as airborne aerosols (red), illustrating the loss of CH$_2$ antisymmetric (~2920 cm^{-1}) and symmetric (~2850 cm^{-1}) stretches. (**C**) Fingerprint region (1800–600 cm^{-1}): difference spectra for the same samples, highlighting newly formed carbonyl (~1720 cm^{-1}), ether/C–O (~1060 cm^{-1}), and other oxidation-related bands.
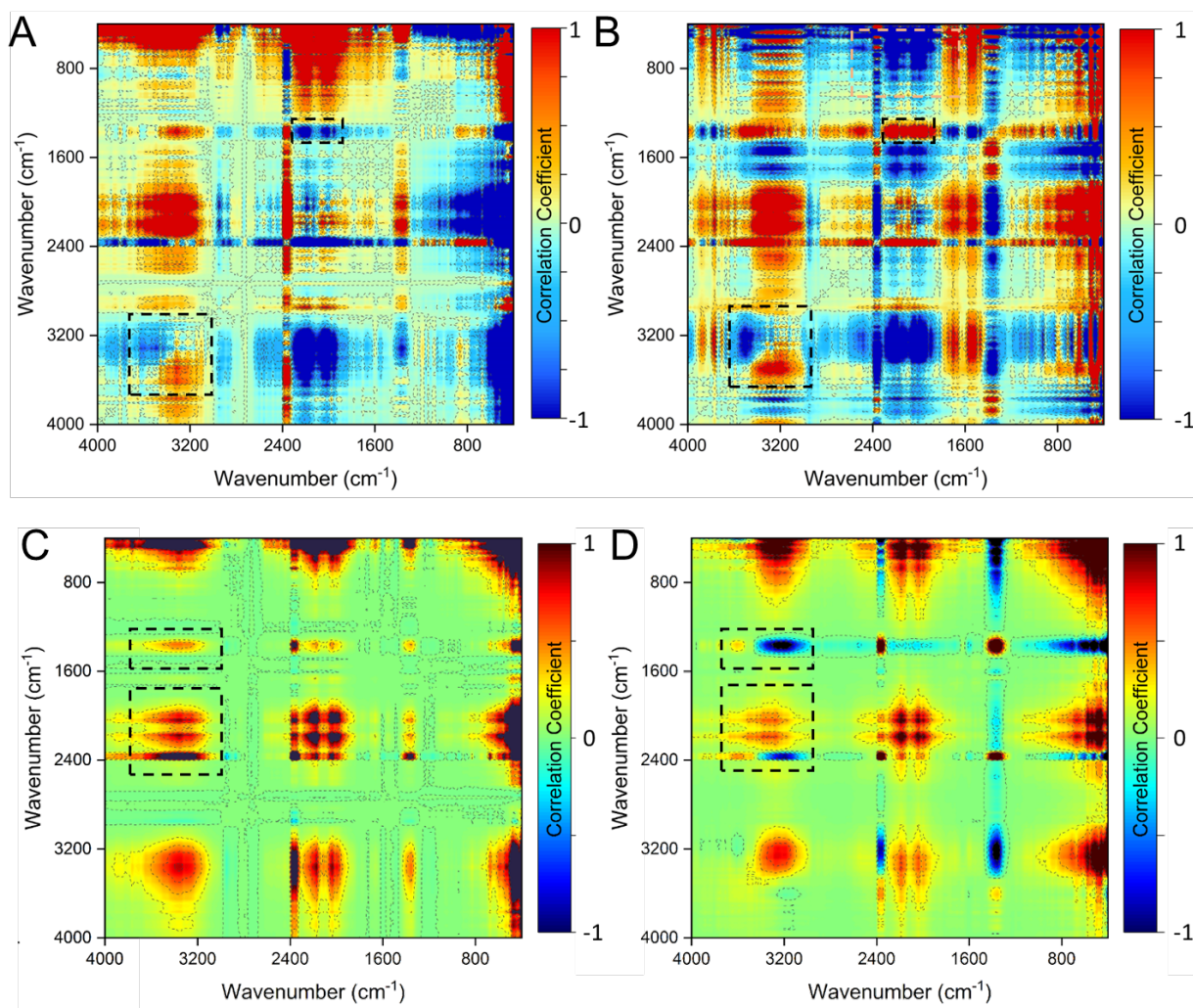
Supplementary Figure 13 | 2D correlation maps constructed from time-dependent FTIR spectra of filtrates of PE plastics aged in bulk $NaNO_3$ solution and in $NaNO_3$ aerosols.

The normalized synchronous (**A** and **B**) and asynchronous (**C** and **D**) 2D correlation spectra after irradiation for 0, 30, 60, 90, 120, 150, and 180 minutes based on measured ATR spectra.
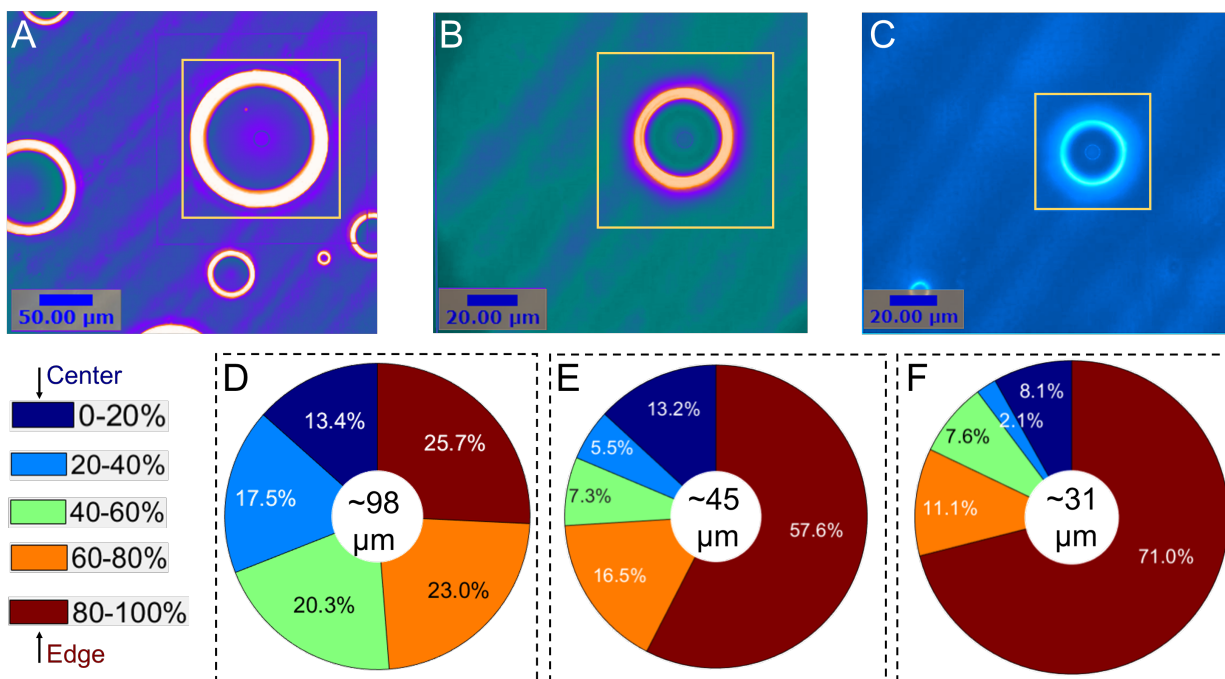
Supplementary Figure 14 | 2D mapping analysis of solutes within NaNO$_3$ aerosols.

Optical images of NaNO$_3$ aerosols of various sizes (**A**-**C**), with diameters of ~98, ~45, and ~31 μm, respectively. The pie charts quantifying NO$_3^-$ content distribution in five concentric segments, each representing 20% of the aerosol sphere volume from edge to center (**D-F**). The color gradient from blue (low) to red (high) represents a growing percentage of nitrate within aerosol particles from the edge region to the interface region. Pie charts quantify the percentage of NO$_3^-$ within five concentric segments (Supplementary Fig. 14D-F), each representing 20% of the aerosol volume from the center to the edge. In the largest microdroplet (~100 μm), nitrate is more evenly distributed across segments. In smaller microdroplets (~45 μm and ~31 μm), nitrate enrichment is increasingly localized at the outermost segments, accounting for 58% and 71% of the solute content, respectively. This size-dependent trend underscores the role of aerosol size in concentrating solutes near the interface.
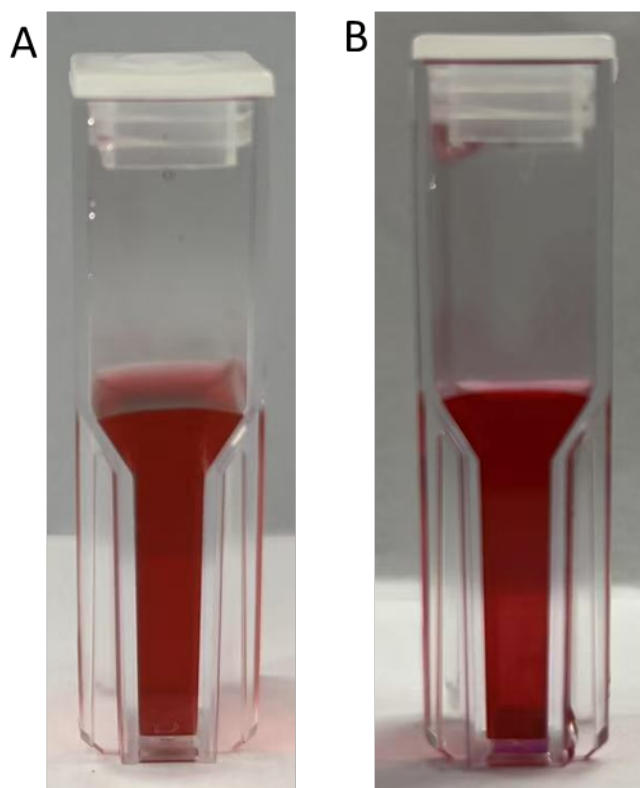
Supplementary Figure 15 | Stability of AuSCN + mPEG nanoprobes in the presence of 1.5 M of nitrate ions.

(**A**) 0 h and (**B**) 20 h. Following surface functionalization with mPEG, no agglomeration of gold nanoparticles was observed after 20 h in the presence of high concentrations of nitrate.
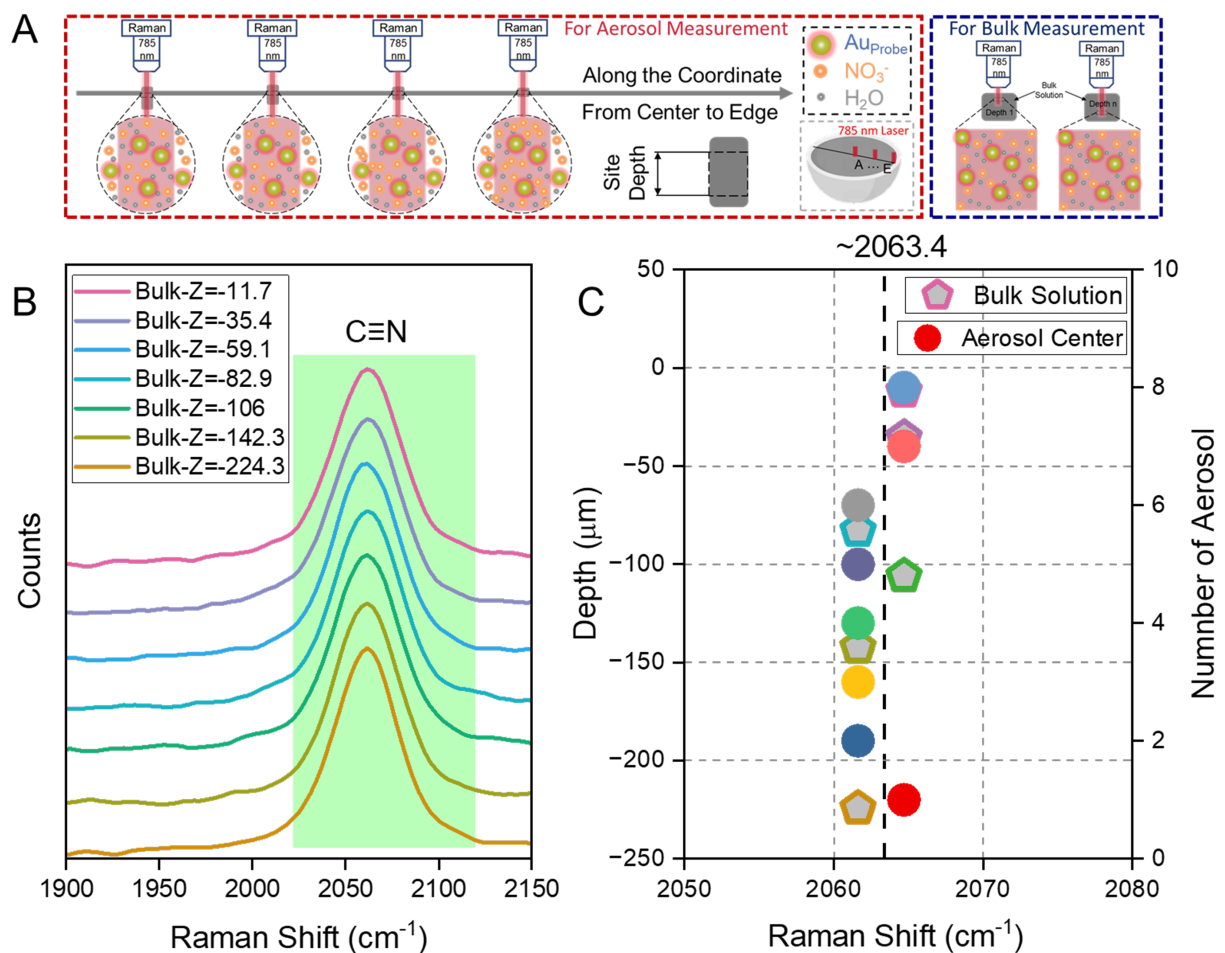
Supplementary Figure 16 | Raman-based assessment of electric field distribution in both bulk nitrate solution at different depths and in the interior (center) region of nitrate aerosols.

(**A**) Diagram illustrating measurement workflows for determining the strength of the electric field in the aerosol and bulk phase of aqueous nitrate, respectively. Raman spectra collected for bulk nitrate solution at different depths (**B**), and corresponding Raman shifts determined for the bulk solution and the interior bulk region of aerosol particles (**C**).
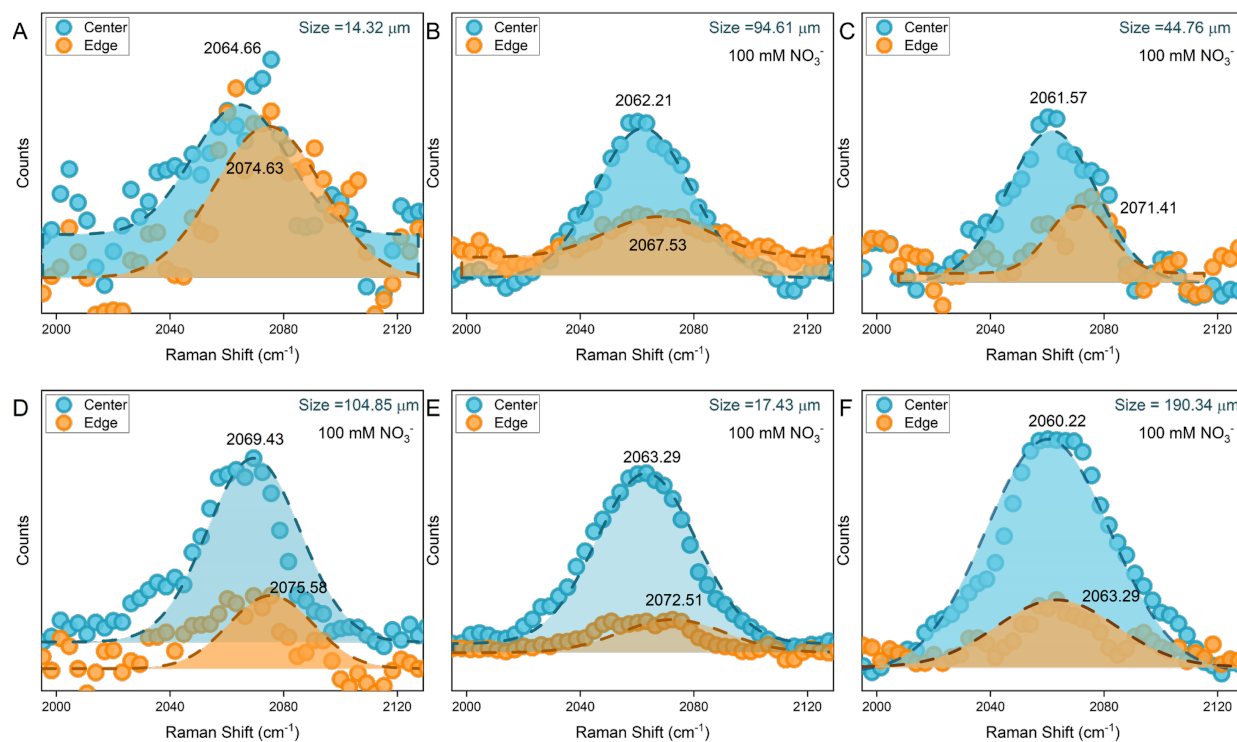
Supplementary Figure 17 | The Raman spectra of the C≡N feature at the edge and center regions of 0.1 M nitrate aerosol particles.

Radii of **A** (14.32 μm), **B** (94.61 μm), **C** (44.76 μm), **D** (104.85 μm), **E** (17.43 μm), and **F**(190.34 μm).
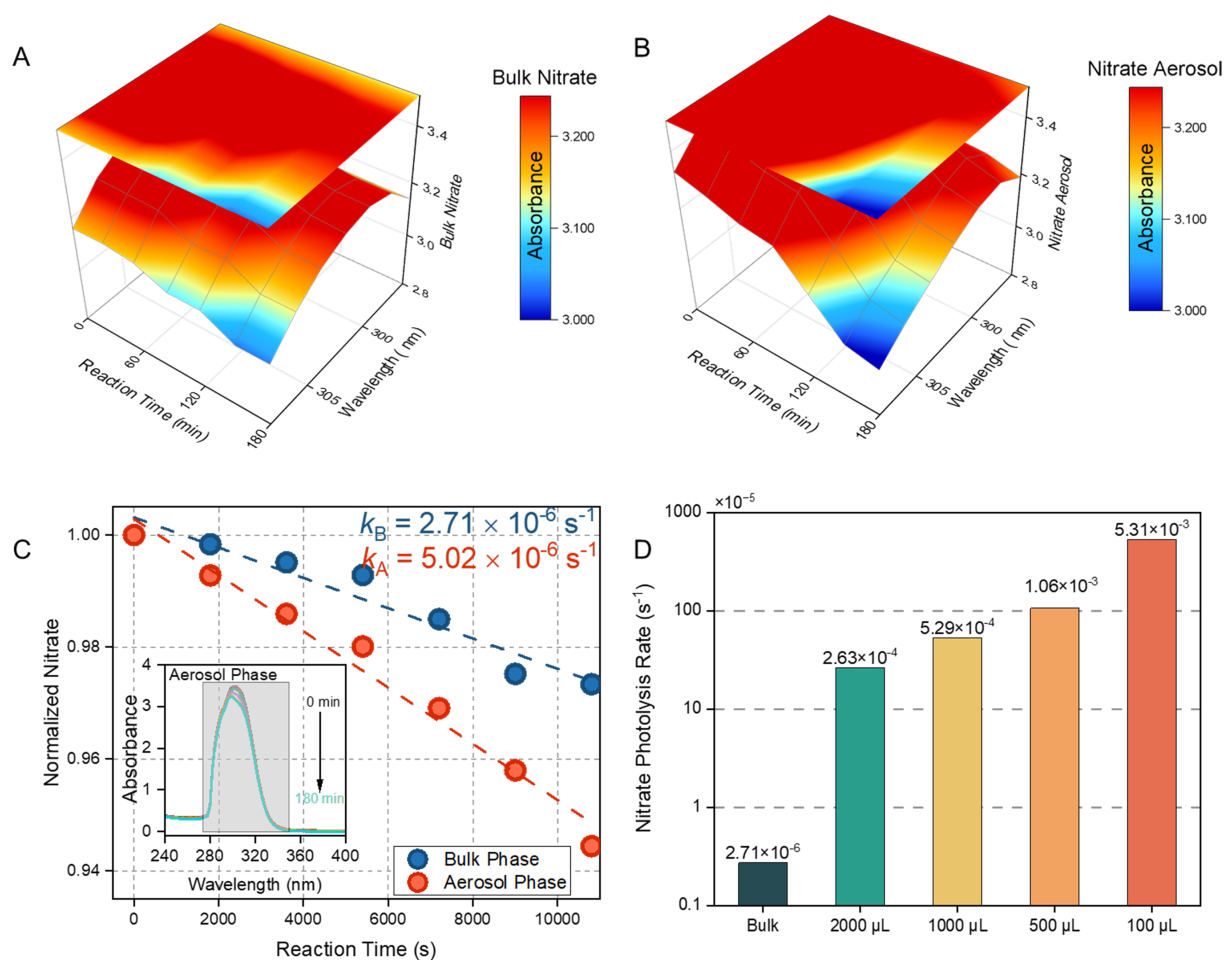
Supplementary Figure 18 | Enhanced photolysis kinetics of nitrate in aerosol versus bulk phase.

The contour maps of UV-vis absorption spectra of nitrate upon irradiation in the bulk (**A**) and aerosol cases (**B**). (**C**) The decay rates of UV-vis light absorption of nitrate in the bulk and aerosol phases. Note: the rates determined in the panel are based on the integrated area of nitrate light absorption in the wavelength range of 270-350 nm. Nitrate concentration = 1 M. For the aerosol phase (inset), the integrated absorbance at each time was normalized to the value at 0 min, yielding a decay profile that reflects the photolysis kinetics. The same procedure was applied to the bulk phase spectra to generate their corresponding decay curves. (**D**) The predicted nitrate photolysis rates of nitrate aerosol particles upon irradiation assuming that the total volumes of nitrate aerosol are 2000, 1000, 500, and 100 μL, respectively. The calculation was detailed in the methodology section.
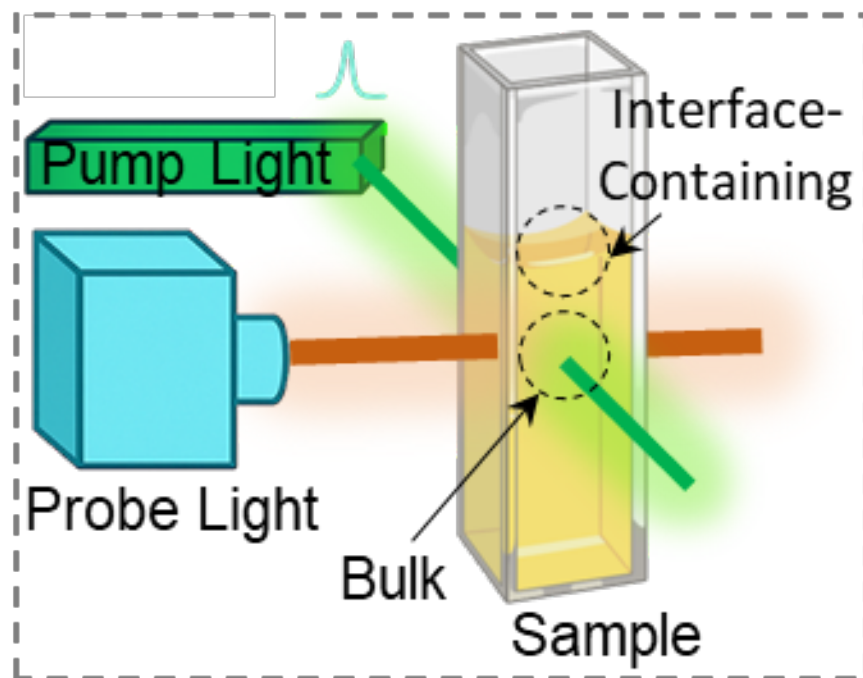
Supplementary Figure 19 | Schematic chart of NTAS analysis of intermediates produced from bulk or air/water interface of nitrate.
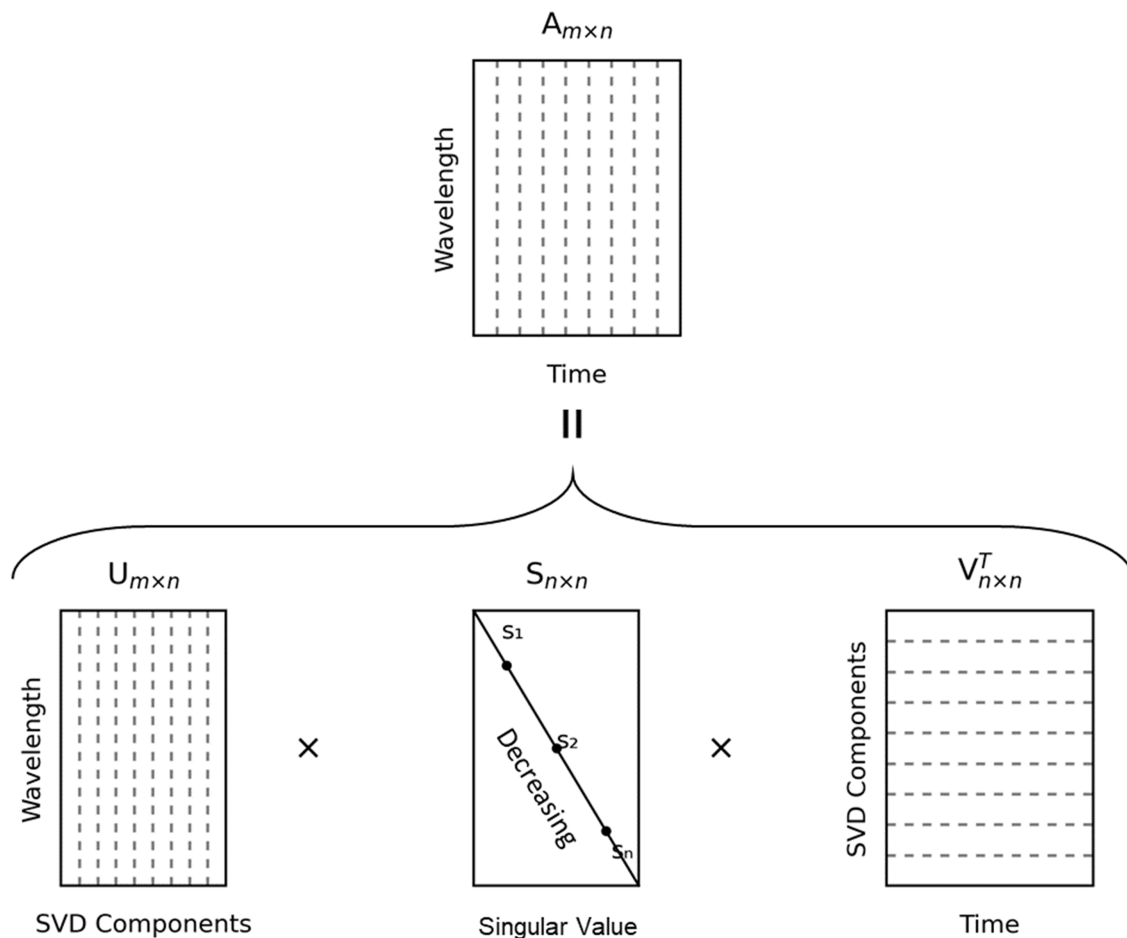
Supplementary Figure 20 | Schematic of Singular Value Decomposition (SVD).

The two-dimensional spectra measured in transient absorption experiments can be expressed in the form of a two-dimensional matrix A. Each column of matrix A is the absorption spectrum at different wavelengths λ for a fixed delayed moment, and each row of matrix A is the absorption (ΔOD) at a fixed wavelength as a function of time t. The matrix elements can be written as $A_{ij} = A(\lambda_i, t_j)$, where the number of wavelengths is m and the number of delay time points is n. This results in an m × n two-dimensional matrix A, which can be split into three matrices multiplied by the SVD[119]: $A = USV^T$, where the wavelength-dependent spectra of the SVD components are reflected in the columns of U. The diagonal element S_i of S is the wavelength-dependent spectrum of the ith SVD component, while the diagonal element S_i of S is the wavelength-dependent spectrum of the ith SVD component. The diagonal element S_i of S is the singular value of the ith SVD component, and SVD components with smaller singular values are generally regarded as random noise. Each column of V reflects the kinetic variation of the SVD component.
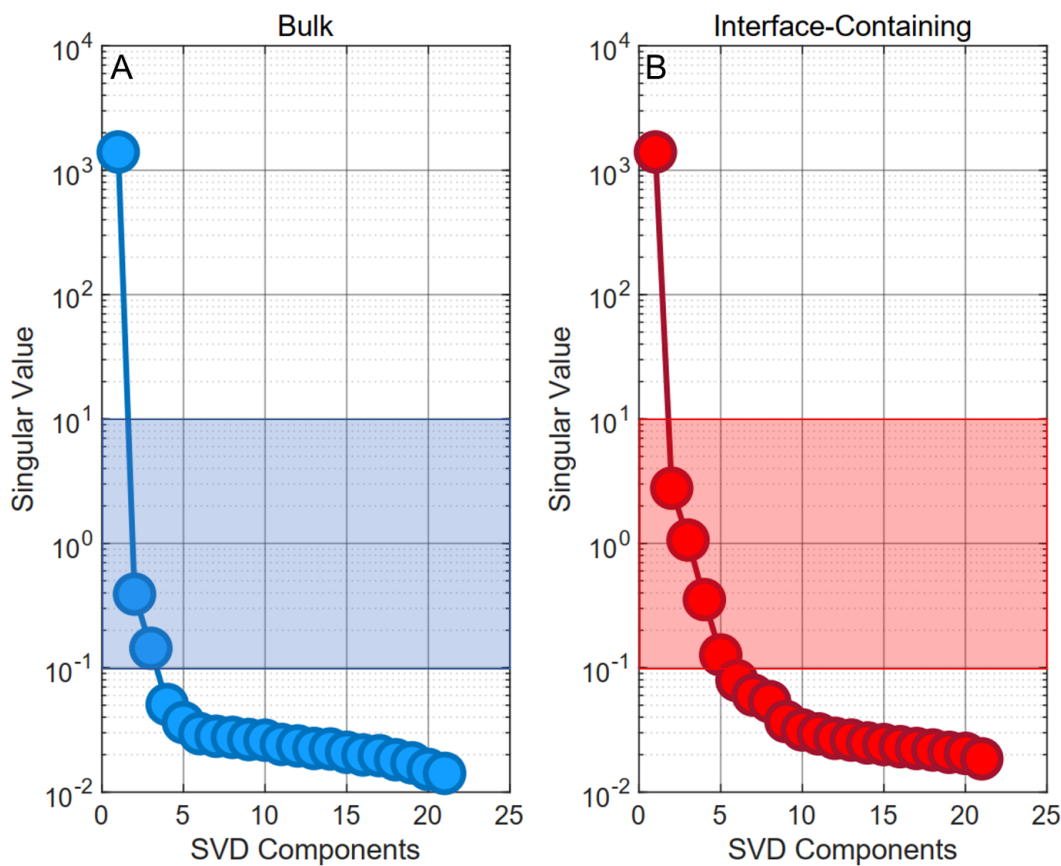
Supplementary Figure 21 | Singular value distributions from analysis of NTAS spectra.

For bulk (**A**) and interface-containing (**B**) nitrate solutions. For both systems, the singular values decrease sharply within the first few components, indicating that the majority of spectral variance is captured by a small number of dominant modes. However, the interface-containing system exhibits a slower decay in singular values compared to the bulk solution, suggesting the presence of additional, spectrally distinct processes at the air–water interface. The shaded areas denote the region where singular values are close to the noise floor, implying limited contribution to meaningful spectral features. This difference in the number and magnitude of significant components highlights the greater photochemical complexity in the interface-containing system relative to the bulk.
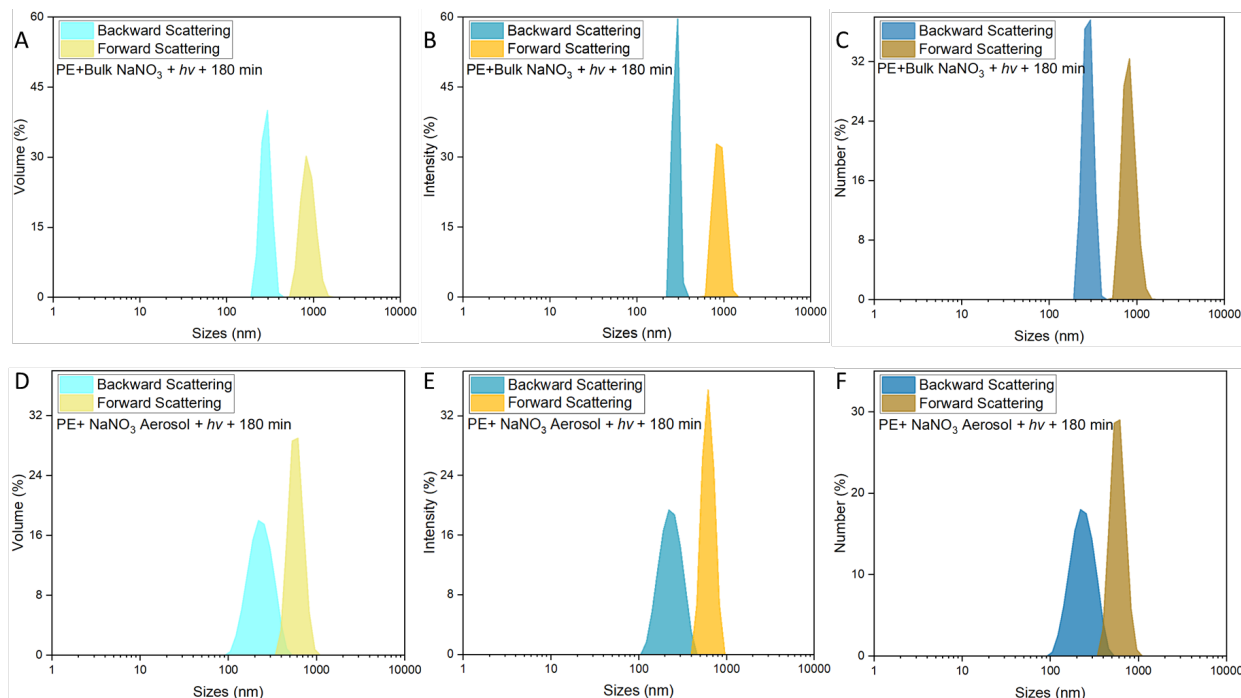
Supplementary Figure 22 | Dynamic light scattering (DLS) of polyethylene (PE) particles after 180 min of irradiation in the presence of NaNO$_3$ under different phase conditions.

(**A-C**) PE aged in bulk NaNO$_3$ solution under simulated sunlight. (**D-F**) PE aged in NaNO$_3$ aerosol phase under the same irradiation conditions. Size distributions were obtained using both backward scattering (173°) and forward scattering (13°) detection modes. The results demonstrate that bulk-phase aging yields predominantly smaller particles (<200 nm), while aerosol-phase aging produces a broader distribution with significant production of both larger and smaller particles. It is important to note that we do not observe distinct new peaks corresponding to very small particles (<10 nm). This is expected because the

scattering signal intensity scales strongly with particle size ($\alpha \propto d^6$ for Rayleigh scattering),

making very small particles difficult to detect with a sufficient signal-to-noise ratio. Instead, the broadening of the smaller peak can be interpreted as an indirect signature of partial fragmentation and nucleation of nanoscale debris. Furthermore, the concurrent peak broadening in both modes strengthens the conclusion that aerosol-mediated reactions increase the heterogeneity of the particle size distribution, rather than merely shifting the dominant mode.
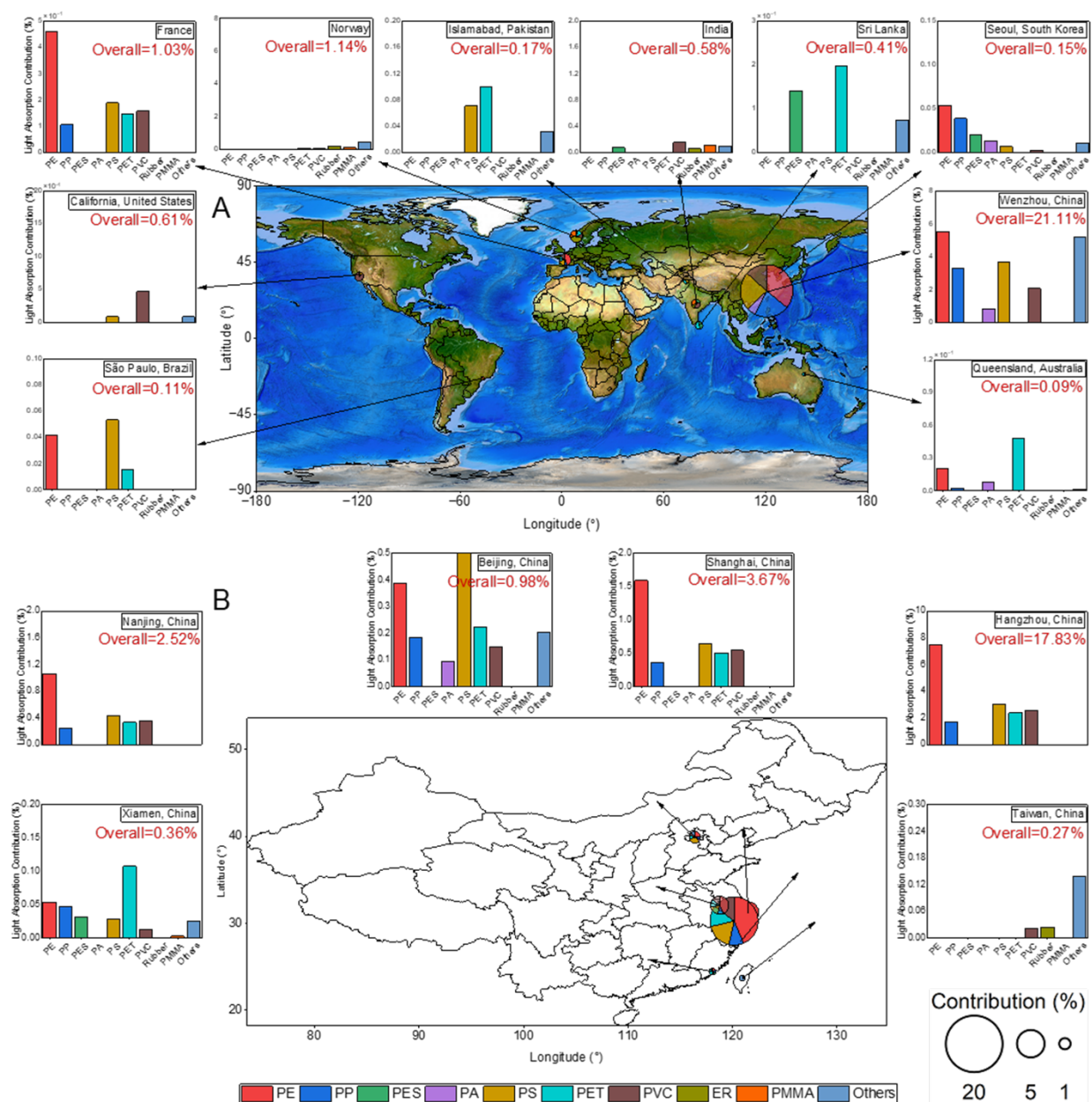
Supplementary Figure 23 | Distribution of microplastic types and their contribution to organic carbon absorptivity in 10 regions worldwide (A) and 7 cities in China (B). Condition: MPs equivalent aging time = 7 days.
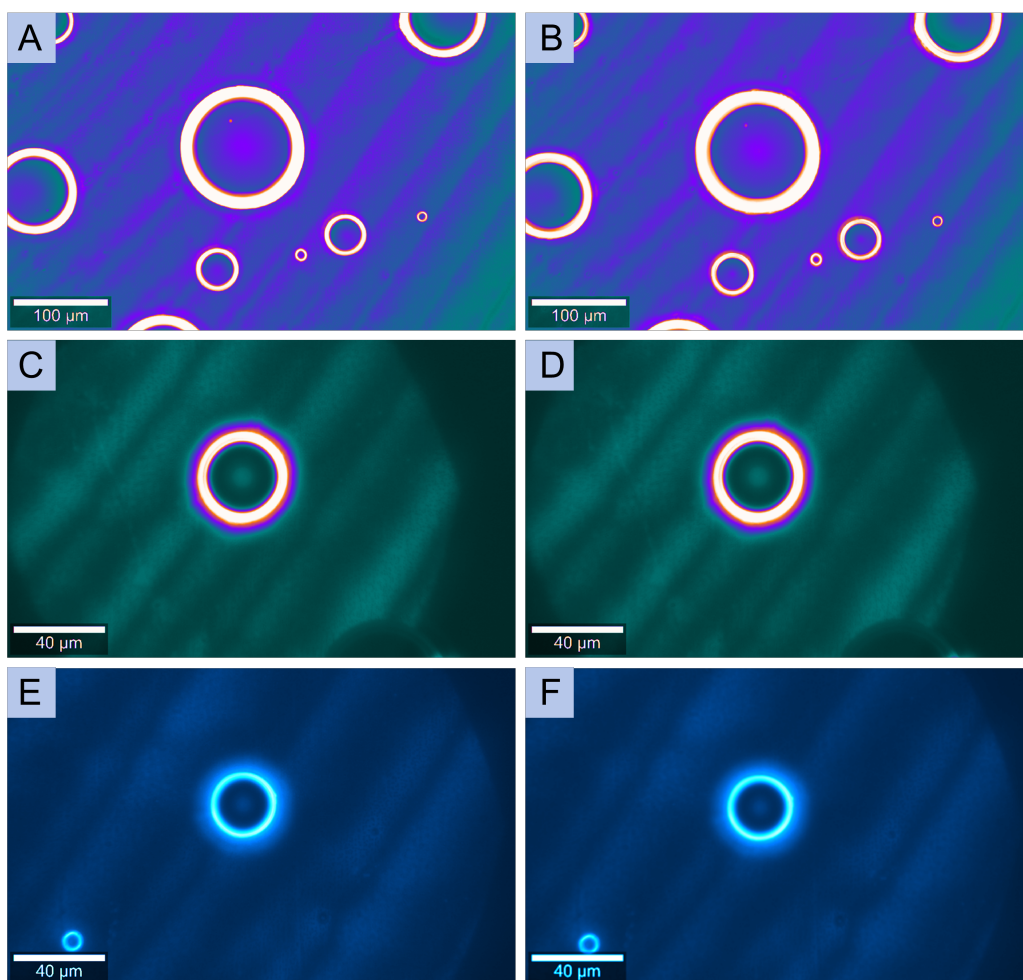
Supplementary Figure 24 | Stability of nitrate aerosol particles.

Optical image of nitrate aerosol particles before (**A**, **C**, **E**) and after mapping analysis (**B**, **D**, **F**).
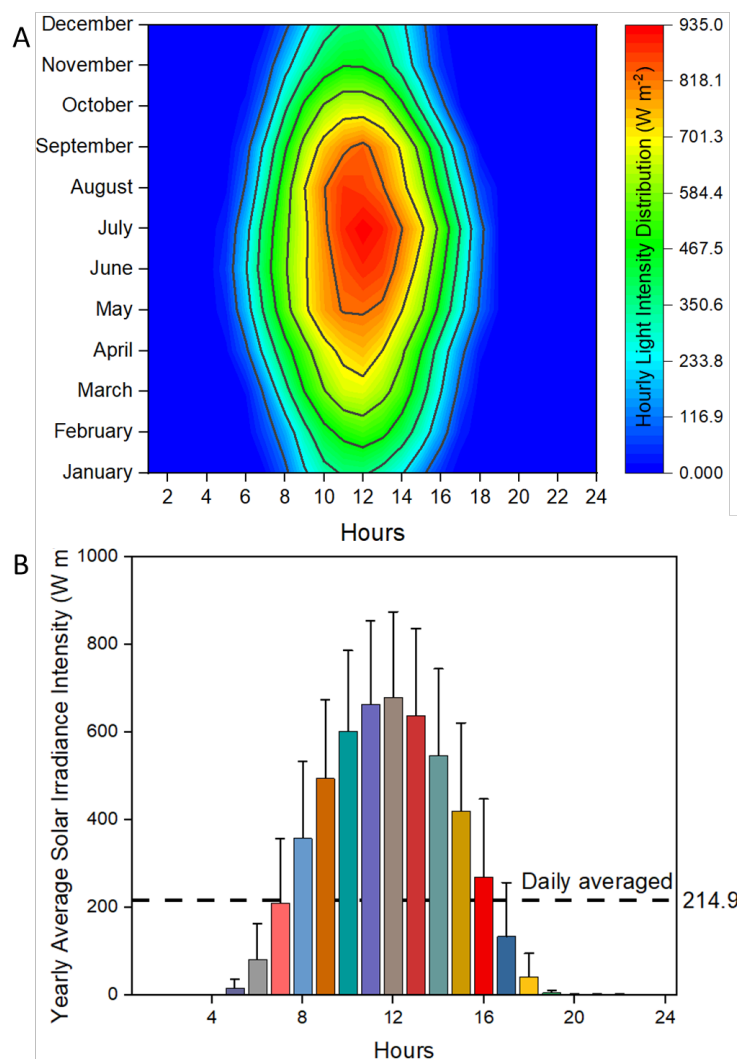
Supplementary Figure 25 | Solar irradiance and corresponding intensity.

(**A**) Contour plot of the hourly solar irradiance distribution (0–24 h) from January through December, where the color scale indicates irradiance intensity (W m^{-2}) ranging from approximately 0.0 (blue) to 935.0 (red). The highest intensities appear around midday during the summer months. (**B**) Bar chart of the yearly average solar irradiance intensity for each hour of the day, with error bars representing standard deviations. The daylight availability and luminous efficacy of global irradiance were taken from the literature[120]. The daily average irradiance corresponds to ~0.215 sun units, calibrated against the ASTM G173-03 AM1.5G standard spectrum.

$$y = A + B/(1 + 10^{(C - x)D})$$

A = 14.77
B = 51.23
C = 2.17
D = -0.27
R^2 = 0.99
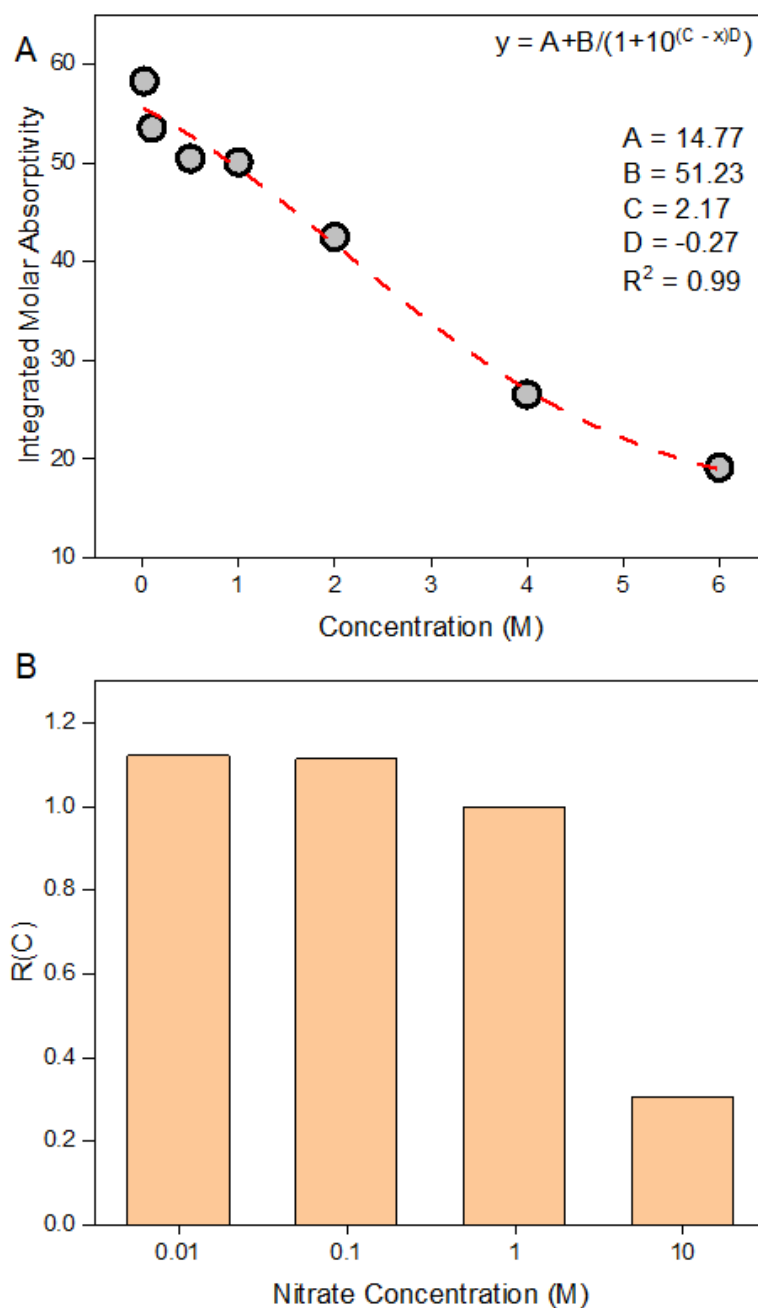
Supplementary Figure 26 | Molar absorptivity and predicted R(C) values.

(A) Integrated molar absorptivity (300-350 nm) of aqueous nitrate as a function of concentration (0.02–6 M). (B) Predicted R(C) values at four representative nitrate levels found in the atmospheric aerosol environment (0.01M, 0.1 M, 1 M, and 10 M).
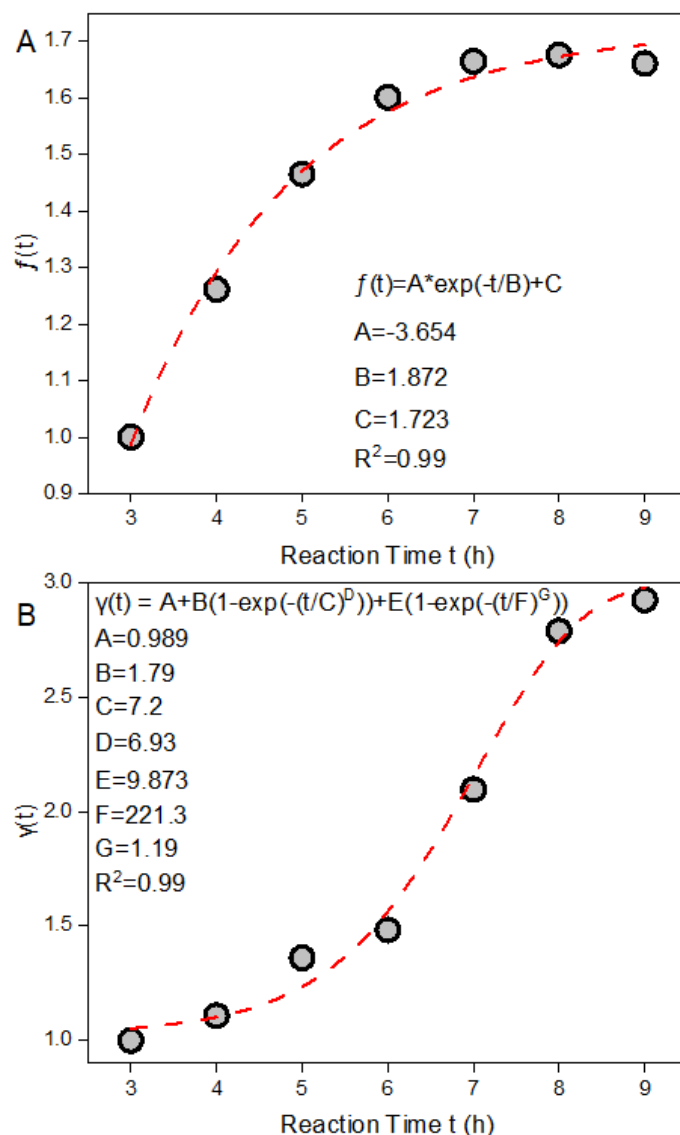
Supplementary Figure 27 | Empirical correction functions for equivalent laboratory exposure time.
(A) The correction function $f(t)$ (R^2 = 0.99) describing the variation of the organic carbon (OC) conversion fraction of microplastics as a function of equivalent laboratory exposure time (t_lab). This function is used to correct OC conversion with respect to the equivalent experimental time. (B) The correction function $\gamma(t)$ (R^2 = 0.99) describes the variation of the mass absorption cross-section (MAC) of microplastics as a function of t_lab during the photochemical aging process.
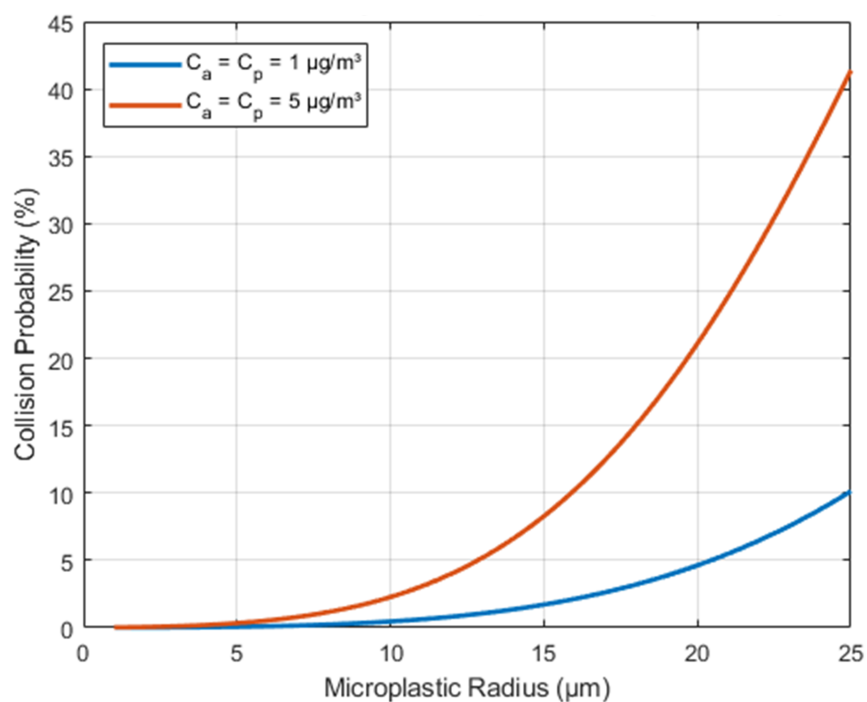
Supplementary Figure 28 | Modeled probability of collision between airborne microplastics and deliquescent nitrate aerosols over atmospheric timescales, based on multi-mechanism kernel integration (Brownian diffusion, turbulent shear, and gravitational settling).

All scenarios assume a fixed turbulent dissipation rate (ε = 1 m^2/s^3) and a nitrate aerosol radius of 1 μm. Microplastic radius ranges from 1 to 25 μm. Despite lower number densities, low concentration of aerosol leads to non-marginal probabilities of collision (>5%) for microplastics larger than 20 μm. This illustrates the potential for the aging process even under relatively clean background conditions when microplastics persist in the atmosphere. We here applied a conservative collision probability of 10% for all estimations in this work.

Supplementary Reference:

1   Smirnova, D. S. *Application of two-dimensional correlation analysis to explosives detection and polymer crystallization*, California Institute of Technology, (2010).

2   Mao, R. *et al.* Aging mechanism of microplastics with UV irradiation and its effects on the adsorption of heavy metals. *J. Hazard Mater.* **393**, 122515, doi:10.1016/j.jhazmat.2020.122515 (2020).

3   Pascher, T. F., Ončák, M., van der Linde, C. & Beyer, M. K. Infrared multiple photon dissociation spectroscopy of anionic copper formate clusters. *J. Chem. Phys.* **153**, 184301, doi:10.1063/5.0030034 (2020).

4   van der Veken, B. J. *et al.* The nature of improper, blue-shifting hydrogen bonding verified experimentally. *J. Am. Chem. Soc.* **123**, 12290-12293, doi:10.1021/ja010915t (2001).

5   Rahman, M. M., Al-Sulaimi, S. & Farooque, A. Characterization of new and fouled SWRO membranes by ATR/FTIR spectroscopy. *Appl. Water Sci.* **8**, 183, doi:10.1016/j.apsusc.2005.12.115 (2018).

6   Grause, G., Chien, M.-F. & Inoue, C. Changes during the weathering of polyolefins. *Polym. Degrad. Stabil.* **181**, 109364, doi:10.1016/j.polymdegradstab.2020.109364 (2020).

7   Konar, J. & Ghosh, R. Oxidative degradation of polyethylene in the presence of phase transfer catalyst: Part I—Infrared studies. *Polym. Degrad. Stabil.* **21**, 263-275, doi:10.1016/0141-3910(88)90032-8 (1988).

8   Yu, T. *et al.* Poly (ethylene glycol) dimethyl ether mediated oxidative scission of aromatic olefins to carbonyl compounds by molecular oxygen. *Rsc Adv.* **11**, 13848-13852, doi:10.1039/D1RA02007B (2021).

9   Park, Y., Noda, I. & Jung, Y. M. Diverse Applications of Two-Dimensional Correlation Spectroscopy (2D-COS). *Appl. Spectrosc.* **79**, 36-68, doi:10.1177/00037028241256397 (2025).

10   Comnea-Stancu, I. R., Wieland, K., Ramer, G., Schwaighofer, A. & Lendl, B. On the identification of rayon/viscose as a major fraction of microplastics in the marine environment: discrimination between natural and manmade cellulosic fibers using Fourier transform infrared spectroscopy. *Appl. Spectrosc.* **71**, 939-950, doi:10.1177/00037028166607 (2017).

11   Xu, Y., Ou, Q., van der Hoek, J. P., Liu, G. & Lompe, K. M. Photo-oxidation of micro-and nanoplastics: physical, chemical, and biological effects in environments. *Environ. Sci. Technol.* **58**, 991-1009 (2024).

12   Kubelka, J., Pancoska, P. & Keiderling, T. A. Novel use of a static modification of two-dimensional correlation analysis. Part II: Hetero-spectral correlations of protein Raman, FT-IR, and circular dichroism spectra. *Appl. Spectrosc.* **53**, 666-671, doi:10.1366/0003702991947315 (1999).

13   Mawhinney, D. B. & Yates Jr, J. T. FTIR study of the oxidation of amorphous carbon by ozone at 300 K—Direct COOH formation. *Carbon* **39**, 1167-1173, doi:10.1016/S0008-6223(00)00238-4 (2001).

14   Meaurio, E., Zuza, E., López-Rodríguez, N. & Sarasua, J. Conformational behavior of poly (L-lactide) studied by infrared spectroscopy. *J. Phys. Chem. B* **110**, 5790-5800, doi:10.1021/jp055203u (2006).

15   Yang, P., Korshin, G. V., Dong, J., Ji, Y. & Lu, J. Differentiation of pathways of nitrated byproduct formation from ammonium and nitrite during sulfate radical oxidation. *Environ. Sci. Technol.* **56**,

7935-7944, doi:10.1021/acs.est.2c00702 (2022).

16   Yang, P., Ji, Y., Lu, J. & Huang, Q. Formation of nitrophenolic byproducts during heat-activated peroxydisulfate oxidation in the presence of natural organic matter and nitrite. *Environ. Sci. Technol.* **53**, 4255-4264, doi:10.1021/acs.est.8b06967 (2019).

17   Shurvell, H. Spectra-structure correlations in the mid-and far-infrared. *Handbook of vibrational spectroscopy* **3**, 1783-1816, doi:110.1002/0470027320.s4101 (2006).

18   Lee, N. R., Bikovtseva, A. A., Cortes-Clerget, M., Gallou, F. & Lipshutz, B. H. Carbonyl iron powder: a reagent for nitro group reductions under aqueous micellar catalysis conditions. *Org. Lett.* **19**, 6518-6521, doi:10.1021/acs.orglett.7b03216 (2017).

19   Sukhorukov, A. Y. Interrupted Nef and Meyer reactions: a growing point for diversity-oriented synthesis based on nitro compounds. *Molecules* **28**, 686, doi:10.1021/acs.joc.2c02281 (2023).

20   Shen, T., Yuan, Y. & Jiao, N. Metal-free nitro-carbocyclization of activated alkenes: a direct approach to synthesize oxindoles by cascade C–N and C–C bond formation. *Chem. Commun.* **50**, 554-556, doi:10.1039/c3cc47336h (2014).

21   Ballini, R., Bosica, G., Fiorini, D., Palmieri, A. & Petrini, M. Conjugate additions of nitroalkanes to electron-poor alkenes: Recent results. *Chem. Rev.* **105**, 933-972, doi:10.1021/cr040602r (2005).

22   Morales, A. C., Jayarathne, T., Slade, J. H., Laskin, A. & Shepson, P. B. The production and hydrolysis of organic nitrates from OH radical oxidation of β-ocimene. *Atmos. Chem. Phys.* **21**, 129-145, doi:10.5194/acp-21-129-2021 (2021).

23   Kim, D.-h., Lee, J., Ryu, J., Kim, K. & Choi, W. Arsenite oxidation initiated by the UV photolysis of nitrite and nitrate. *Environ. Sci. Technol.* **48**, 4030-4037, doi:10.1021/es500001q (2014).

24   Gupta, D., Harish, B., Kissner, R. & Koppenol, W. H. Peroxynitrate is formed rapidly during decomposition of peroxynitrite at neutral pH. *Dalton Trans.*, 5730-5736, doi:10.1039/B905535E (2009).

25   Gen, M., Zhang, R., Huang, D. D., Li, Y. & Chan, C. K. Heterogeneous oxidation of SO_2 in sulfate production during nitrate photolysis at 300 nm: effect of pH, relative humidity, irradiation intensity, and the presence of organic compounds. *Environ. Sci. Technol.* **53**, 8757-8766, doi:10.1021/acs.est.9b01623 (2019).

26   Benedict, K. B., McFall, A. S. & Anastasio, C. Quantum yield of nitrite from the photolysis of aqueous nitrate above 300 nm. *Environ. Sci. Technol.* **51**, 4387-4395, doi:10.1021/acs.est.6b06370 (2017).

27   Fountoukis, C. & Nenes, A. ISORROPIA II: a computationally efficient thermodynamic equilibrium model for K^+–Ca^{2+}–Mg^{2+}–NH_4^+–Na^+–SO_4^{2-}–NO_3^-–Cl^-–H_2O aerosols. *Atmos. Chem. Phys.* **7**, 4639-4659, doi:10.5194/acp-7-4639-2007 (2007).

28   Jahanzaib, M., Sharma, S. & Park, D. Microplastics comparison of indoor and outdoor air and ventilation rate effect in outskirts of the Seoul metropolitan city. *Emerg. Contam.* **11**, 100408, doi:10.1016/j.emcon.2024.100408 (2025).

29   Zhang, Y. *et al.* Atmospheric microplastics: A review on current status and perspectives. *Earth Sci. Rev.* **203**, 103118, doi:10.1016/i.earscirev.2020.103118 (2020).

30   Harper, L., Qian, C., Luchoo, R. & Warrior, N. 3D geometric modelling of discontinuous fibre composites using a force-directed algorithm. *J. Compos. Mater.* **51**, 2389-2406, doi:10.1177/0021998316672722 (2017).

31   Luqman, M. *et al.* Quantification and characterization of microplastics (MPs) pollution in peri-

uburban agricultural lands of Lahore, Pakistan. *Plos one* **18**, e0291760, doi:10.1371/journal.pone.0291760 (2023).

32   Mutshekwa, T. *et al.* Atmospheric deposition of microplastics in urban, rural, forest environments: A case study of Thulamela Local Municipality. *PloS one* **20**, e0313840, doi:10.1371/journal.pone.0313840 (2025).

33   Gaston, E., Woo, M., Steele, C., Sukumaran, S. & Anderson, S. Microplastics differ between indoor and outdoor air masses: insights from multiple microscopy methodologies. *Appl. Spectrosc.* **74**, 1079-1098, doi:10.1177/0003702820920652 (2020).

34   Aas, W. *et al.* Monitoring of long-range transported air pollutants in Norway. Annual Report 2020. Report No. 8242530408, (2021).

35   Kung, H.-C. *et al.* The current status of atmospheric micro/nanoplastics research: characterization, analytical methods, fate, and human health risk. *Aerosol Air Qual. Res.* **23**, 220362, doi:10.4209/aaqr.220362 (2023).

36   Liao, Z. *et al.* Airborne microplastics in indoor and outdoor environments of a coastal city in Eastern China. *J. Hazard Mater.* **417**, 126007, doi:10.1016/j.jhazmat.2021.126007 (2021).

37   Perera, K., Ziajahromi, S., Bengtson Nash, S., Manage, P. M. & Leusch, F. D. Airborne microplastics in indoor and outdoor environments of a developing country in South Asia: abundance, distribution, morphology, and possible sources. *Environ. Sci. Technol.* **56**, 16676-16685, doi:10.1021/acs.est.2c05885 (2022).

38   Du, R. *et al.* Unveiling the suspended atmospheric microplastic pollution in a coastal urban landscape. *J. Clean. Prod.* **442**, 141145, doi:10.1016/j.jclepro.2024.141145 (2024).

39   O'Brien, S. *et al.* There's something in the air: a review of sources, prevalence and behaviour of microplastics in the atmosphere. *Sci. Total. Envrion.* **874**, 162193, doi:110.1016/j.scitotenv.2023.162193 (2023).

40   Zhu, X. *et al.* Airborne microplastic concentrations in five megacities of northern and southeast China. *Environ. Sci. Technol.* **55**, 12871-12881, doi:10.1021/acs.est.1c03618 (2021).

41   Dris, R. *et al.* Microplastic contamination in an urban area: a case study in Greater Paris. *Environ. Chem.* **12**, 592-599, doi:10.1071/EN14167 (2015).

42   Kaushik, A. *et al.* Identification and physico-chemical characterization of microplastics in marine aerosols over the northeast Arabian Sea. *Sci. Total. Envrion.* **912**, 168705, doi:10.1016/j.scitotenv.2023.168705 (2024).

43   Xi, Z. & Zhao, H. Study on Transient Spectrum Based on Charge Transfer of Semiconductor Quantum Dots. *arXiv preprint*, doi:10.48550/arXiv.2011.14972 (2020).

44   Madsen, D., Larsen, J., Jensen, S. K., Keiding, S. R. & Thøgersen, J. The primary photodynamics of aqueous nitrate: formation of peroxynitrite. *J. Am. Chem. Soc.* **125**, 15571-15576, doi:10.1021/ja030135f (2003).

45   Wang, Y., Jorga, S. & Abbatt, J. Nitration of Phenols by Reaction with Aqueous Nitrite: A Pathway for the Formation of Atmospheric Brown Carbon. *ACS Earth Space Chem.* **7**, 632-641, doi:10.1021/acsearthspacechem.2c00396 (2023).

46   Lin, P. *et al.* Molecular characterization of brown carbon (BrC) chromophores in secondary organic aerosol generated from photo-oxidation of toluene. *Phys. Chem. Chem. Phys.* **17**, 23312-23325, doi:10.1039/C5CP02563J (2015).

47   Cui, Y. *et al.* Influence of ammonia and relative humidity on the formation and composition of secondary brown carbon from oxidation of 1-methylnaphthalene and longifolene. *ACS Earth*

Space Chem. **5**, 858-869, doi:10.1021/acsearthspacechem.0c00353 (2021).

48   Bali, K. *et al.* Measurements of brown carbon and its optical properties from boreal forest fires in Alaska summer. *Atmos. Environ.* **324**, 120436, doi:10.1016/j.atmosenv.2024.120436 (2024).

49   Yang, Z. M., Tsona, N. T., George, C. & Du, L. Nitrogen-Containing Compounds Enhance Light Absorption of Aromatic-Derived Brown Carbon. *Environ. Sci. Technol.* **56**, 4005-4016, doi:10.1021/acs.est.1c08794 (2022).

50   Marrero-Ortiz, W. *et al.* Formation and optical properties of brown carbon from small α-dicarbonyls and amines. *Environ. Sci. Technol.* **53**, 117-126, doi:10.1021/acs.est.8b03995 (2018).

51   Chen, K. *et al.* Relative Humidity Modulates the Physicochemical Processing of Secondary Brown Carbon Formation from Nighttime Oxidation of Furan and Pyrrole. *ACS ES&T Air* **1**, 426-437, doi:10.1021/acsestair.4c00025 (2024).

52   Wong, J. P. *et al.* Atmospheric evolution of molecular-weight-separated brown carbon from biomass burning. *Atmos. Chem. Phys.* **19**, 7319-7334, doi:10.5194/acp-19-7319-2019 (2019).

53   Lambe, A. T. *et al.* Relationship between oxidation level and optical properties of secondary organic aerosol. *Environ. Sci. Technol.* **47**, 6349-6357, doi:10.1021/es401043j (2013).

54   Ni, H. *et al.* Brown carbon in primary and aged coal combustion emission. *Environ. Sci. Technol.* **55**, 5701-5710, doi:10.1021/acs.est.0c08084 (2021).

55   Mayorga, R. J., Zhao, Z. & Zhang, H. Formation of secondary organic aerosol from nitrate radical oxidation of phenolic VOCs: Implications for nitration mechanisms and brown carbon formation. *Atmos. Environ.* **244**, 117910, doi:10.1016/j.atmosenv.2020.117910 (2021).

56   El Mais, A. E. R. *et al.* Insights into secondary organic aerosol formation from the day-and nighttime oxidation of polycyclic aromatic hydrocarbons and furans in an oxidation flow reactor. *Atmos. Chem. Phys.* **23**, 15077-15096, doi:10.5194/acp-23-15077-2023 (2023).

57   Jiang, H. *et al.* Brown carbon formation from nighttime chemistry of unsaturated heterocyclic volatile organic compounds. *Environ. Sci. Tech. Let.* **6**, 184-190, doi:10.1021/acs.estlett.9b00017 (2019).

58   Xie, M. *et al.* Light absorption of secondary organic aerosol: composition and contribution of nitroaromatic compounds. *Environ. Sci. Technol.* **51**, 11607-11616, doi:10.1021/acs.est.7b03263 (2017).

59   Cui, Y., Chen, K., Zhang, H., Lin, Y.-H. & Bahreini, R. Chemical Composition and Optical Properties of Secondary Organic Aerosol from Photooxidation of Volatile Organic Compound Mixtures. *ACS ES&T Air* **1**, 247-258, doi:10.1021/acsestair.3c00041 (2024).

60   Wang, Y. *et al.* Increased UV–Visible Particle Absorption via Evaporation and Drying of Aqueous Droplets Containing Catechol/HONO Solutions. *Environ. Sci. Tech. Let.* **12**, 619-625, doi:10.1021/acs.estlett.5c00364 (2025).

61   Kim, H., Kim, J. Y., Jin, H. C., Lee, J. Y. & Lee, S. P. Seasonal variations in the light-absorbing properties of water-soluble and insoluble organic aerosols in Seoul, Korea. *Atmos. Environ.* **129**, 234-242, doi:10.1016/j.atmosenv.2016.01.042 (2016).

62   Seong, C. *et al.* Influence of relative humidity and composition on $PM_{2.5}$ phases in Northeast Asia. *ACS Earth Space Chem.* **8**, 788-797, doi:10.1021/acsearthspacechem.4c00019 (2024).

63   Din, K. S., Khokhar, M. F., Butt, S. I., Qadir, A. & Younas, F. Exploration of microplastic concentration in indoor and outdoor air samples: Morphological, polymeric, and elemental analysis. *Sci. Total. Envrion.* **908**, 168398, doi:10.1016/i.scitotenv.2023.168398 (2024).

64   Tang, J. *et al.* Molecular signatures and formation mechanisms of particulate matter (PM) water-soluble chromophores from Karachi (Pakistan) over South Asia. *EGUsphere* **2023**, 1-37, doi:10.5194/egusphere-2023-403 (2023).

65   Shahid, M. Z. *et al.* Seasonal variations of aerosols in Pakistan: Contributions of domestic anthropogenic emissions and transboundary transport. *Aerosol Air Qual. Res.* **15**, 1580-1600, doi:10.4209/aaqr.2014.12.0332 (2015).

66   Arun, B. *et al.* Carbonaceous aerosols over lachung in the eastern himalayas: primary sources and secondary formation of organic aerosols in a remote high-altitude environment. *ACS Earth Space Chem.* **5**, 2493-2506, doi:10.1021/acsearthspacechem.1c00190 (2021).

67   Ahmad, M. *et al.* Characteristics, sources, and exposure risk of the carbonaceous species of $PM_{2.5}$ in Lahore, Pakistan. doi:10.21203/rs.3.rs-2335442/v1 (2022).

68   Yan, F. *The deposition and light absorption property of carbonaceous matter in the Himalayas and Tibetan Plateau*, Lappeenranta-Lahti University of Technology LUT, (2020).

69   Amato-Lourenço, L. F., dos Santos Galvão, L., Wiebeck, H., Carvalho-Oliveira, R. & Mauad, T. Atmospheric microplastic fallout in outdoor and indoor environments in São Paulo megacity. *Sci. Total. Envrion.* **821**, 153450, doi:10.1016/j.scitotenv.2022.153450 (2022).

70   Vieira-Filho, M., Pedrotti, J. J. & Fornaro, A. Water-soluble ions species of size-resolved aerosols: Implications for the atmospheric acidity in São Paulo megacity, Brazil. *Atmos. Res.* **181**, 281-287, doi:10.1016/j.atmosres.2016.07.006 (2016).

71   Trebs, I. *et al.* The NH_4^+-NO_3^--Cl^--SO_4^{2-}-H_2O aerosol system and its gas phase precursors at a pasture site in the Amazon Basin: How relevant are mineral cations and soluble organic acids? *J. Geophys, Res. Atmos.* **110**, D07303, doi:10.1029/2004JD005478 (2005).

72   Fernandes, K. S. *et al.* WSOC and Its Relationship with BC, Levoglucosan and Transition Metals in the $PM_{2.5}$ of an Urban Area in the Amazon. *J. Braz. Chem. Soc.* **33**, 570-581, doi:10.21577/0103-5053.20220011 (2022).

73   Zhang, X., Lin, Y.-H., Surratt, J. D. & Weber, R. J. Sources, composition and absorption Ångstrom exponent of light-absorbing organic components in aerosol extracts from the Los Angeles Basin. *Environ. Sci. Technol.* **47**, 3685-3693, doi:10.1021/es305047b (2013).

74   Kim, E. & Hopke, P. K. Source characterization of ambient fine particles in the Los Angeles basin. *J. Environ. Eng. Sci.* **6**, 343-353, doi:10.1139/s06-054 (2007).

75   Richards, L., Anderson, J., Blumenthal, D., Duckhorn, S. & McDonald, J. Characterization of reactants, reaction mechanisms, and reaction products leading to extreme acid rain and acid aerosol conditions in Southern California. (1983).

76   Liu, J. *et al.* Size-resolved measurements of brown carbon in water and methanol extracts and estimates of their contribution to ambient fine-particle light absorption. *Atmos. Chem. Phys.* **13**, 12389-12404, doi:10.5194/acp-13-12389-2013 (2013).

77   Perera, K., Ziajahromi, S., Nash, S. B. & Leusch, F. D. Microplastics in Australian indoor air: Abundance, characteristics, and implications for human exposure. *Sci. Total. Envrion.* **889**, 164292, doi:10.1016/j.scitotenv.2023.164292 (2023).

78   Chin, M. *et al.* Light absorption by pollution, dust, and biomass burning aerosols: a global model study and evaluation with AERONET measurements. *Ann. Geophys.* **27**, 3439-3464, doi:10.5194/ange0-27-3439-2009 (2009).

79   Karydis, V., Tsimpidi, A., Pozzer, A., Astitha, M. & Lelieveld, J. Effects of mineral dust on global

atmospheric nitrate concentrations. *Atmos. Chem. Phys.* **16**, 1491-1509, doi:10.5194/acp-16-1491-2016 (2016).

80 Zhang, Y., Yan, C., Li, Z., Gu, H. & Xie, Y. Development of a multiple solution mixing mechanism based aerosol component retrieval method for polarimetric satellite measurements. *Atmos. Environ.* **349**, 121120, doi:10.1016/j.atmosenv.2025.121120 (2025).

81 Chan, Y. L. *et al.* Pulmonary inflammation induced by low dose particulate matter exposure in mice. *Am. J. Physiol. Lung Cell. Mol. Physiol.* **317**, L424-L430, doi:10.1152/ajplung.00232.2019 (2019).

82 Wu, C. *et al.* Atmospheric concentrations and sources of black carbon over tropical Australian waters. *Sci. Total. Envrion.* **856**, 159143, doi:10.1016/j.scitotenv.2022.159143 (2023).

83 Radhi, M. *et al.* Optical, physical and chemical characteristics of Australian continental aerosols: results from a field experiment. *Atmos. Chem. Phys.* **10**, 5925-5942, doi:10.5194/acp-10-5925-2010 (2010).

84 Chen, E.-Y., Lin, K.-T., Jung, C.-C., Chang, C.-L. & Chen, C.-Y. Characteristics and influencing factors of airborne microplastics in nail salons. *Sci. Total. Envrion.* **806**, 151472, doi:10.1016/j.scitotenv.2021.151472 (2022).

85 Tsai, Y. I. & Kuo, S.-C. $PM_{2.5}$ aerosol water content and chemical composition in a metropolitan and a coastal area in southern Taiwan. *Atmos. Environ.* **39**, 4827-4839, doi:10.1016/i.atmosenv.2005.04.024 (2005).

86 Tsai, Y. I. & Chen, C.-L. Characterization of Asian dust storm and non-Asian dust storm $PM_{2.5}$ aerosol in southern Taiwan. *Atmos. Environ.* **40**, 4734-4750, doi:10.1016/j.atmosenv.2006.04.038 (2006).

87 Ting, Y.-C., Ko, Y.-R., Huang, C.-H., Cheng, Y.-H. & Huang, C.-H. Optical properties and potential sources of water-soluble and methanol-soluble organic aerosols in Taipei, Taiwan. *Atmos. Environ.* **290**, 119364, doi:10.1016/j.atmosenv.2022.119364 (2022).

88 Tsai, H.-H., Yuan, C.-S., Hung, C.-H. & Lin, C. Physicochemical properties of $PM_{2.5}$ and $PM_{2.5-10}$ at inland and offshore sites over southeastern coastal region of Taiwan Strait. *Aerosol Air Qual. Res.* **11**, 664-678, doi:10.4209/aaqr.2010.12.0113 (2011).

89 Wang, Q. *et al.* The characteristics and impact factors of sulfate and nitrate in urban $PM_{2.5}$ over typical cities of Hangzhou Bay area, China. *Atmosphere* **14**, 1799, doi:10.3390/atmos14121799 (2023).

90 Yu, G. *et al.* Short-term effects of meteorological factors and air pollution on childhood hand-foot-mouth disease in Guilin, China. *Sci. Total. Envrion.* **646**, 460-470, doi:10.1016/j.scitotenv.2018.07.329 (2019).

91 Ram, K., Sarin, M. & Tripathi, S. Temporal trends in atmospheric $PM_{2.5}$, PM_{10}, elemental carbon, organic carbon, water-soluble organic carbon, and optical properties: impact of biomass burning emissions in the Indo-Gangetic Plain. *Environ. Sci. Technol.* **46**, 686-695, doi:10.1021/es202857w (2012).

92 Zhang, Y., Jia, Y., Li, M. & Hou, L. a. Characterization of carbonaceous species in $PM_{2.5}$ in Xi'an during spring. *Environ. Forensics* **19**, 150-154, doi:10.1080/15275922.2018.1448910 (2018).

93 Tao, J., Zhang, L., Cao, J. & Zhang, R. A review of current knowledge concerning $PM_{2.5}$ chemical composition, aerosol optical properties and their relationships across China. *Atmos. Chem. Phys.* **17**, 9485-9518, doi:10.5194/acp-17-9485-2017 (2017).

94 Li, J.-M. *et al.* Changes in source contributions to the oxidative potential of $PM_{2.5}$ in urban

Xiamen, China. *J. Environ. Sci. China* **149**, 342-357, doi:10.1016/jjes.2024.02.003 (2025).

95   Li, T.-C., Chen, W.-H., Yuan, C.-S., Wu, S.-P. & Wang, X.-H. Physicochemical characteristics and source apportionment of atmospheric aerosol particles in Kinmen-Xiamen Airshed. *Aerosol Air Qual. Res.* **13**, 308-323, doi:10.4209/aaqr.2011.11.0203 (2013).

96   Bjørnsen, A. *Abundance and Characteristics of Microplastics in Atmospheric Deposition from the Arctic and Mainland, Norway*, NTNU, (2023).

97   Schaap, M., Van Loon, M., Ten Brink, H., Dentener, F. & Builtjes, P. Secondary inorganic aerosol simulations for Europe with special attention to nitrate. *Atmos. Chem. Phys.* **4**, 857-874, doi:10.5194/acp-4-857-2004 (2004).

98   Zhang, A. *et al.* Modeling the global radiative effect of brown carbon: a potentially larger heating source in the tropical free troposphere than black carbon. *Atmos. Chem. Phys.* **20**, 1901-1920, doi:10.5194/acp-20-1901-2020 (2020).

99   Chi, X. *Development of improved sampling and analysis methods for measuring organic, elemental, and water-soluble organic carbon in atmospheric aerosols and application to aerosol studies in Europe and tropical/equatorial and oceanic regions*, Ghent University, (2009).

100   Chen, H. *et al.* Optical properties and molecular composition of wintertime atmospheric water-soluble organic carbon in different coastal cities of eastern China. *Sci. Total. Envrion.* **892**, 164702, doi:10.1016/j.scitotenv.2023.164702 (2023).

101   Li, D., Cui, S., Wu, Y., Wang, J. & Ge, X. Direct Measurement of Aerosol Liquid Water Content: A Case Study in Summer in Nanjing, China. *Toxics* **12**, 164, doi:10.3390/toxics12030164 (2024).

102   Wang, G. *et al.* in *The 7 th Asian Aerosol Conference.* 354.

103   Huang, Y. *et al.* Machine Learning Assisted Chemical Characterization and Optical Properties of Atmospheric Brown Carbon in Nanjing, China. *EGUsphere* **2024**, 1-66, doi:10.5194/egusphere-2024-2757 (2024).

104   Wang, B., Li, Y., Tang, Z. & Cai, N. The carbon components in indoor and outdoor $PM_{2.5}$ in winter of Tianjin. *Sci. Rep.* **11**, 17881, doi:10.1038/s41598-021-98824-W (2021).

105   Sun, T. *et al.* Size-segregated atmospheric humic-like substances (HULIS) in Shanghai: Abundance, seasonal variation, and source identification. *Atmosphere* **12**, 526, doi:10.3390/atmos12050526 (2021).

106   Liu, Y. *et al.* Chemical characteristics and sources of water-soluble organic nitrogen species in $PM_{2.5}$ in Nanjing, China. *Atmosphere* **12**, 574, doi:10.3390/atmos12050574 (2021).

107   Zhou, G. *et al.* Measuring and modeling aerosol: relationship with haze events in Shanghai, China. *Aerosol Air Qual. Res.* **14**, 783-792, doi:10.4209/aaqr.2013.01.0019 (2014).

108   Wu, J., Cheng, W., Lu, H., Shi, Y. & He, Y. The effect of particulate matter on visibility in Hangzhou, China. *J. Environ. Sci. Manag.* **21**, 100-109, doi:10.47125/ijesam/2018 1/10 (2018).

109   Zhang, Q., Zhu, B., Kang, H. & Wang, H. in *2011 International Conference on Remote Sensing, Environment and Transportation Engineering.* 3323-3326 (IEEE).

110   Yang, X., Cheng, S., Li, J., Lang, J. & Wang, G. Characterization of chemical composition in $PM_{2.5}$ in Beijing before, during, and after a large-scale international event. *Aerosol Air Qual. Res.* **17**, 896-907, doi:10.4209/aaqr.2016.07.0321 (2017).

111   Sun, J. *et al.* Secondary inorganic ions characteristics in $PM_{2.5}$ along offshore and coastal areas of the megacity Shanghai. *J. Geophys, Res. Atmos.* **126**, e2021JD035139, doi:10.1029/2021JD035139 (2021).

112   Feng, J. *et al.* Characteristics of organic matter in $PM_{2.5}$ in Shanghai. *Chemosphere* **64**, 1393-

1400, doi:10.1016/j.chemosphere.2005.12.026 (2006).

113   Jaffrezo, J.-L., Aymoz, G., Delaval, C. & Cozic, J. Seasonal variations of the water soluble organic carbon mass fraction of aerosol in two valleys of the French Alps. *Atmos. Chem. Phys.* **5**, 2809-2821, doi:10.5194/acp-5-2809-2005 (2005).

114   Lima, A. R. *et al.* Global patterns for the spatial distribution of floating microfibers: Arctic Ocean as a potential accumulation zone. *J. Hazard Mater.* **403**, 123796, doi:10.1016/j.jhazmat.2020.123796 (2021).

115   Garcia, A. V. *Chemical and optical properties of particulate pollution in the Lille area, Northern France based on ATOLL observations*, Ecole nationale supérieure Mines-Télécom Lille Douai, (2023).

116   Rumman, R. *et al.* Water-Soluble Inorganic Anions in Fine Particulate Matter ($PM_{2.5}$) in Dhaka, Bangladesh: Source Apportionment. *J. Chem.* **2024**, 1296699, doi:10.1155/2024/1296699 (2024).

117   Arun, B. *et al.* Enhanced light absorption by ambient brown carbon aerosols in the eastern Himalayas. *Environ. Sci.: Atmos.* **4**, 782-801, doi:10.1039/D4EA00021H (2024).

118   Saxena, P., Kumar, A., Sharma, K., Khan, A. H. & Kumari, A. Trace Elements and Water-Soluble Ionic Species Associated with Ambient Particulate Matter over Lucknow City, India. *Int. J. Plant Env.* **10**, 120-125, doi:10.18811/ijpen.v10i01.16 (2024).

119   Damay, J., Jirasek, F., Kloft, M., Bortz, M. & Hasse, H. Predicting activity coefficients at infinite dilution for varying temperatures by matrix completion. *Ind. Eng. Chem. Res.* **60**, 14564-14578, doi:10.1021/acs.iecr.1c02039 (2021).

120   Kandilli, C. & Ulgen, K. Solar illumination and estimating daylight availability of global solar irradiance. *Energy Sources, Part A* **30**, 1127-1140, doi:10.1080/15567030601100688 (2008).